FABRICATION OF NOVEL NANOMATERIALS FOR POLYMER ELECTROLYTE MEMBRANE FUEL CELLS AND SELF-CLEANING APPLICATIONS

by
Lei Zhang

A dissertation submitted to the faculty of the University of North Carolina at Chapel Hill in partial fulfillment of the requirements for the degree of Doctor of Philosophy in the Curriculum of Applied and Materials Sciences.

Chapel Hill
2006

Approved by

Advisor: Professor Edward T. Samulski

Reader: Professor Eugene A. Irene

Reader: Professor Joseph M. DeSimone

Reader: Professor Otto Zhou

Reader: Professor Yue Wu

Reader: Professor Richard Superfine

ABSTRACT

LEI ZHANG: FABRICATION OF NOVEL NANOMATERIALS FOR POLYMER ELECTROLYTE MEMBRANE FUEL CELLS AND SELF-CLEANING APPLICATIONS (UNDER THE DIRECTION OF EDWARD T. SAMULSKI)

Materials scientists have embraced nanoscale materials as allowing new degrees of freedom in materials design, as well as producing completely new and enhanced properties compared with conventional materials. However, most nanofabrication methods are tedious and expensive, or require extreme conditions. This thesis presents efficient methods for generating nanostructured materials under relatively mild chemistry and experimental conditions.

The basis of most of this work is porous anodic aluminum oxide (p-AAO) membranes, which have hexagonally close-packed pores and were fabricated following a two-step aluminum anodization procedure. Partially removing the barrier layer of a p-AAO membrane enabled the preparation of silver nanorod arrays using a very simple electrodepostition procedure. One dimensional (1-D) alumina nanostructures were also electrochemically synthesized on the surface of a p-AAO membrane by carefully controlling the anodization parameters.

Polyacrylonitrile nanofibers containing platinum salt were fabricated by polymerization of acrylonitrile in p-AAO templates. Subsequent pyrolysis resulted in carbon nanofibers wherein the platinum salt is reduced *in-situ* to elemental Pt. The Pt nanoparticles are dispersed throughout the carbon nanofibers, have a narrow size range, and are single

crystals. Rotating disc electrode voltammetry suggests that the dispersion of Pt nanocrystals in the carbon nanofiber matrix should exhibit excellent electrocatalytic activity. The preparation of catalyst ink and the construction of membrane-electrode-assembly need to be optimized to get better performance in polymer electrolyte membrane fuel cells.

Platinum nanoparticles embedded in carbon fibers were also prepared using electrospinning. The prepared platinum nanoparticles are narrowly distributed in size and well dispersed in the carbon matrix. This method can provide a large yield of products with a simple setup and procedure.

2-D arrays of nanopillars made from perfluoropolyether (PFPE) derivatives were fabricated using p-AAO membrane templates. Pretexturing the aluminum prior to anodization enables one to engineer multiple morphological length scales and thereby synthesize a lotus leaf-like topography. Both nanopillars on a flat surface and on a lotus leaf-like topology exhibit superhydrophobicity, low contact angle hysteresis and self-cleaning.

DEDICATION

I dedicate this work to my family, my fiancée, and those who have worked hard to make this world a better place.

ACKNOWLEDGEMENTS

I must start off by acknowledging my advisor, Dr. Edward T. Samulski. Besides the guidance, advice, support and encouragement, he provided a great research environment and gave me the freedom to explore. As a graduate student, I can not ask more.

Next, I like to thank the past and present group members, Dr. Bin Cheng, Dr. Louis A. Madsen, Dr. Wensheng Shi, Joette M. Russell-Tanner, Dr. Qian Zhao, Jinrong Liu, Richard Waters, Walter A. Schenck, and Nicholas A. Zafiropoulos, for their friendship and intriguing discussions. It is my pleasure to work with them during the past four years at UNC-Chapel Hill. I especially appreciate Dr. Bin Cheng and Dr. Wensheng Shi for sharing invaluable experience in nanoscience, and Dr. Louis A. Madsen for revising and editing my dissertation.

Many colleagues from other groups also deserve the acknowledgment. I would like to thank Zhilian Zhou and Professor DeSimone for providing PFPE derivatives and sharing fuel cell test station, and Dr. Qi Zhang, Dr. Aaron Rothrock, Dr. Srikanth Ranganathan, Dr. Hui Xu, Dr. Mary Robbins, and Wallace W. Ambrose for help during characterization.

Most of all, I would like to thank my family and my fiancée. Thanks for their love and support all the time. I could not have completed this without them.

TABLE OF CONTENTS

Page

LIST OF TABLES

LIST OF FIGURES

LIST OF ABBREVIATIONS AND SYMBOLS

1-D	one dimensional
AAO	anodic aluminum oxide
AFC	alkaline fuel cell
AFM	atomic force microscopy
AIBN	2,2'-azo-bis-isobutyrylnitrile
BIMat	bio inspired materials
CNFs	carbon nanofibers
DMF	N, N-dimethylformamide
DMFC	direct methanol fuel cell
EDX	energy dispersive X-ray spectroscopy
EM	electron microscopy
FC	fuel cell
FE-SEM	field emission scanning electron microscopy
g	gram
HRTEM	high resolution transmission electron microscopy
ITO	indium doped tin oxide
MEA	membrane electrode assembly
MCFC	molten carbonate fuel cell
mg	milligram
nm	nanometer
p-AAO	porous anodic aluminum oxide
PAFC	phosphoric acid fuel cell

PAN	polyacrylonitrile
PEMFC	polymer electrolyte membrane fuel cell
PFPE	perfluoropolyether
$Pt(acac)_2$	platinum (II) acetylacetonate
Pt-C	platinum-carbon nanocomposite
Pt-CFs	platinum nanoparticles-embedded carbon fibers
Pt-CNFs	platinum nanoparticles-embedded carbon nanofibers (using homemade p-AAO membrane template and $Pt(acac)_2$ as platinum precursor)
Pt-CNFs'	platinum nanoparticles-embedded carbon nanofibers (using Whatman p-AAO membrane template and $Pt(acac)_2$ as platinum precursor)
Pt-CNFs''	platinum nanoparticles-embedded carbon nanofibers (using Whatman p-AAO membrane template and H_2PtCl_6 as platinum precursor)
RDE	rotating disc electrode
SAED	selected area electron diffraction
SEM	scanning electron microscopy
SOFC	solid oxide fuel cell
s-PFPE	styrene end-functionalized perfluoropolyether
s-PFPE-SS	copolymer of styrene end-functionalized perfluoropolyether and highly fluorinated styrene sulfate ester
SS	highly fluorinated styrene sulfate ester
TEM	transmission electron microscopy
V	volt
XPS	X-ray photoelectron spectroscopy
XRD	X-ray diffraction
μm	micrometer (micron)

Chapter I: Introduction

1.1 Nanostructured Materials

A nanometer is a length unit, which is one billionth of a meter. It is approximately equal to the length of nine hydrogen atoms aligned end-to-end. Structures less than 100 nanometers are usually referred to as nanoscale structures. The watershed position of macroscopic and microscopic endows nanoscale materials with special properties (in optics, electrics, mechanics, etc.) with potential application in chemical, energy, medical, electronics and space industries.[1] Preparation, characterization, assembly and exploitation of nanomaterials has been a burgeoning field in materials science.

Because every bulk material has its own intrinsic physical and chemical properties, suitable methods must be adopted to fabricate the corresponding nanoscale counterparts. In the last few years, various kinds of nanostructures including nanoparticles,[2] nanorods,[3] nanaotubes,[4] nanofibers,[5] nanobelts,[6] and core-shell structures[7] have been prepared. A few general ways of synthesizing nanoscale materials have been developed, such as chemical vapor deposition,[8] wet chemical synthesis,[9] and template-based methods.[10]

Future research will focus on fabricating high purity nanoscale materials with regular shape. New chemical or physical methods to easily achieve nanomaterials should be developed. Methods for mass-producing nanoscale materials would be another hotspot when practical applications are realized.

1.2 A Template-Based Method for the Preparation of Nanomaterials

Among synthesizing methods, template-based methods are the most popular and powerful. Normally, nanostructures grow freely in all directions. Their length and shape are not uniform. Impurities usually grow simultaneously and are not easy to eliminate at the end. A template can restrain the nanoscale material's growth in a given direction and it is easy to control growth during the process. When a template-based method is chosen for fabricating nanoscale materials, first, an appropriate template is required, i.e., the configuration of nanostructures in the template must match the desired structures. After the template is chosen, suitable steps must be developed to grow nanoscale materials in the template. Finally, the template needs to be removed and the pure nanoscale materials are acquired. Based on the properties of the template and nanomaterials to be fabricated, numerous methods have been adopted, such as electroless deposition, electrodeposition, chemical vapor deposition, sol-gel methods, and *in-situ* chemical reactions.

There are also some shortcomings of template-based methods. First of all, the availability of templates limits the usage of this method. Generally, only simple nanostructures, such as nanoparticles, nanorods, and nanotubes can be prepared using templates. For some more elaborate structures, there are no appropriate templates available, posing obstacles to this method. Furthermore, template-based methods are not necessarily straightforward. Extra time and materials must be spent making the template, which usually needs to be removed at the end and is not reusable. Generally, fabrication using templates requires more steps than wet-solution growth or chemical vapor deposition. Third, since nanoscale materials are formed in a random way in templates, template-mediated methods usually form polycrystalline materials.

In theory, any material with nanometer-scale structures could be used as the template.

However, a good template should be easily made and easily eliminated. Scientists have done substantial research in this field and found many desirable templates. The most prevalent templates currently used are porous materials, such as track-etched polymeric membranes, porous anodic aluminum oxide (p-AAO) membranes, and mesoporous silica. One dimensional nanomaterials can be fabricated inside the porous structures. Besides nanoporous materials, carbon nanotubes could act as templates in carbon-nanotube confined reactions.[11] Synthesis using ZnO nanowires[12] and DNA[13] templates have also been reported.

1.3 Porous Anodic Aluminum Oxide Membranes

Aluminum anodization, which was developed in the early 1930's, is a common technology to passivate aluminum surfaces. Aluminum surfaces are naturally covered with a thin layer of alumina in air, which is only several tens of nanometers thick. With the technique of aluminum anodization, a dense anodic film as thick as several microns can be made. The anodic film is hard and electrically insulating, which could improve the resistance to abrasion and corrosion. Therefore, anodization has been widely applied in industry to protect aluminum metal. In addition, the anodic film, which has a stronger adhesion with organic coatings, provides an excellent paint base.

Aluminum anodization is carried out by applying an electrical current to aluminum submersed in an electrolyte. Depending on the electrolyte used, two types of anodic aluminum oxide can form. Anodization of aluminum in a neutral or basic solution (pH>5) results in a flat, nonporous alumina layer (Figure 1-1A). Anodization in an acid leads to an alumina layer with pores, the arrangement of which is approximately hexagonal (Figure 1-1B).[14]

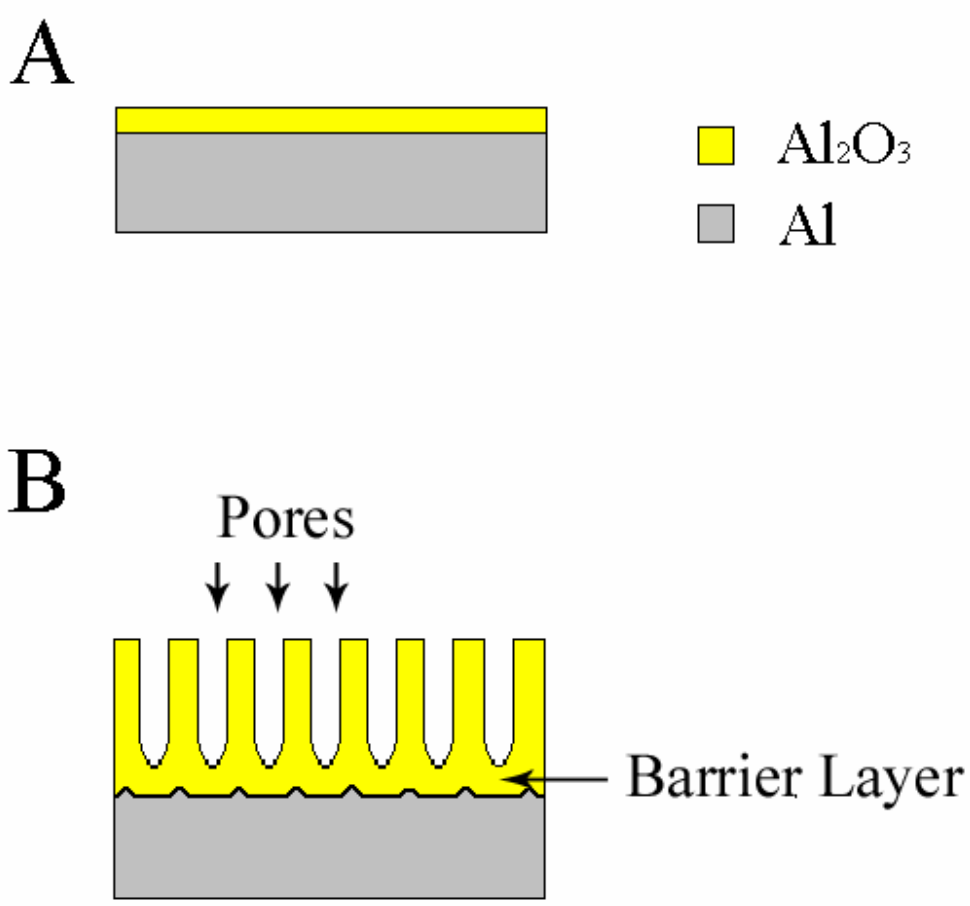

Figure 1-1. Schematic diagrams of a (A) flat and (B) porous aluminum oxide membrane after aluminum anodization.
(A) Aluminum anodization in a neutral or basic solution (pH>5) produces a flat layer of alumina; (B) aluminum anodization in acid solution produces a porous layer of alumina.

It is widely believed that the formation of pores during anodization depends on the oxidation rate of aluminum at the interface of metal and oxide, and on the electric-field-enhanced dissolution rate at the interface of oxide and electrolyte.[14,15] The original aluminum foil (Figure 1-2A) is generally electrochemically polished in perchloric acid alcohol solution to get a smooth surface (Figure 1-2B). A thin layer of alumina may form on the surface of aluminum when the electropolished aluminum is in contact with air. At the beginning of aluminum anodization, since the naturally formed alumina layer is very thin and the conductivity is good, large anodic current pass through the aluminum foil. A thicker layer of alumina is produced on the surface of aluminum foil under the electric field (Figure 1-2C), which in-turn would increase the resistance of system, reduce the anodic current and the formation rate of alumina. During the anodization,[14] Al^{3+} forms at the interface of aluminum and alumina (1), and the water-splitting reaction happens at the interface of alumina and electrolyte (2). The formed O^{2-} migrates through the oxide layer under the electric field and reacts with the produced Al^{3+} at the interface of aluminum and alumina (3). The aluminum oxide at the interface of alumina and electrolyte reacts with acid and dissolves in the electrolyte under the assistance of the electric field (4). Small differences within the alumina layer would cause an inhomogeneous electric field at the surface of the alumina. As indicated in Figure 1-2C, at spots where the alumina layer is thinner, the electric field density is much stronger and the electric-field-enhanced dissolution is much faster than in the surrounding area; therefore, small pores form (Figure 1-2D). The electric potential can penetrate into the pores and the electric field at the pore bottoms will be stronger. Therefore, once small pores have formed, the growth become self-catalyzing. There is always a thin layer of alumina between the pore bottom and the aluminum substrate, which is called the barrier

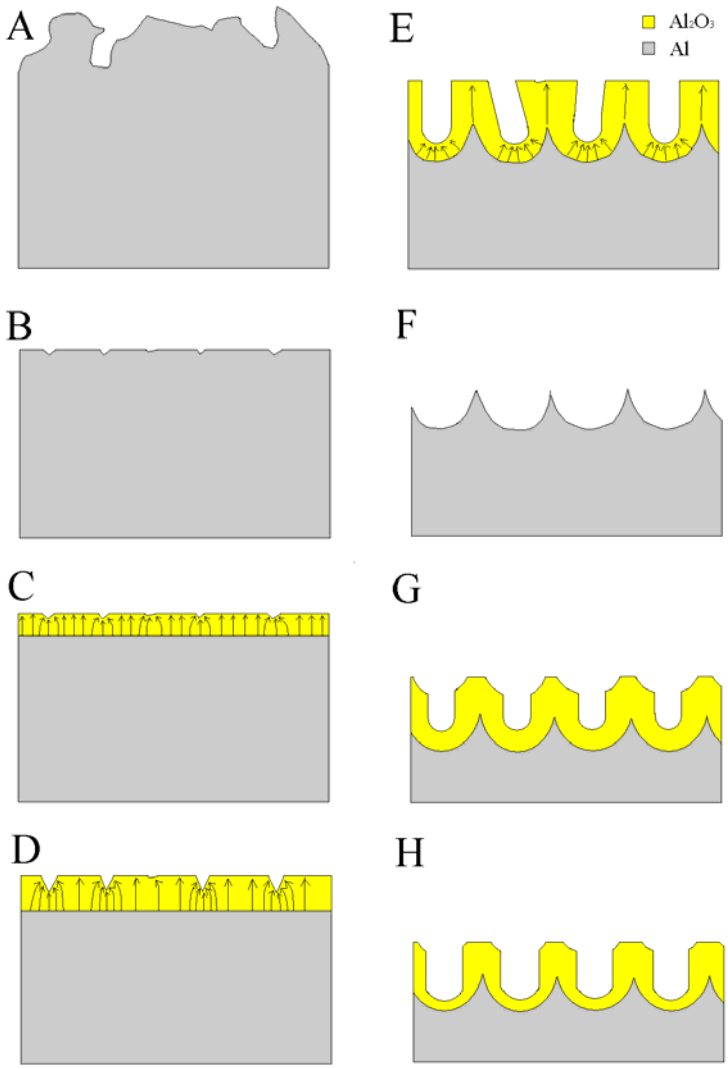

Figure 1-2. Schematic diagram of the development of a porous aluminum oxide membrane during a two-step aluminum anodization.
(A) and (B) an aluminum foil before and after electropolishing; (C), (D) and (E) porous structures form under the electric filed assisted dissolution (arrows indicate electric field) and formation of alumina; (F) close-packed pits form on the surface of aluminum foil after stripping the alumina layer; (G) close-packed pores form during the second anodization; (H) diameter of pores can be adjusted by chemical etching.

layer (Figure 1-1B). If the dissolution rate is faster than the formation rate, the barrier layer becomes thinner. This leads to a larger anodic current and a faster alumina formation rate, and vice versa. Therefore, the formation rate of alumina and the electric-field-assisted dissolution of alumina would equilibrate and the barrier layer thickness would not continue to change. The final barrier layer thickness is determined by the anodization voltage, which is optimal around 1-1.2 nm/V.[16] As the surrounding alumina layer becomes thicker, the dissolution rate would become even slower than that at the bottom of pores. Pores grow continuously during the anodization, with the surrounding alumina left as channel walls (Figure 1-2E). Li et al. found that about 30% of the produced alumina was dissolved in electrolyte, while 70% of the alumina constructed the nanochannel walls.[14] H^+ can migrate to the cathode and be reduced to H_2 to complete the circuit (5).

$$H_2O\ (l) \rightarrow 2H^+(aq) + O^{2-}(oxide) \quad (1)$$

$$Al\ (s) \rightarrow Al^{3+}(oxide) + 3e^- \quad (2)$$

$$3O^{2-}(oxide) + 2Al^{3+}(oxide) \rightarrow Al_2O_3(s) \quad (3)$$

$$Al_2O_3(s) + 6H^+ \rightarrow Al^{3+}(aq) + 3H_2O(l) \quad (4)$$

$$2H^+(aq) + 2e^- \rightarrow H_2\ (g) \quad (5)$$

The overall reaction is

$$2Al(s) + 3H_2O\ (l) \rightarrow Al_2O_3(s) + 3H_2(g) \quad (6)$$

In 1995, Mesuda et al. first reported the fabrication of porous aluminum oxide with a perfect hexagonal packing over a micron scale area.[17] After stripping the anodized alumina layer form during the first anodization, hexagonally packed pits form on the aluminum surface (Figure 1-2F). The origin for the hexagonal ordering, which depends on the anodization voltage and the electrolyte, is still not clear. It may be induced by a diffusion of

the pore bottoms, aided by the lateral mobility of Al^{3+} and O^{2-} in the barrier layer.[14] These pits formed after the first anodization serve as the master for the second step anodization at the same conditions as the first one. Ultimately, a perfect hexagonal pore arrangement is obtained (Figure 1-2G).

The cell diameter, or the interpore distance is determined by the anodization voltage. P-AAO membranes with pore diameters from 50 to over 500 nm can be fabricated by selecting the appropriate anodization voltage and electrolyte,[18] including sulfuric, oxalic, phosphoric, and chromic acid. Li et al. suggested that there was a linear relation between interpore distance d and anodization voltage U with $d = -1.7 + 2.81U$.[19] Other articles suggested that it was around 2.5 nm/V for the interpore spacing and 1.29 nm/V for the pore diameter.[15] After anodization, the pore diameter can be further enlarged by chemical etching in phosphoric acid (Figure 1-2H) to get the desired pore diameter.[17]

P-AAO membranes with a desired thickness can be prepared by controlling the anodization time. The growth rate of pores depends on the anodization voltage and current, the electrolyte, and the temperature. Generally, it is around 2-6 microns per hour.[20]

Besides using a two-step anodization method, hexagonally packed pores can be fabricated on pre-textured aluminum by electropolishing or indenture using a master with an appropriate pattern.[21]

As was shown in Figure 1-1B, porous alumina nanostructures are formed on aluminum substrates via anodization. P-AAO membranes on other substrates can also be prepared. An aluminum film around several microns in thickness is first deposited on the desired substrates (e.g. Si and glass) through thermal evaporation or sputter coating. Following the two-step anodization, porous alumina structures may be produced on SiO_2, Si

wafer [15,22] and ITO glass.[23,24] The hexagonal-packed pattern of p-AAO can even be subsequently transferred to the substrate.[15]

1.4 Porous Anodic Aluminum Oxide Membrane Templates for Preparation of Nanomaterials

P-AAO membranes are the most widely used templates for the synthesis of nanomaterials.[10] Compared with other template methods, p-AAO is cheap, easy to make and eliminate, and widely applicable. The parameters of p-AAO membranes (such as thickness and pore diameter), which determine the desirable parameters of nanomaterials are easily controllable by changing the anodization voltage, time and post treatment. The fabricated nanostructures are well aligned, and very uniform in size and length.

A variety of nanomaterials[16,25-29] including nanofibers, nanorods and nanotubes composed of metals, metal oxides, carbon, polymers, and composites have been fabricated based on p-AAO membrane templates using several methods, such as chemical vapor deposition, electrodeposition, sol-gel synthesis, and polymerization. 1-D nanostructures composed of metals are generally fabricated in the nanochannels of p-AAO templates using electrodeposition; nanostructures of metal oxides are usually made using sol-gel methods on p-AAO membrane; carbon nanotubes are made in p-AAO membranes using chemical vapor deposition; polymer nanofibers are prepared using p-AAO templates by polymerizing the liquid monomers inside the nanochannels.

1.5 Fuel Cells

The principle of the fuel cell was first discovered by William Grove, a British jurist

and amateur physics, in 1839. In the late 1950s and early 1960s, NASA applied fuel cell technologies to the Gemini and Apollo space missions to provide power and drinking water. Today, many automobiles companies, research centers, and universities worldwide are doing research to overcome the technical barriers to widespread commercialization of fuel cells.

Fuel cells (FCs) show promise to be the energy conversion devices for the 21st century due to several advantages. The first characteristic of fuel cells is high efficiency. Fuels are oxidized at the fuel cell anode, and oxygen is reduced to water on the cathode. Since fuel cells convert chemical energy directly to electrical energy without going through the process of heat to mechanical energy, their efficiencies are not limited by the Carnot Cycle, as in internal combustion engines. Generally, the efficiency of internal combustion engine is around 15%, while for fuel cells, the efficiency is around 40%. The second advantage is quiet operation. Since there are no moving parts in fuel cells, they can be operated quietly. The third and most important advantage of fuel cells comes from their pollutant-free emission. If hydrogen is used as the fuel, the only emission is water (hydrogen can be produced from electrolysis of water using the wind, water flow or solar energy). According to the electrolyte used in the fuel cells, they are generally divided into five categories: polymer electrolyte membrane fuel cells (PEMFCs, they are also known as proton exchange membrane fuel cells), alkaline fuel cells (AFCs), phosphoric acid fuel cells (PAFCs), molten carbonate fuel cells (MCFCs), and solid oxide fuel cells (SOFCs). [30]

1.6 Polymer Electrolyte Membrane Fuel Cells

PEMFC technologies were developed by GE and NASA in 1960s. The electrolyte for a PEMFC is a proton-conductive solid organic polymer (Figure 1-3). There are several

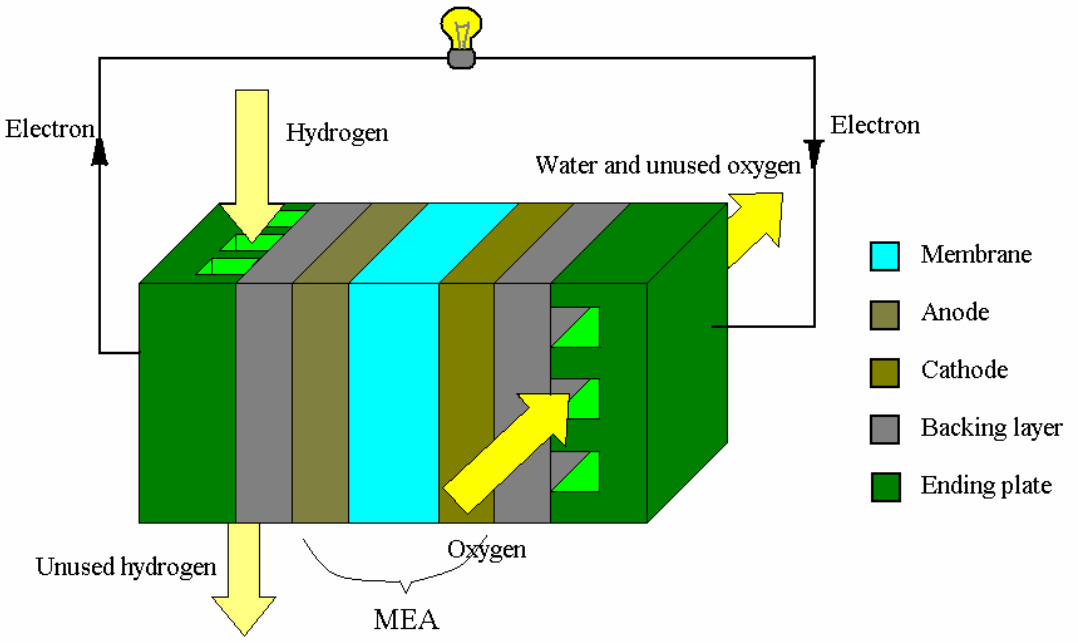

Figure 1-3. Schematic diagram of a polymer electrolyte membrane fuel cell.

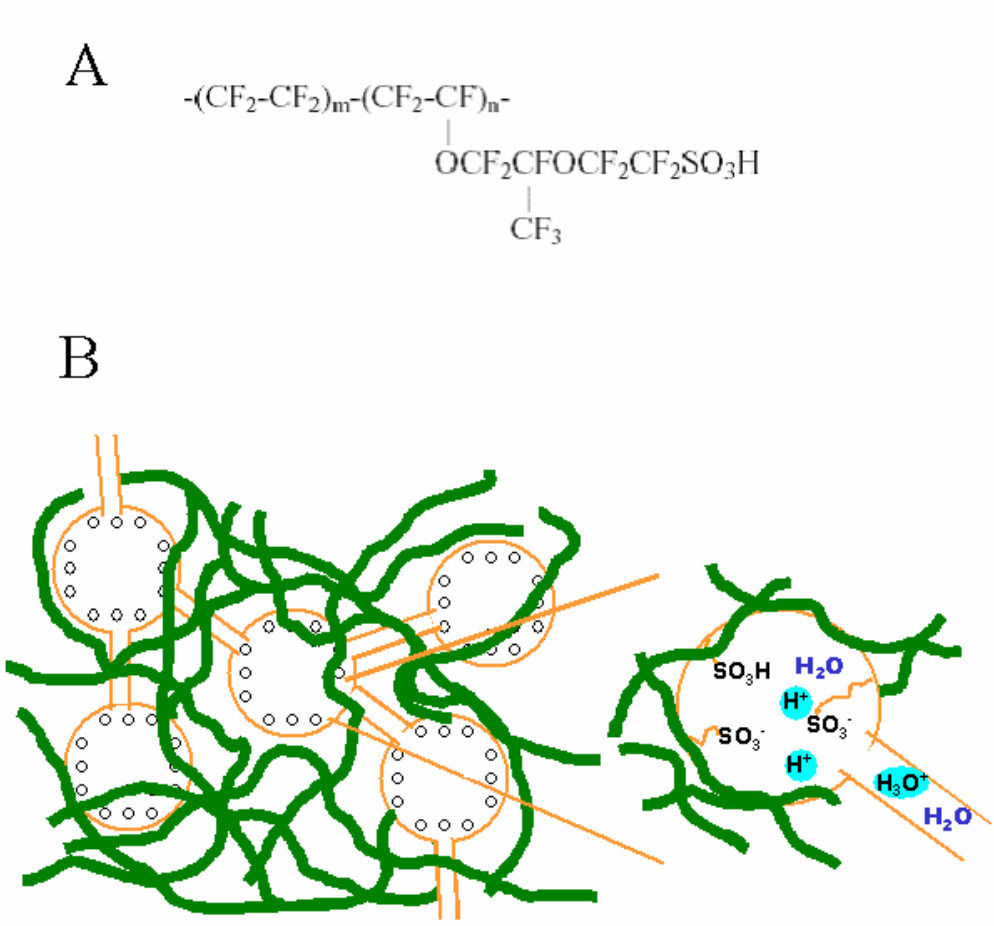

Figure 1-4. (A) Chemical structure of Nafion and (B) schematic diagram of protons diffusion in hydrated Nafion.

advantages of PEMFCs over the other types of fuel cells, such as low temperature operation, quick start-up, and reduction of corrosion & management problems due to the solid electrolyte. The voltage from a single cell is around 0.7 V; the voltage for fuel cell stacks is 0.7 V multiplied by the number of cells stacked. PEMFCs are considered to be an alternative to internal combustion engines for vehicles.

The core part of a PEMFC is called membrane electrode assembly (MEA). Today, the most prevalent membrane is Nafion, a poly-perfluorosulfonic acid (Figure 1-4A). Nafion membranes usually have thickness from 50 to 175 microns. The transition from polystyrene sulfonic acid membranes to perfluorosulfonic acid membranes is one of the quantum jumps in technology in the past forty years.[31,32] Nafion consists of three regions: Teflon-like fluorocarbon backbones ($-CF_2-CF_2-CF_2-$), side chains ($-O-CF_2-CF(CF_3)-O-CF_2-CF_2-$), and ion clusters consisting of sulfonic acid ions ($SO_3^-H^+$). When the membrane is hydrated by adsorbed water, it becomes an excellent conductor for protons (Figure 1-4B). Depending on the water contents, the transport of proton in Nafion is carried out via surface diffusion mechanism (protons bond to water molecules and hop from SO_3^- site to SO_3^- site close to pore walls) and/or a bulk diffusion mechanism (protons diffuse in the center region of the pores through Grotthuss mechanism and *en masse* diffusion).[33] To keep water in the membrane in a liquid phase, the general operating temperature for a PEMFC is between 60 and 100 ˚C. Operation above 100 ˚C needs pressurized conditions which usually shortens the life of fuel cell. Beside the function of proton conductivity, the membrane performs as a gas separator (to keep the hydrogen fuel separated from the oxygen) and an electron insulator.

The electrochemical reaction happens on the catalyst layers, which are commonly composed of platinum and carbon. In the oxidation half-reaction, hydrogen fuel produces

protons and electrons at the anode (7). Protons travel through the membrane to the cathode, while electrons transfer through an external circuit to the cathode. In the reduction half-reaction, oxygen reacts with protons and electrons to form water at the cathode (8). The final products of the overall reaction are H_2O, electric current, and excess heat.

Anode: $$H_2 \rightarrow 2H^+(aq) + 2e^- \quad (7)$$

Cathode: $$\tfrac{1}{2} O_2 + 2H^+ + 2e^- \rightarrow H_2O \quad (8)$$

Overall: $$H_2 + \tfrac{1}{2} O_2 \rightarrow H_2O \quad (9)$$

Since PEMFCs need to operate at very low temperature relative to other types of fuel cells, a catalyst with excellent activity is required. The catalyst that works the best for both the oxidation of hydrogen at anode and the reduction of oxygen at cathode in PEMFC is Pt, a very expensive metal. The oxygen reduction half reaction is much slower than the hydrogen oxidization reaction; hence, the performance of PEMFC is primarily limited by reaction at the cathode.

The backing layer is made of electron conductive materials. The most prevalent backing layer is porous carbon paper and carbon cloth. The backing layer serves the triple role of conducting electrons (exiting the anode and entering the cathode), providing effective diffusion of each reactant gas and managing water during operation. Flooding is a serious problem in PEMFC operation, especially when operated at large current densities. By placing a thin diffusion layer (made of fine carbon particles) between the backing layer and the catalyst layer, water can be better managed in a PEMFC.[34] This improves the electrode performance, particularly at high current density. A PEMFC with catalyst layer, diffusion layer and backing layer is generally called a three-layer electrode FC, while FCs with only catalyst layer and backing layer is called a two-layer electrode FC.[34]

The end-plates are in contact with the backing layers. The main functions of the end-plates are providing flow fields for reactants and products, and collecting current. The plates are commonly made of graphite or metals.

1.7 Developments in Polymer Electrolyte Membrane Fuel Cell Electrodes

Due to the rapid start-up capability, PEMFCs are usually chosen for mobile applications. However, for large-scale automotive application, a significant reduction of platinum loading is required due to high cost and platinum supply limitations.[35] Attaining platinum's specific power density of 0.2 g_{Pt}/kW at 0.6 V is an ideal PEMFC performance target.[36] Reducing the platinum loadings and costs, improving the performance of platinum-based catalysts in fuel cells, and finding a substitute to Pt are challenging projects in this area.

There have been great improvements in this area in the past twenty years. It requires about 4-10 mg/cm^2 platinum when using platinum black as the electrode. By the introduction of a Nafion-ionomer-impregnated gas diffusion electrode, the three-dimensional reaction zone has been extended. Pt loading has been reduced to about 0.4 mg/cm^2 or even less when using carbon-supported platinum.[34]

When operated at low temperature, platinum is very sensitive to fuel impurities. The poisoning of Pt is serious when using reformed fuels (with CO). Pt alloys are developed as catalysts to enhance the tolerance to reformed fuels. The best performing platinum alloy includes Pt-Ru and Pt-Mo for the anode, and Pt-Co, Pt-Ni, Pt-Cr, Pt-V for the cathode.

Some Pt alloys also enhance the activity of the oxygen reduction reaction.[36] Catalysts without platinum are also under investigation.[35] Combinatorial chemistry methods have been used to speed up the search for catalyst formulations.

Aside from the platinum loading, electrode durability is another important issue. Long-term cycling and high potentials/temperatures always lead to a loss of platinum surface area and a reduction of fuel cell performance. Generally, there are three processes for the loss of apparent platinum surface area: (1) an Ostwald ripening process via platinum dissolution and redeposition, (2) coalescence of platinum nanoparticles through migration on the carbon support, and (3) agglomeration of platinum nanoparticles due to corrosion of the carbon support.[37] At a given current density, the fuel cell voltage is mainly determined by the available surface area of platinum in the electrode (especially the cathode). The long-term performance degradation of less than 10 μV/h is required for automotive applications.

1.8 Overview

This dissertation presents development of efficient fabrication techniques for novel nanostructures using p-AAO membrane templates and elecrospinning. 2-D arrays of nanopillars and lotus leaf-like structures made from perfluoropolyether (PFPE) derivatives were fabricated. The nanostructured topologies exhibit superhydrophobicity, low contact angle hysteresis and self-cleaning. The general method of electrodepositing metal nanorods on p-AAO membrane templates was modified, which enabled the fabrication of silver nanorod arrays in a very simple way. One dimensional (1-D) alumina nanostructures were electrochemically synthesized on the surface of a p-AAO membrane by controlling the aluminum anodization conditions. This method provides a large yield of 1-D alumina nanostructures without the involvement of complicated setups and procedures, and extreme conditions.

Platinum nanoparticles embedded in carbon nanofibers were fabricated using

template-based methods. The prepared single crystalline platinum nanoparticles are highly dispersed in the carbon matrix, yielding a system with excellent electrocatalytic activity and a promising stability in PEMFC operations. This may help improve the durability and life of fuel cells. Platinum nanoparticles embedded in carbon fibers were also prepared using elecrospinning. A large yield of products can be prepared with a simple setup and procedure.

1.9 References

(1) Rao, C. N. R.; Cheetham, A. K. *J. Mater. Chem.* **2001**, *11*, 2887-2894.

(2) Sun, S.; Murray, C. B.; Weller, D.; Folks, L.; Moser, A. *Science* **2000**, *287*, 1989-1992.

(3) Morales, A. M.; Lieber, C. M. *Science* **1998**, *279*, 208 - 211.

(4) Qin, L.-C.; Zhao, X.; Hirahara, K.; Miyamoto, Y.; Ando, Y.; Iijima, S. *Nature* **2000**, *408*, 50.

(5) Hartgerink, J. D.; Beniash, E.; Stupp, S. I. *Science* **2001**, *294*, 1684-1688.

(6) Pan, Z. W.; Dai, Z. R.; Wang, Z. L. *Science* **2001**, *291*, 1947-1949.

(7) Skumryev, V.; Stoyanov, S.; Zhang, Y.; Hadjipanayis, G.; Givord, D.; Nogues, J. *Nature* **2003**, *423*, 850-853.

(8) Li, Y.-L.; Kinloch, I. A.; Windle, A. H. *Science* **2004**, *304*, 276-278.

(9) Peng, X.; Manna, L.; Yang, W.; Wickham, J.; Scher, E.; Kadavanich, A.; Alivisatos, A. P. *Nature* **2000**, *404*, 59-61.

(10) Martin, C. R. *Science* **1994**, *266*, 1961-1966.

(11) Han, W.; Fan, S.; Li, Q.; Hu, Y. *Science* **1997**, *277*, 1287-1289.

(12) Goldberger, J.; He, R.; Zhang, Y.; Lee, S.; Yan, H.; Choi, H.-J.; Yang, P. *Nature* **2003**, *422*, 599-602.

(13) Braun, E.; Eichen, Y.; Sivan, U.; Ben-Yoseph, G. *Nature* **1998**, *391*, 775-778.

(14) Li, F.; Zhang, L.; Metzger, R. M. *Chem. Mater.* **1998**, *10*, 2470-2480.

(15) Crouse, D.; Lo, Y.-H.; Miller, A. E.; Crouse, M. *Appl. Phys. Lett.* **2000**, *76*, 49-51.

(16) Nielsch, K.; Muller, F.; Li, A.-P.; Gosele, U. *Adv. Mater.* **2000**, *12*, 582-586.

(17) Masuda, H.; Fukuda, K. *Science* **1995**, *268*, 1466-1468.

(18) Masuda, H.; Yada, K.; Osaka, A. *Jpn. J. Appl. Phys.* **1998**, *37*, L1340-L1342.

(19) Li, A. P.; Muller, F.; Birner, A.; Nielsch, K.; Gosele, U. *J. Appl. Phys.* **1998**, *84*, 6023-6026.

(20) Jessensky, O.; Muller, F.; Gosele, U. *Appl. Phys. Lett.* **1998**, *72*, 1173-1175.

(21) Asoh, H.; Nishio, K.; Nakao, M.; Tamamura, T.; Masuda, H. *J. Electrochem. Soc.* **2001**, *148*, B152-B156.

(22) Cai, A.; Zhang, H.; Hua, H.; Zhang, Z. *Nanotechnology* **2002**, *13*, 627-630.

(23) Chu, S. Z.; Wada, K.; Inoue, S.; Todoroki, S. *Surface and Coatings Technology* **2003**, *169-170*, 190-194.

(24) Chu, S.-Z.; Wada, K.; Inoue, S.; Todoroki, S.-I. *Chem. Mater.* **2002**, *14*, 266-272.

(25) Chu, S.-Z.; Wada, K.; Inoue, S. *Adv. Mater.* **2002**, *14*, 1752-1756.

(26) Che, G.; Lakshmi, B. B.; Martin, C. R.; Fisher, E. R. *Chem. Mater.* **1998**, *10*, 260-267.

(27) Steinhart, M.; Wendorff, J. H.; Greiner, A.; Wehrspohn, R. B.; Nielsch, K.; Schilling, J.; Choi, J.; Gosele, U. *Science* **2002**, *296*.

(28) Kim, K.; Lee, S. H.; Yi, W.; Kim, J.; Choi, J. W.; Park, Y.; Jin, J.-I. *Adv. Mater.* **2003**, *15*, 1618-1622.

(29) Cheng, B.; Samulski, E. T. *J. Mater. Chem.* **2001**, *11*, 2901-2902.

(30) Thomas, S.; Zalbowitz, M. *Fuel Cells- Green Power* **1999**.

(31) Costamagna, P.; Srinivasan, S. *J. Power Sources* **2001**, *102*, 242-252.

(32) Costamagna, P.; Srinivasan, S. *J. Power Sources* **2001**, *102*, 253-269.

(33) Choi, P.; Jalani, N. H.; Datta, R. *J. Electrochem. Soc.* **2005**, *152*, E123-E130.

(34) Antolini, E. *J. Appl. Electrochem.* **2004**, *34*, 563-576.

(35) Gasteiger, H. A.; Kocha, S. S.; Sompalli, B.; Wagner, F. T. *Appl. Catal. B :*

Environmental **2005**, *56*, 9-35.

(36) Ball, S. C. *Platinum Metals Rev.* **2005**, *49*, 27-32.

(37) Ferreira, P. J.; la O', G. J.; Shao-Horn, Y.; Morgan, D.; Makharia, R.; Kocha, S.; Gasteiger, H. A. *J. Electrochem. Soc* **2005**, *152*, A2256-A2271.

Chapter II: Preparation of Porous Anodic Aluminum Oxide Membranes and One Dimensional Alumina Nanostructures

2.1 Introduction

As stated in Chapter 1, fabrication of nanomaterials using porous anodic aluminum oxide (p-AAO) membranes as templates is a general method.[1,2] During my thesis research, several kinds of nanostructures were fabricated using p-AAO templates, e.g., platinum-embedded carbon nanofibers, perfluoropolyether nanopillars, and silver nanorod arrays.

Although there is commercial Whatman p-AAO membrane available, its microstructure is far from perfect. As shown in the scanning electron microscopy (SEM) images (Figure 2-1), pore openings on the surface of a commercial p-AAO membrane are not uniform in size. They are randomly packed with a mean diameter around 0.2 μm. Pore channels of these membranes are also not perfectly parallel, with intersections at random points. There are several kinds of Whatman membranes commercially available, such as 0.2 μm and 0.02 μm specified pore sizes. However, the bulk section of a 0.02 μm membrane is the same as a 0.2 μm membrane. The only difference is an extra thin porous layer with channels around 0.02 μm on the glassy side. This is because the main application of Whatman p-AAO membranes is filtration, and a thin layer will serve that purpose. For template-based fabrication of nanomaterials, 0.2 μm and 0.02 μm membranes would give the same structures, i.e., nanostructures with different diameters could not be fabricated by choosing different Whatman templates. In addition to the fixed channel diameters, the thickness of Whatman membranes is fixed.

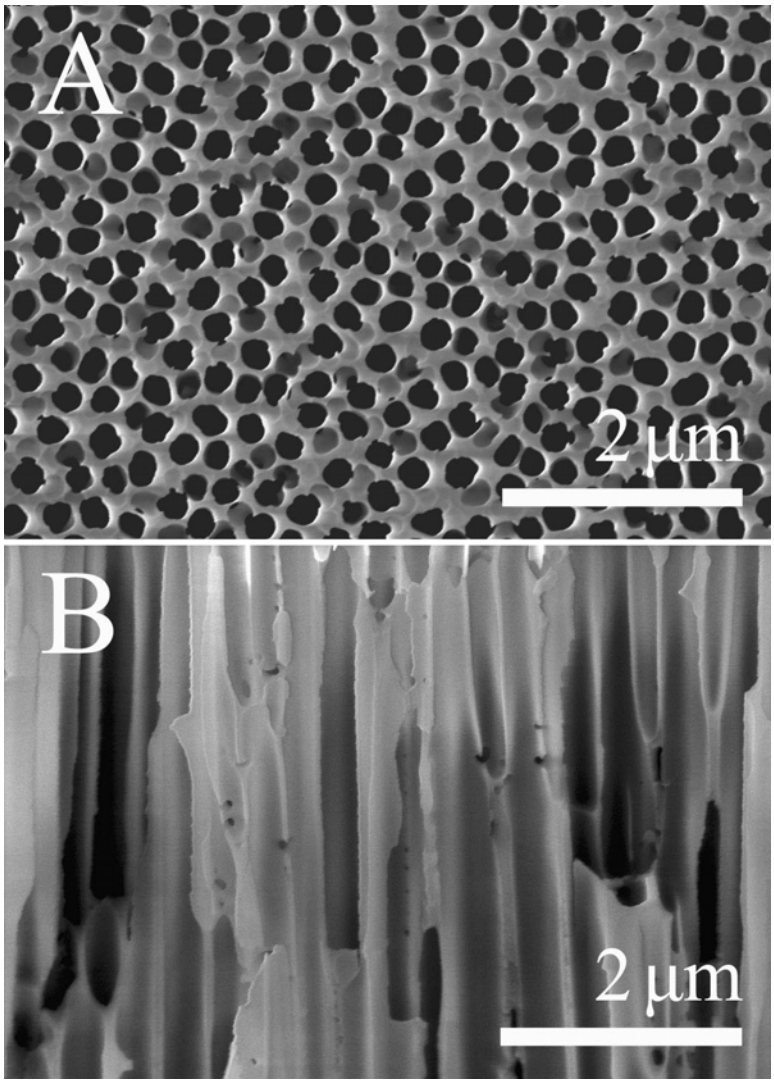

Figure 2-1. FE-SEM micrographs of a 0.2 µm Whatman p-AAO membrane.
(A) Top view shows the randomly packed pore openings on the surface of membrane; (B) cross-sectional view shows the irregular channels.

To get high quality and controllable parameters in a p-AAO template, such as channel diameter or membrane thickness, anodization of aluminum foil was carried out following the well known two-step procedure.[3,4] This chapter describes in detail the preparation of p-AAO membranes with different pore sizes. Post-growth modifications of fabricated p-AAO membranes for different applications are also covered. As an example of applications, electrodeposition of silver nanorod arrays using a homemade p-AAO membrane template is presented. By controlling the anodization voltage, time and temperature, one dimensional (1-D) alumina nanostructures could also be fabricated using the same procedure. The last section covers details of this experiment and a possible formation mechanism.

2.2 Materials and Instrumentation

Materials: Oxalic acid (99.5%, Alfa Aesar), chromic oxide (99.6%, Fisher), copper chloride (99+%, Alfa Aesar), phosphoric acid (86%, Fisher Scientific), perchloric acid (70%, Alfa Aesar), hydrochloric acid (37.3%, Fisher Scientific), sulfuric acid (99.999%, Aldrich), sodium hydroxide (98.7%, Mallinckrodt), ethanol (Fisher Scientific), silver plating solution (1025, Technic Inc.) and Whatman 0.2 μm porous anodic aluminum oxide membrane discs (Fisher Scientific) were used as received, unless stated otherwise. Aluminum foils (99.99%, Alfa Aesar) were cleaned by acetone to remove grease. After cleaning, aluminum foils were kept in acetone for future use.

Instrumentation: Power supplies (Agilent E3612A, Brandenburg Photomultiplier 472R, and Bio-Rad PowerPac Basic) were used for aluminum anodization at different voltage ranges. The morphologies of the samples were characterized using scanning

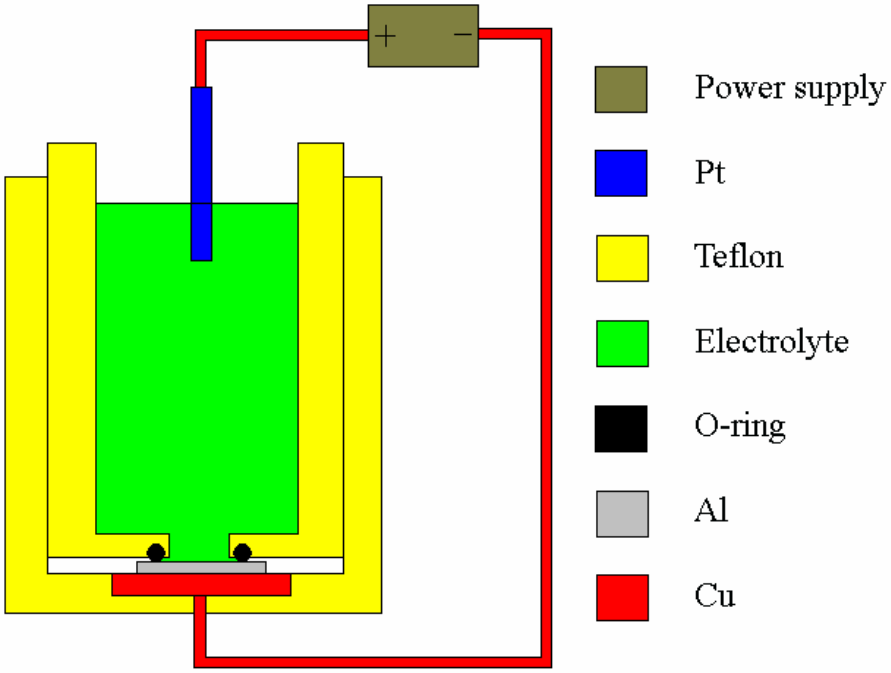

Figure 2-2. Schematic diagram of the Teflon cell for the anodization of aluminum foil. The Pt wire serves as cathode and the Cu plate serves as anode. The O-ring prevents electrolyte from leaking.

electron microscopy (SEM, JEOL JEM6300), field-emission scanning electron microscopy (FE-SEM, Hitachi S4700), and transmission electron microscopy (TEM, JEOL JEM-100CXII). An energy-dispersive X-ray (EDX) spectrometer installed in a JEOL JEM6300 was used for the composition analysis. X-ray diffraction (XRD, Rigaku Multiflex X-ray diffractometer) and selected area electron diffraction (SAED) installed in a JEOL JEM-100CXII were used to determine the crystallinity of the materials.

2.3 Preparation of Porous Anodic Aluminum Oxide Membranes

2.3.1 Experimental

2.3.1.1 Preparation of p-AAO Membranes Anodized at 40V

Anodization of aluminum foil was conducted in a homemade Teflon cell (Figure 2-2) following the two-step procedure.[3-5] In a typical experiment, a high purity aluminum foil (99.99%) was first electrochemically polished in a mixture of perchloric acid (70%) and ethanol with a volume ratio of 3:7 at a constant current of 100 mA for 4 minutes. Electrochemically polished aluminum foil was held in the Teflon cell with one surface in contact with a Cu plate anode; a Pt wire served as the cathode, and a 0.3 M oxalic acid aqueous solution was used as the electrolyte. The cell was placed in a refrigerated circulating bath and the electrolyte was vigorously stirred to equilibrate the temperature. The first step of aluminum foil anodization was carried out under a constant voltage of 40 V at 4˚C. After several hours of anodization, the anodized foil was taken out of the cell and immersed in a mixture of 1.8 wt% chromic acid and 6 wt% phosphoric acid with a volume ratio of 2:8. The sample was etched in this mixture at 60˚C for 40 minutes to remove the anodized layer. After cleaning with water and ethanol, the treated aluminum foil was held in the Teflon cell again

for the second step of anodization, the parameters of which are the same as those in the first step. Anodization time was controlled to get p-AAO membranes with desired thicknesses. After anodization, the pores of p-AAO membranes were widened by chemical etching in a 5% aqueous phosphorous acid at 30˚C for 40 minutes to get a larger pore diameter.

2.3.1.2 Preparation of p-AAO Membranes Anodized at 180V

As the cell diameters (distance between adjacent pore centers) of p-AAO membranes are linearly related to the anodization voltages (in the range of 20 to 195V),[6,7] cell diameters can be finely controlled. However, for each electrolyte composition there is an optimal anodization voltage to get highly ordered porous structures. Therefore, optimization of both of these parameters is required for a desired cell diameter. Although there are several previous publications on this topic,[6,7] the reported experimental conditions produced inferior membranes for my experiment. Fabrication of p-AAO membranes with the largest cell diameters used the following experimental conditions. The first step of anodization was conducted using a 10 wt% aqueous phosphoric acid solution as electrolyte starting at 195 V, which is close to the breakdown potential of anodic aluminum oxide (breakdown potential ~ 195 V in 0.1 M phosphoric acid[8]). After around ten minutes (aluminum oxide layer tends to breakdown for a longer time), the anodization voltage was lowered to 175 V and kept at this voltage for one to two hours. Since heat aggregation is serious at high anodization voltage, the temperatures of electrolytes need to be kept around 0 ˚C at all times. Otherwise, the exothermic anodization of aluminum along with ohmic heating increases the temperature of the aluminum foil and electrolyte quickly, which in turn makes the anodization accelerate and release more heat. The reaction would be out of control in a short time. After removing the

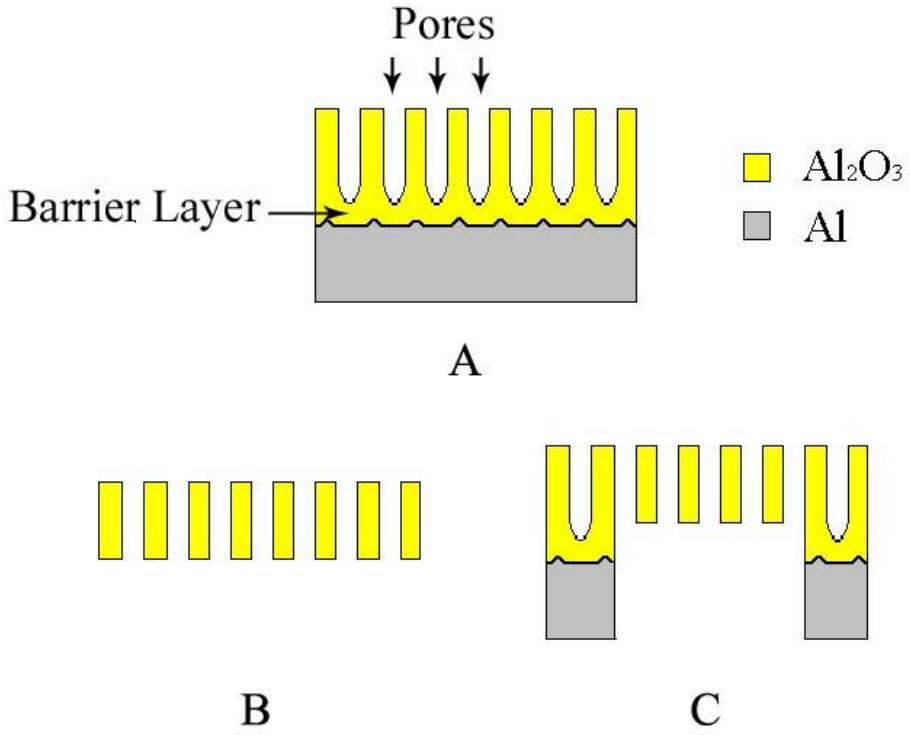

Figure 2-3. Schematic diagrams (cross sections) of p-AAO membranes with penetrated channels.
The Al substrate and barrier layer are (B) completely or (C) selectively chemically etched away from (A) the p-AAO membrane after two-step anodization. To make structure (C), part of aluminum substrate is first protected with a thin layer of nail polish before etching.

anodized layer, the second anodization was carried out in 0.3 M phosphoric aqueous solution at 180V. The pore enlargement reaction was conducted in a 5 wt% phosphoric aqueous solution at 30˚C for 40 minutes.

2.3.1.3 Fabrication of p-AAO Membranes with Nanochannels Open on Both Ends

After the anodization of aluminum foil, one end of the p-AAO membrane is open and the other end is closed (Figure 2-3A). To open the other end and produce penetrated channels, both the aluminum substrate and the barrier layer need to be removed. By selectively etching, either a freestanding p-AAO membrane (Figure 2-3B) or a p-AAO membrane partly supported by aluminum (Figure 2-3C) could be fabricated. Two methods could be used to remove the aluminum substrate. One is chemical etching in copper chloride and hydrochloric acid.[9] The other is electrochemical etching in perchloric alcohol solution at high current (as used in electrochemical polishing). The exposed barrier layer could be etched away in 5 wt% phosphoric acid at 30 ˚C. For p-AAO membranes anodized at 40V, the barrier layer could be removed in 90 minutes; for p-AAO membranes anodized at 180V, it needs around 5 hours. To avoid the pore enlargement etching at this step, the top surfaces of p-AAO membranes were protected by nail polish. After pore opening, the nail polish was washed away by acetone.[9] To make structures as shown in Figure 2-3C, part of aluminum substrate is first protected with a thin layer of nail polish before etching. The unprotected aluminum substrate can be etched away as previously stated.

2.3.2 Results and Discussion

2.3.2.1 Characterization of p-AAO Membranes Anodized at 40V

Figure 2-4 shows the surface structures of a sample at different stages of anodization. During the electrochemical polishing process, the rough structures of aluminum foil (Figure 2-4A) were smoothed, producing a flat and shiny surface (Figure 2-4B). Figure 2-4C, the top view FE-SEM image of the p-AAO membranes after the first step of anodization, shows the porous structure on the surface, which is the result of competition between the formation and electric-field-assisted dissolution of anodized alumina. The pores are randomly distributed, since at the beginning of the first-step anodization, pores grow randomly on sites where the oxide coverages are thinner. Figure 2-4D shows the FE-SEM image of aluminum foil after stripping the porous oxide layer after the first step of anodization. Uniform dents are hexagonally packed on the surface, which is the result of self adjustment of pore channels during the first step of anodization.[10] This close-packed dent structure serves as an master for the second anodization step, i.e., pores form at the bottom of each dent in the second step of anodization.

Uniform p-AAO membranes were prepared after the second step of anodization. Figure 2-5A, the top view of a p-AAO membrane, indicates that the pore openings on the surface are hexagonally close-packed and around 25 nm in diameter. Figure 2-5B shows the surface structure of the p-AAO membrane after pore enlargement in 5 wt% phosphoric acid, which clearly illustrates that the sizes of pores increase from 25 nm to 70 nm. Cell diameter is around 110 nm, which is determined by the anodization voltage and temperature, and does not change during the pore enlargement treatment. Figure 2-5C and D are cross-sectional views of the p-AAO membrane showing that all of the nanopore channels are reasonably straight and parallel and traverse the entire thickness of the porous membrane.

Figure 2-6 shows the current vs. time curve of the first and second steps of

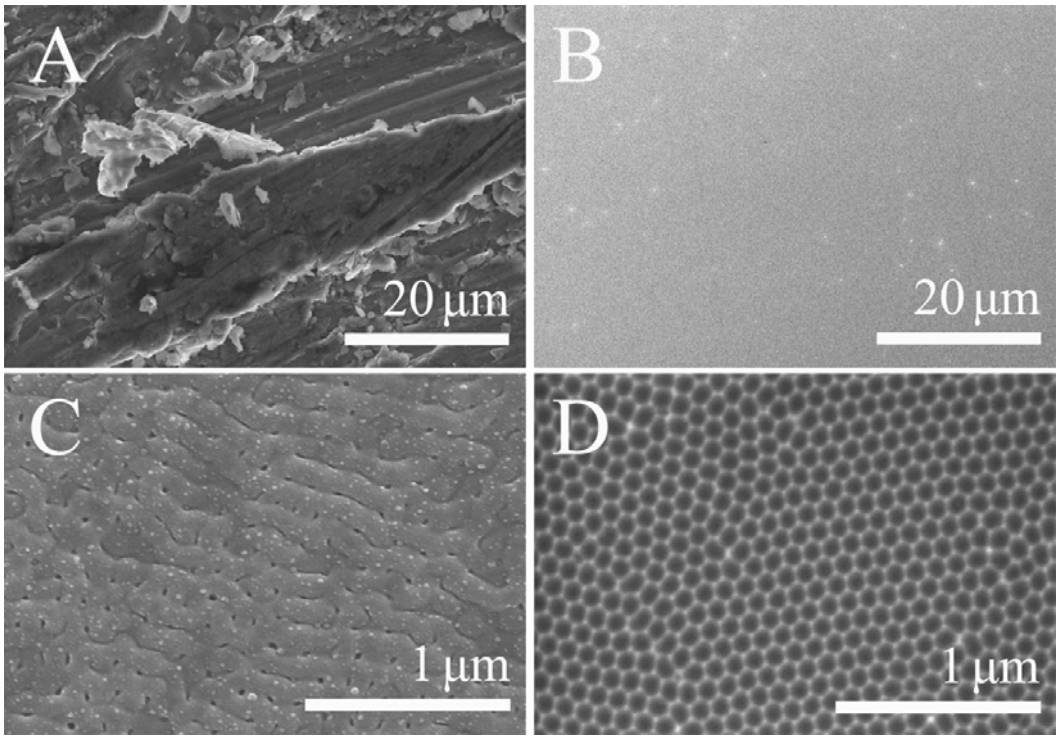

Figure 2-4. Surface structures of sample during anodization.
FE-SEM images of high purity aluminum foil (A) before and (B) after electrochemical polishing in a mixture of perchloric acid (70%) and ethanol with a volume ratio of 3:7 at a constant current of 100 mA for 4 minutes, (C) after the first-step anodization at 40V in 0.3 M oxalic acid aqueous solution at 4 ˚C, and (D) after stripping the anodized alumina layer using a mixture of 1.8 wt% chromic acid and 6 wt% phosphoric acid with a volume ratio of 2:8 at 60˚C.

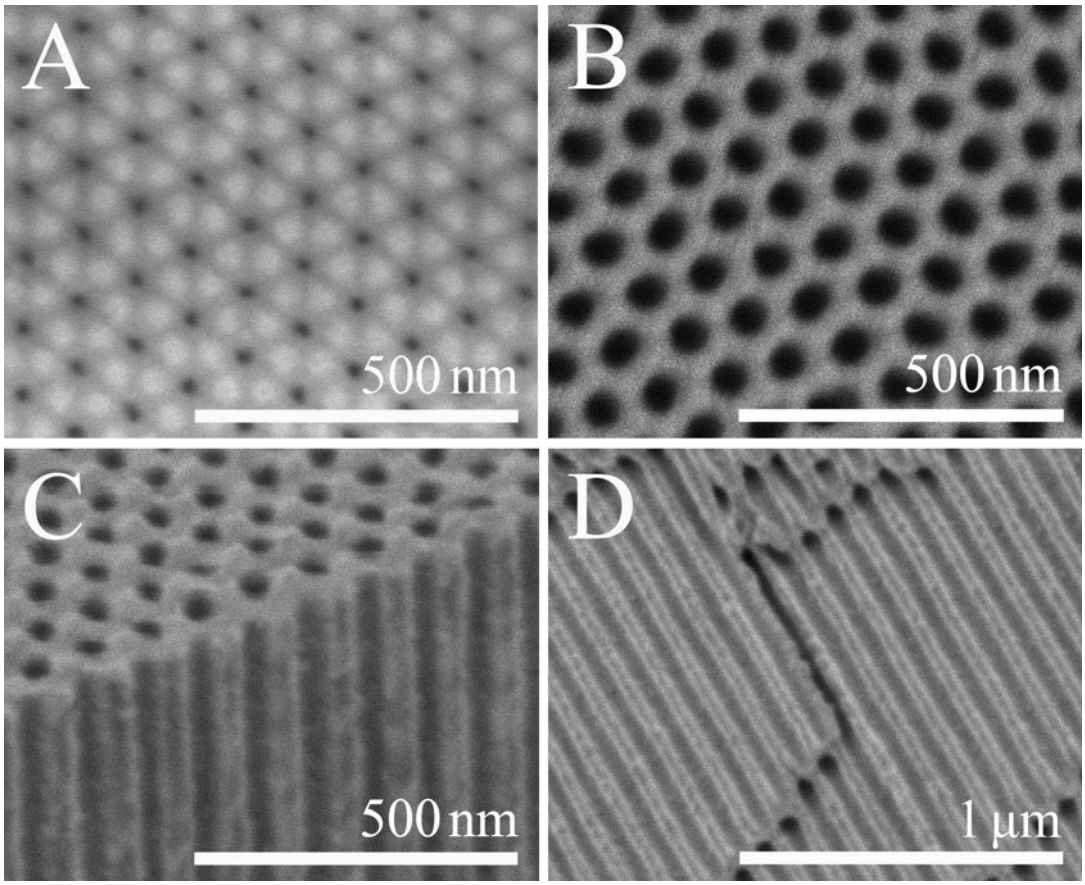

Figure 2-5. Structures of a p-AAO membrane anodized at 40V.
(A) FE-SEM micrograph of p-AAO membranes after the second step of anodization at 40V in 0.3 M oxalic acid aqueous solution at 4 ˚C. FE-SEM micrographs of (B) top and (C), (D) cross-sectional views of p-AAO membrane anodized at 40V after pore enlargement in 5 wt% phosphoric acid aqueous solution at 30 ˚C for 40 minutes.

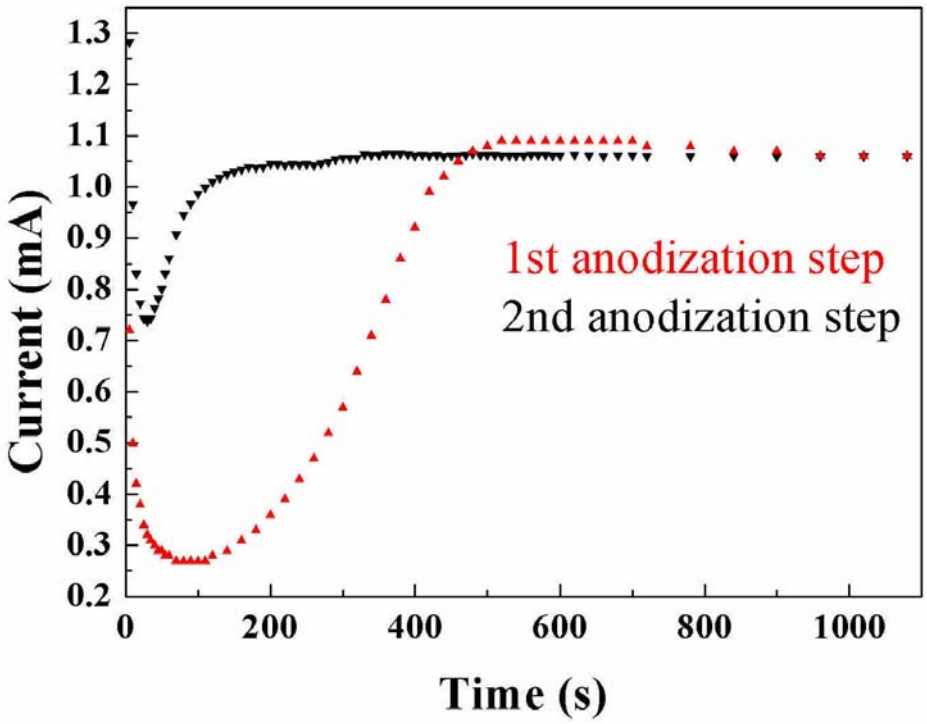

Figure 2-6. Current vs. time anodization curves.
Current vs. time curves of the first and second steps of anodization at 40V in a 0.3 M oxalic acid aqueous solution at 4 ˚C.

anodization at 40V in 0.3M oxalic acid. Current decreases at the beginning of anodization because of the formation of anodized alumina under high initial current, which greatly reduces the conductivity. Then electric-field-assisted dissolution of alumina takes place and reduces the thickness of alumina layer. This process increases the anodization current. After reaching equilibrium, the thickness of the barrier layer does not change any more and the anodization current becomes stable. The second step of anodization starts with regular dents as a master, and therefore the stabilization process is much faster than that of the first step. Because the same anodization conditions were applied to both the first and second steps of anodization, the final stabilized anodization current is the same.

2.3.2.2 Characterization of p-AAO Membranes Anodized at 180V

The size of pores is much larger for p-AAO membranes anodized at 180V. Figure 2-7 shows the anodization of aluminum at 180V at different stages. After stripping the anodized layer from the first anodization, hexagonally close-packed dents appear on the surface of aluminum foil (Figure 2-7A) just as in the case for p-AAO membranes at 40V. Figure 2-7B shows the FE-SEM images of p-AAO after the second anodization. Pore structures with diameters around 110 nm are hexagonally close-packed. After chemical etching, the pore diameters are enlarged to around 160 nm (Figure 2-7C). The porous channels are straight and parallel with each other, as shown in Figure 2-7D. The cell diameter of p-AAO membrane anodized at 180 V is around 400nm.

2.3.2.3 Characterization of Homemade p-AAO Membranes with Nanochannels Open on Both Ends

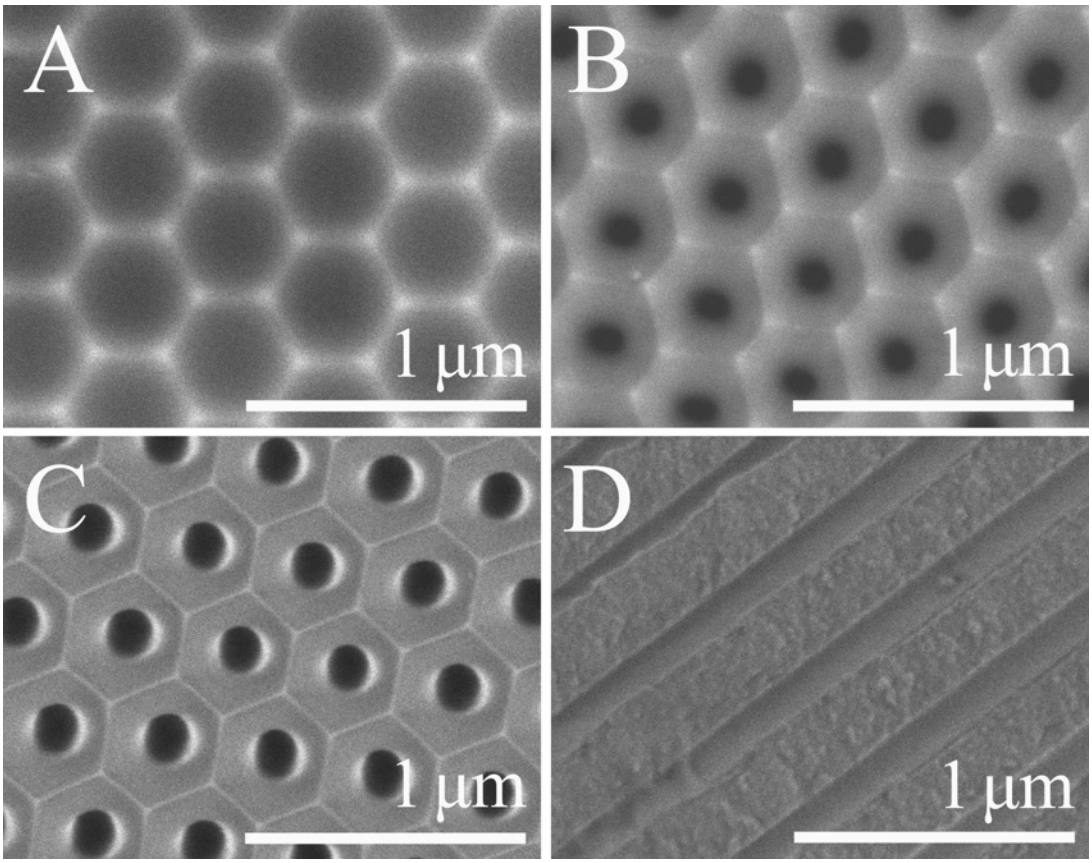

Figure 2-7. Structures of a p-AAO membrane anodized at 180V.
FE-SEM images of aluminum foils (A) before and (B) after the second step of anodization at 180V in 0.3 M phosphoric acid aqueous solution. FE-SEM images of (C) top and (D) cross-sectional views of p-AAO membranes anodized at 180V after pore enlargement in 5 wt phosphoric acid aqueous solution at 30 ˚C for 40 minutes.

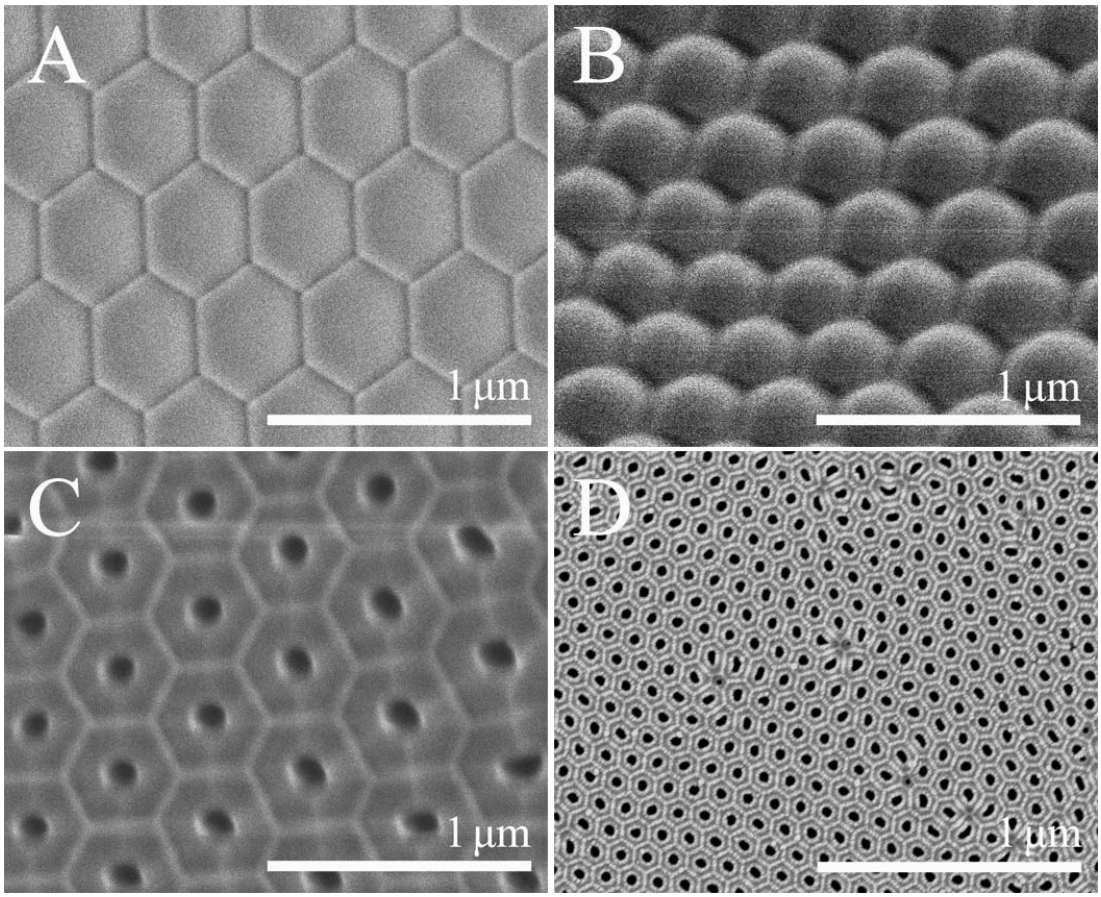

Figure 2-8. Structures of p-AAO membranes before and after stripping the barrier layers.

FE-SEM images of (A) vertical and (B) 30˚ views of the barrier layers of a p-AAO membrane anodized at 180V in 0.3 M phosphoric acid aqueous solution. FE-SEM images of back sides of p-AAO membranes anodized at (C) 180V and (D) 40V after removing the barrier layers.

After stripping the aluminum substrate (see Figure 2-3A), the barrier layer sandwiched between the porous alumina and aluminum substrate is exposed. Figure 2-8A and B show the FE-SEM at different angles of the barrier layer structure from a p-AAO membrane anodized at 180V. The barrier layers are hexagonally packed half-spheres composed of alumina, which could be chemically etched by phosphoric acid. After etching, nanochannels are open at this end (Figure 2-8C). The diameter of openings is 110nm, which is almost the same as the size of pore openings on the other end (Figure 2-7B). Figure 2-8D is the FE-SEM image showing openings around 30nm in diameter of a p-AAO membrane anodized at 40V, which also matches the size of openings on the other end (Figure 2-5A). These results further confirm that the channels of p-AAO membrane are straight and uniform along their whole length.

2.4 Fabrication of Silver Nanorod Arrays by Electrodeposition

2.4.1 Introduction

P-AAO membrane templates have been used to make many types of nanomaterials. The most popular is the electrodeposition of metals into nanochannels to form nanorods.[11-13] Either AC or DC voltage can be used. However, a thin layer of alumina, the barrier layer, is between the porous oxide and aluminum substrate after the anodization. Since it is a layer of insulator, high potential is required for electrons to tunnel through the barrier layer. However, high cathodic potentials may cause several problems, such as hydrogen evolution,[14] which would inhibit metal deposition. To overcome this problem, the general procedure[12,13] is to strip the aluminum substrate and barrier layer to form a freestanding p-AAO membrane with both nanochannel ends open (as stated in 2.3.1.3). Then a thin layer of metal (usually Au, Ag)

is sputter coated on one side of the membrane for better conduction. This conducting layer functions as the working electrode for deposition. Afterwards, metal can be electrodeposited into the channels of p-AAO membrane using AC or DC voltage. After removing the sputter-coated metals, and the p-AAO membrane, separated metal nanorods can be achieved. This whole process requires many steps and large amounts of wasted materials.

Taking another perspective, the aluminum layer is conductive and could function as the working electrode as long as the barrier layer is thin. The barrier layer thickness is linearly related to the anodization voltage (1-1.2 nm per volt oxidation potential);[15] therefore, it could be thinned by reducing the anodization voltage at the end of the second anodization step.[14,16] Metal could then be electrodeposited into the channels at a much lower potential.

For their special optical and electronic properties,[17,18] silver rods have been prepared by several methods, including wet chemical synthesis,[19] ultraviolet irradiation photoreduction,[20] solid-liquid-phase arc discharge,[21] and template methods.[22,23] Fabrication of silver nanorod arrays was also reported using vapor deposition,[24] which can produce large enhancements in surface-enhanced Raman scattering (SERS) experiments. However, a complicated oblique-angle deposition system is required.

In this section, the fabrication of silver nanorod arrays by a simple electrodeposition method is presented. By exchanging the sequence of voltage reduction step and pore enlargement step,[14] part of the bottom of each pore could be opened. Aligned silver nanorod arrays could then be easily fabricated by electrodeposition into the treated p-AAO membrane template.

2.4.2 Experimental

After two-step anodization at 40V, the p-AAO membrane was further treated to open part of the pore bottom. During the experiments, p-AAO membrane was stuck to the Teflon cell continuously. Electrolyte and power supply connections were changed for anodization and electrodeposition.

As shown in Figure 2-9, the barrier layer of p-AAO template was thinned by gradually reducing the anodization voltage to around 2.0 V. Then the 0.3 M oxalic acid solution was replaced by a 5 wt% phosphoric acid aqueous solution for pore enlargement. The p-AAO membrane was etched for 40 minutes at 30 °C. Afterwards, the phosphoric acid aqueous solution was depleted and the template was cleaned in the Teflon cell with distilled water several times to remove the remaining phosphoric acid in the p-AAO membrane nanochannels. This step is very important, since silver salt may react with phosphoric acid and form insoluble silver(I)phosphate (k_{sp} $8.89*10^{-17}$ at 25 ˚C) and block the nanochannels. Then, Technic silver plating solution was added to the Teflon cell with the p-AAO membrane connected to the cathode of power supply. Electrodeposition of silver was carried out at a potential of 2V for 4 minutes. The deposition current was around 0.8 mA. Finally, the p-AAO template with silver deposited was taken out of the Teflon cell and immersed in a chromic acid and phosphoric acid solution to remove the p-AAO template. After cleaning, silver nanorod arrays standing on the aluminum substrate were exposed.

2.4.3 Results and Discussion

The treated p-AAO membranes and silver nanorod arrays were characterized using FE-SEM. Figure 2-10A shows the channels near the bottom of p-AAO membrane. The pore bottoms were partially opened and the nanochannels of the p-AAO membrane were

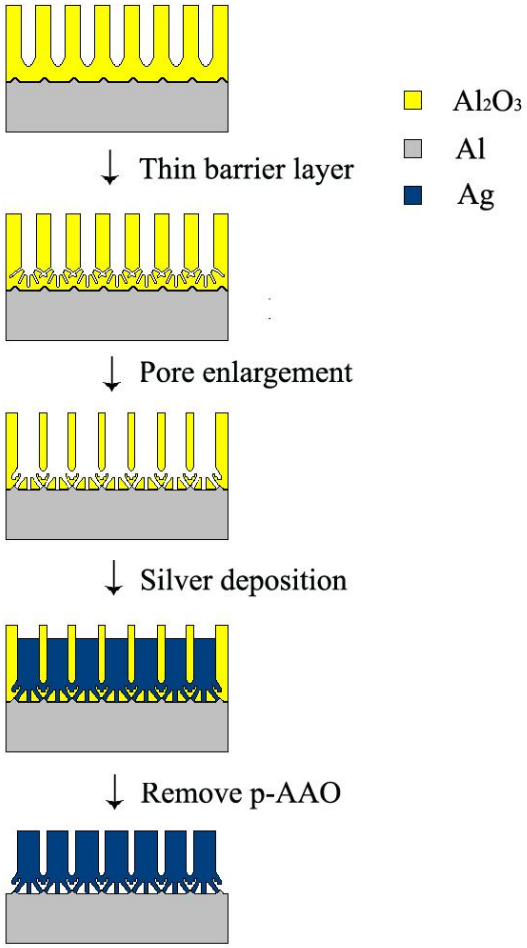

Figure 2-9. Schematic diagram of the fabrication of silver nanorod arrays using a treated homemade p-AAO membrane template.
By reduction of anodization voltage, the barrier layer of prepared p-AAO membrane template is thinned due to the formation of fibrous channels. The followed pore enlargement process partially opens the barrier layer. Electrodeposition of silver in nanochannels of treated p-AAO membrane is conducted at a potential of 2V for 4 minutes. After removing the porous template, silver nanorod arrays standing on the aluminum substrate are exposed.

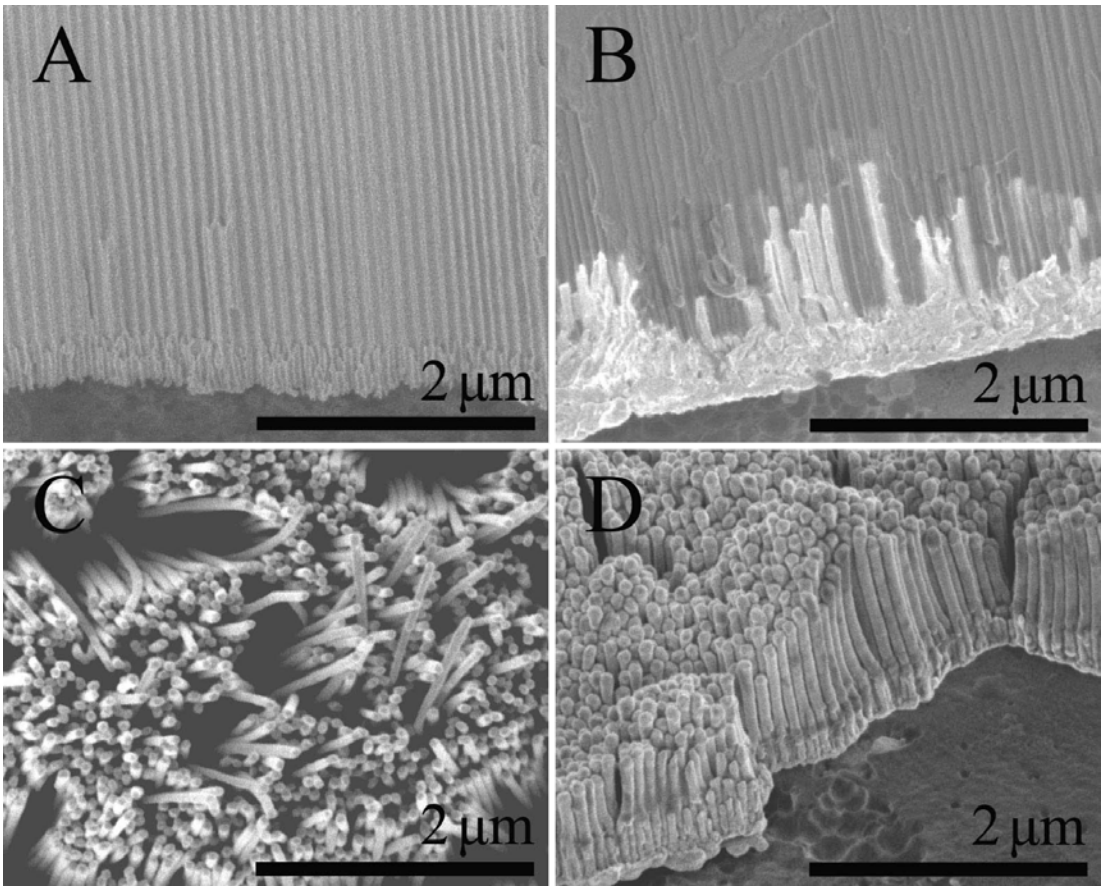

Figure 2-10. Structure of silver nanorod arrays fabricated by electrodeposition in a treated p-AAO template.
FE-SEM image of (A) a treated p-AAO membrane with barrier layer partly removed, (B) silver nanorods electrodeposited in the nanochannels of a treated p-AAO membrane. FE-SEM images of (C) top and (D) cross-sectional views silver nanorod arrays after removing the p-AAO substrate.

connected to aluminum substrate by much thinner nanochannels. Silver nanorods in the p-AAO template are shown in Figure 2-10B. Silver filled the bottom part of most of the channels. After removing the p-AAO template, silver nanorod arrays standing on aluminum substrate were exposed. Figure 2-10C and D are the top and 30 degree views of the silver nanorod arrays. The nanorod diameters, around 70nm, are very uniform and match the diameter of channels, but the lengths are variable. This may be due to the slight difference between fine bottom structures from channel to channel. The electrodeposited silver nanorods are connected with each other and beneath aluminum substrate. Further optimization of experimental conditions is needed to make equal-length silver nanorod arrays.

2.5 *In-situ* Electrochemical Synthesis of 1-Dimensional Alumina Nanostructures

2.5.1 Introduction

The unique properties and potential applications of 1-D nanostructures (nanotubes, nanowires and nanorods) in optical, electronic, magnetic and mechanical devices continue to attract attention.[25-29] Alumina nanowires and nanotubes exhibit a high dielectric constant, high thermal and chemical stability, and high elastic modulus, thereby making alumina nanostructures useful in advanced high-temperature composite materials, catalyst beds and nanodevices.[30,31] Considerable effort has gone into obtaining 1-D alumina nanostructures and several synthetic methods have been reported: catalyst-assisted vapor-liquid-solid deposition,[32-35] catalyst-free vapor-solid deposition,[36-39] template methods,[40,41] chemical etching methods,[42-44] and mechanical cleavage of porous aluminum oxide (p-AAO) membranes.[45] Although various synthesis methods have their strong points, most reported methods exhibit some drawbacks: thermal vapor deposition requires special conditions (e.g.

high temperatures >1000˚C), the template method necessitates fabrication of nanostructures (nanotubes or a nanoporous membrane), the chemical etching method requires p-AAO membrane precursors, and mechanical membrane cleavage cannot provide large amounts of product.

In this section, we report a high yield of 1-D alumina nanostructures synthesized via controlled anodization of aluminum foil without the involvement of extreme conditions, complicated setups, or template preparation and removal. Although aluminum anodization has been used for p-AAO membrane fabrication for a long time,[3] we find that alumina nanowires, nanofascias, and nanotubes can be electrochemically synthesized in-situ on the surface of a p-AAO membrane by controlling the anodization temperature, voltage, and time.

2.5.2 Experimental

The same Teflon cell and setup (Figure 2-2) was used for the synthesis of 1-D alumina nanostructure. 10 wt% phosphoric aqueous solution was used as the electrolyte. High purity aluminum foil was anodized at 137V with a cooling bath temperature of 10 ˚C for 18 hours following the well-known two-step procedure.[3,6,7] There was an equilibrium between the bath temperature and the electrolyte temperature. The anodization temperature at the bottom of the p-AAO pores was assumed to be the same as that of the electrolyte. The anodization temperature at the interface of Al and Al2O3 was not accessible, however the electrolyte temperature stabilized in less than half an hour to the cooling bath temperature and small changes in the latter temperature induce profound changes in the AAO morphology. The anodization did not commence until thermal equilibrium was established. After the anodization commenced, a new thermal equilibrium was established (~ 0.5 h time scale) and

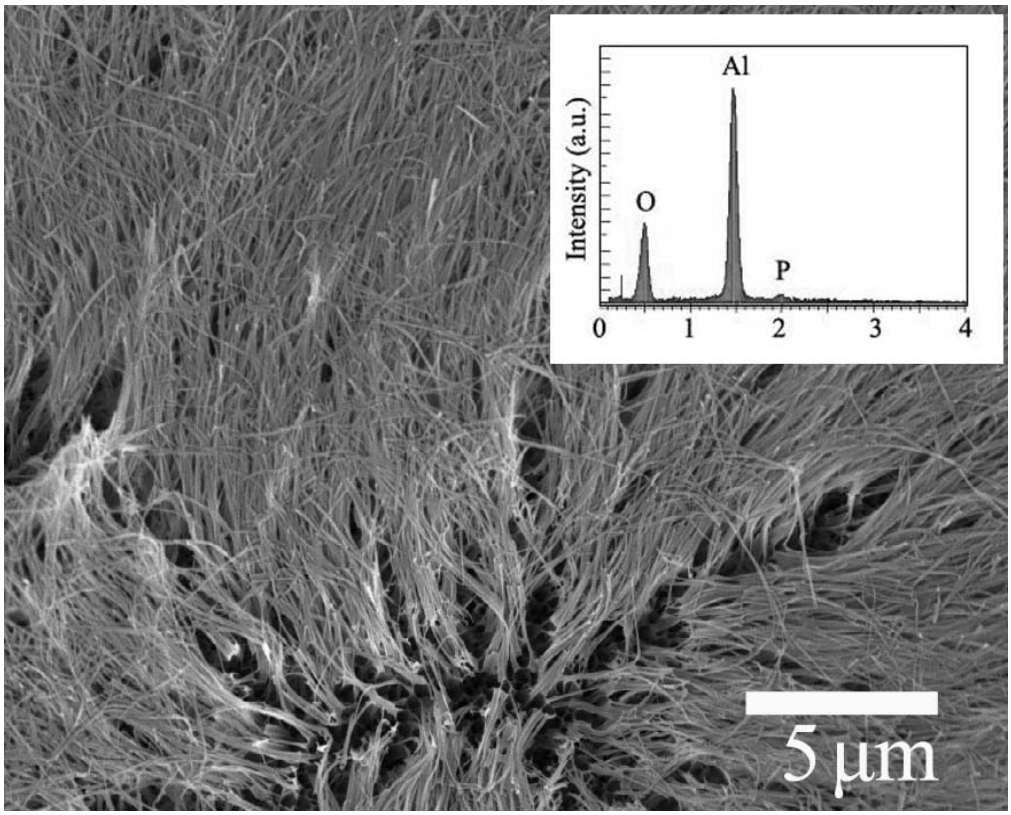

Figure 2-11. 1-D alumina nanostructures and their composition.
SEM image of 1-D fibrous alumina nanostructures produced at an anodization voltage of 137V in 10 wt% phosphoric acid aqueous solution for 18 hours with a cooling bath temperature of 10˚C. The upper-right inset is an EDX spectrum of the as-prepared alumina nanostructures.

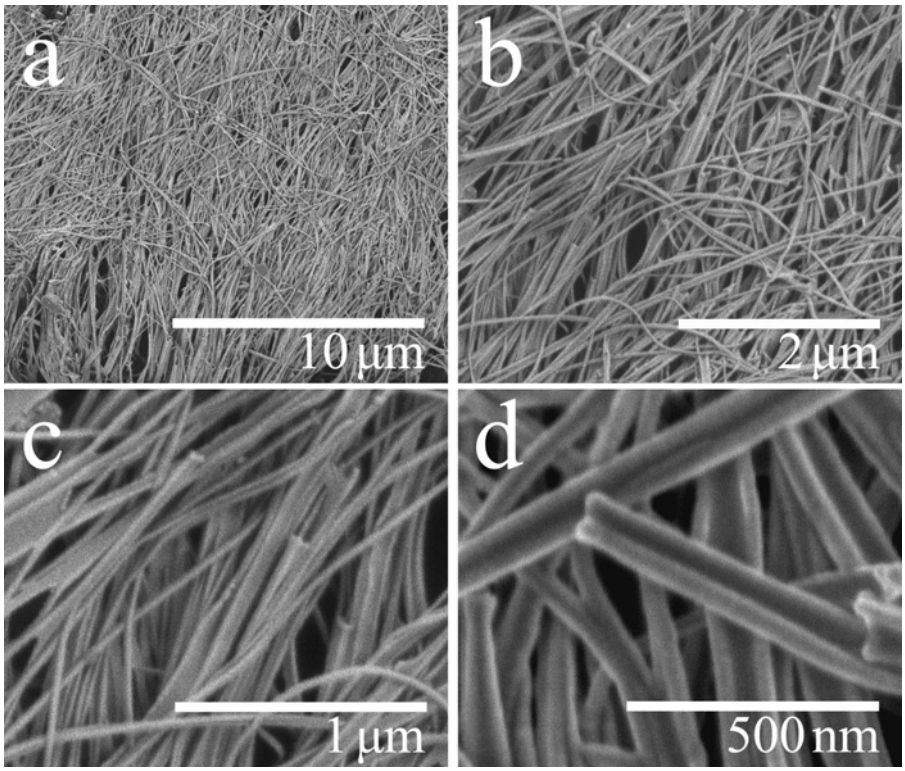

Figure 2-12. 1-D alumina nanostructures at different magnifications.
FE-SEM images at different magnifications of 1-D alumina nanostructures produced at an anodization voltage of 137V in 10 wt% phosphoric acid for 18 hours with a cooling bath temperature of 10˚C.

the bulk of the anodization occurred at that temperature, which was around 4 ˚C higher than the cooling bath temperature.

A thin layer of gold (~10nm) was sputter coated on an as-prepared sample before SEM and FE-SEM characterization. For TEM observations, an as-prepared sample had been sonicated in ethanol for several minutes before a drop of the solution was placed on the Cu grid.

Control experiments were carried out using the same apparatus at different cooling temperatures and for different anodization times.

2.5.3 Results and Discussion

2.5.3.1 Morphologies of 1-D Alumina Nanostructures

The morphologies of the anodized products were characterized using SEM and FE-SEM. Figure 2-11 shows a SEM image of the as-prepared fibrous nanostructures, which are tens of microns long and cover the entire anodized surface. The upper-right inset in Figure 2-11 is the EDX spectrum of the 1-D alumina nanostructure showing that the product contains only the elements Al, O, and a very small amount of P; the latter comes from contamination by the electrolyte, a well-known characteristic of p-AAO preparation.10 FE-SEM images at different magnifications was shown in Figure 2-12. These indicate that the fibrous nanostructures are comprised of nanowires, fascias or partial tubes.

2.5.3.2 Cross-section Structures of the Anodized Al Foil

In order to understand the formation mechanism of 1-D alumina nanostructures, the cross-section of a sample was characterized by SEM and FE-SEM. The cross-sectional SEM

image (Figure 2-13) shows a dense layer of 1-D fibrous nanostructures nearly 10 μm thick on the surface of a contiguous solid phase, which is the usual product of anodization — an alumina layer ~50 μm thick punctuated with nearly hexagonally spaced nanochannels. The fibrous upper layer is separated from the porous alumina by a ~15 μm thick transition layer. Figure 2-14A is a magnified image of the fibrous alumina 1-D nanostructures on the upper surface taken by FE-SEM and is similar to Figure 2-12. Nanowires with diameters of nearly 30 nm and nanofascias with transverse dimensions around 100 nm are shown in the image. Figure 2-14B shows the transition layer from 1-D nanostructures to nanochannels. In the transition region, the alumina nanochannels are fragile and readily disintegrate producing many broken alumina fragments. Figure 2-14C shows the parallel and straight nanochannels of the usual p-AAO product, a membrane beneath the transition layer.

2.5.3.3 Crystallinity of 1-D Alumina Nanostructures

The crystalline phase of the exterior of the 1-D alumina nanostructures was characterized using SAED and XRD. Figure 2-15 shows a TEM image of an isolated alumina partial nanotube with an outer diameter around 220 nm. The upper-left inset is the SAED pattern of this nanotube. Broad rings suggested that the alumina nanotube is amorphous. XRD results from alumina nanostructures (fibrous nanostructure, transition zone, and underneath p-AAO) confirm that this is an amorphous phase (Figure 2-16).

2.5.3.4 Results of Control Experiments

Our anodization product is clearly different from the reported conventional structure of p-AAO membranes.[6,7] However, by lowering the cooling temperature to 2 ˚C while keeping all

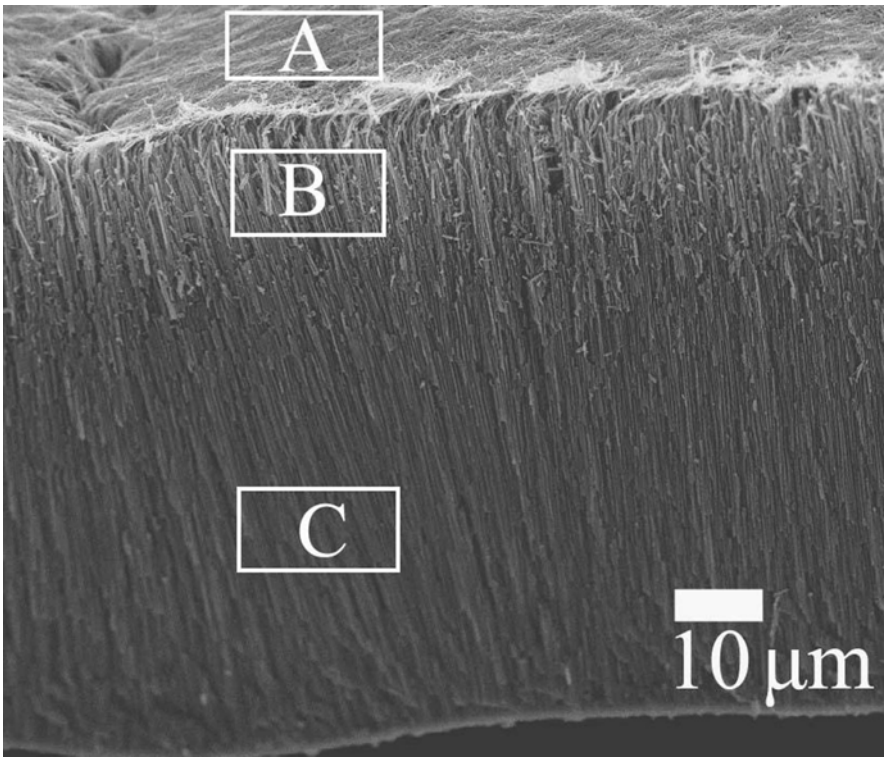

Figure 2-13. A cross-sectional SEM image of as-prepared 1-D alumina nanostructures on a p-AAO membrane.
Enlarged images in A, B and C are shown in Figure 2-14, respectively.

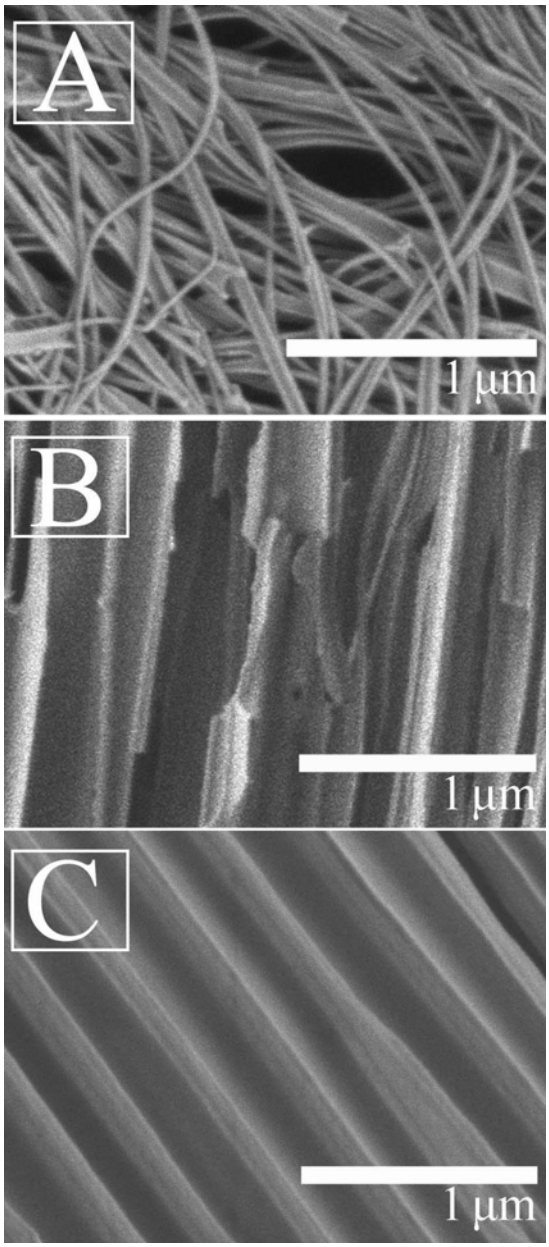

Figure 2-14. Magnified FE-SEM images of different layers.
FE-SEM images of (A) 1-D alumina nanostructures, (B) transition layer and (C) alumina nanochannels are higher resolution images from box A, B and C in Figure 2-13 respectively.

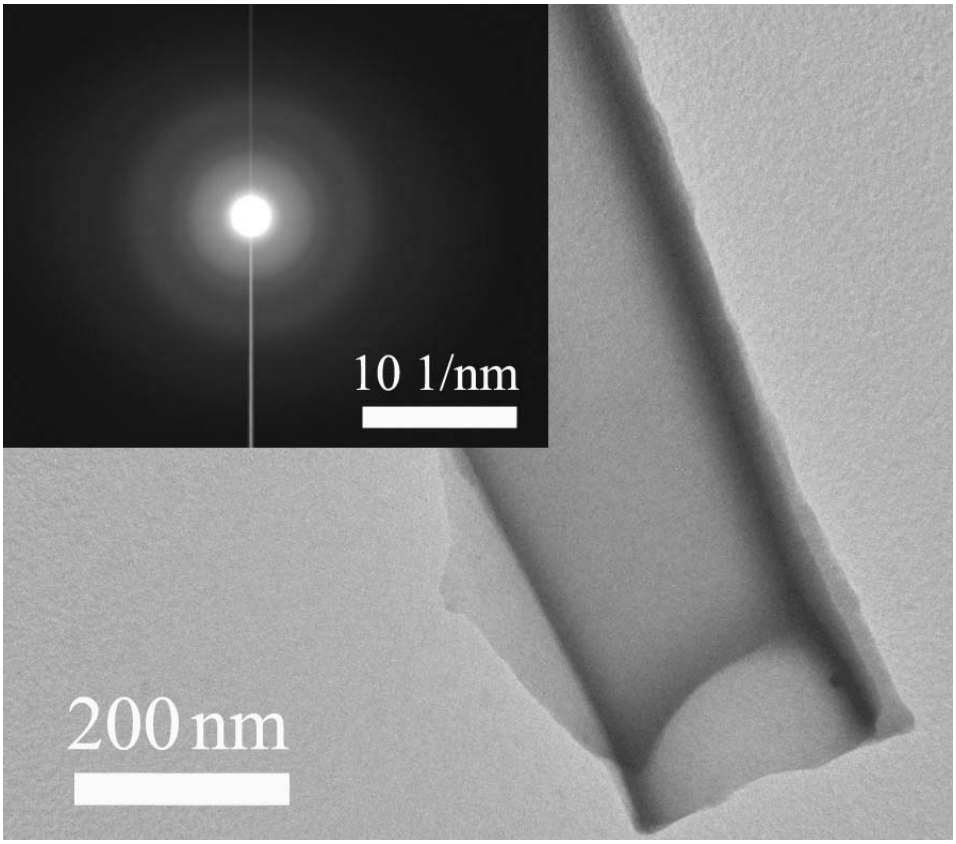

Figure 2-15. TEM image of 1-D alumina nanotube after sonication of as-prepared sample.
The upper-left inset is a SAED pattern of the alumina nanotube.

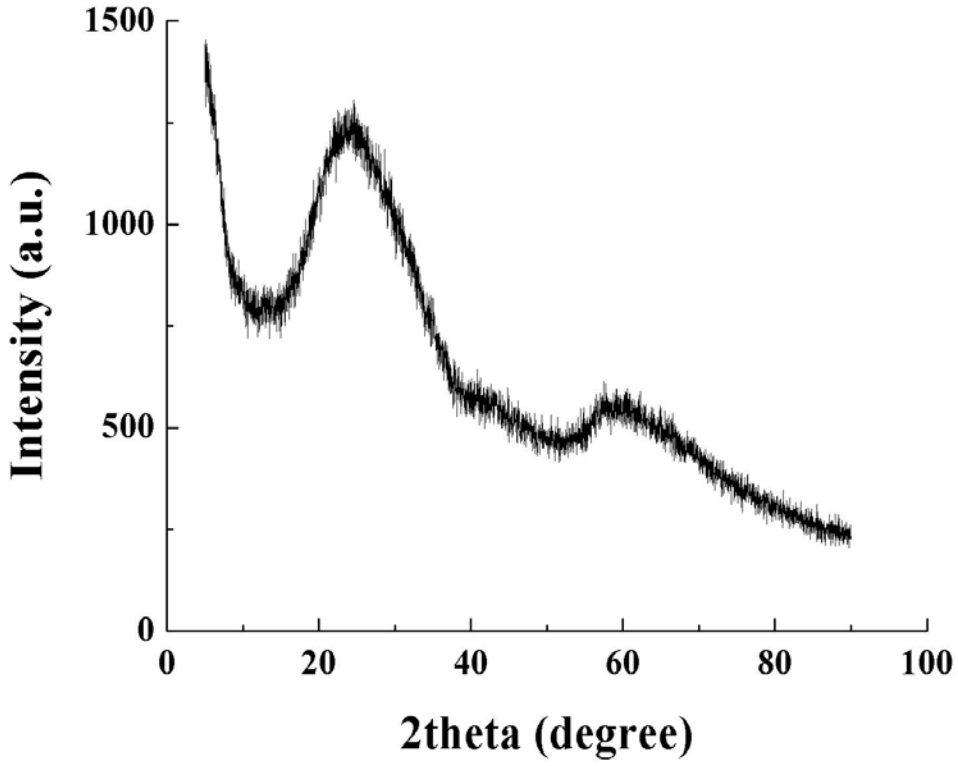

Figure 2-16. XRD result of as-prepared 1-D alumina nanostructures on a p-AAO membrane.

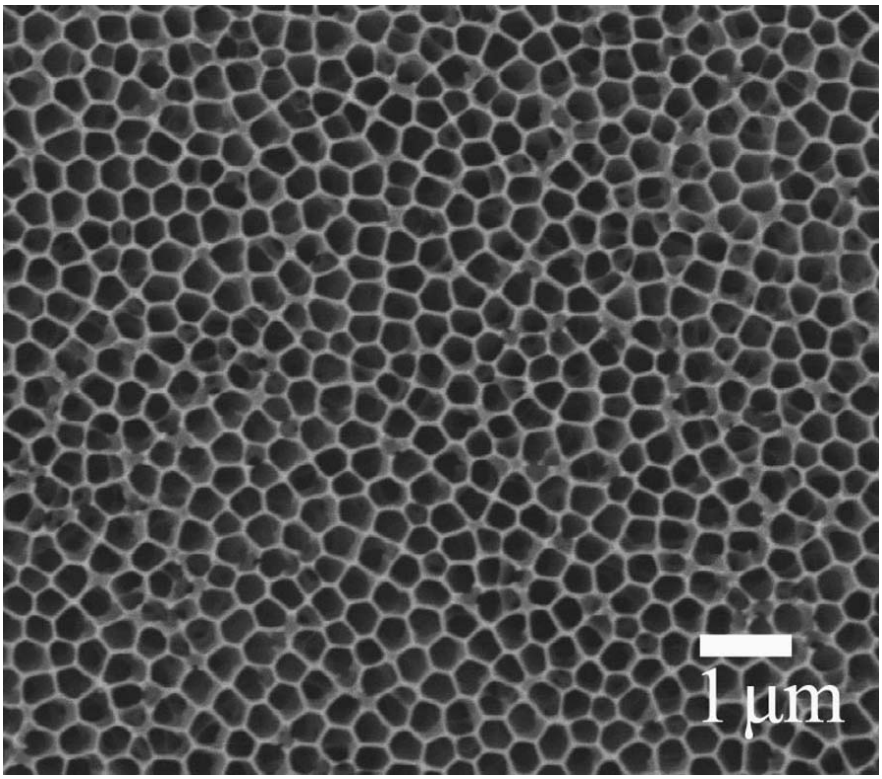

Figure 2-17. SEM image of a p-AAO membrane produced at an anodization voltage of 137V in 10 wt% phosphoric acid for 18 hours with a cooling bath temperature of 2˚C.

of the other parameters the same, a monolithic conventional p-AAO membrane with average pore size of ~250 nm was fabricated without observing any fibrous 1-D nanostructures phase (Figure 2-17). To further understand the mechanism, experiments at different anodization times were carried out. As shown in Figure 2-18, the channel walls became thinner and thinner as anodization proceeds. For anodization times around 9 - 10 hours, large sections of the p-AAO channel walls were etched away and 1-D nanostructures (fibers, fascias and partial tubes) appeared. Additional control experiments with Al foil anodization at different voltages and times are listed in Table 2-1. These experiments suggested that the formation of the different alumina nanostructures (nanowires/nanotubes/nanofascias on the p-AAO membrane surface or just the p-AAO membrane itself) strongly depends on the anodization temperature, the anodization time, and the anodization voltage.

2.5.3.5 Nanostructure Formation Mechanism

Based on these results, a possible mechanism for 1-D alumina nanostructure formation is proposed: during anodization, the alumina growth rate at the metal/oxide interface reaches an equilibrium with an electric-field-enhanced alumina dissolution rate at the oxide/electrolyte interface near the bottom of the pores in the anodized aluminum.[10] A certain amount of oxide produced during the initial anodization (approximately 30% in aqueous 3% oxalic acid solution at 40V)[10] is dissolved in the acidic electrolyte, and the remaining oxide forms the channel walls comprising the conventional p-AAO membrane (Figure 2-19A). Simultaneously, the nanochannel wall edges close to the surface are thinned — the channel diameters are increased — by a slow dissolution of alumina in the electrolyte under the influence of a relatively weak electric field near the external surface (Figure 2-19B).

Table 2-1. Effect of anodization parameters on the formation of different alumina nanostructures. (* Electrolyte temperature is around 4˚C higher than cooling bath temperatures)

Cooling Bath Temperature* (˚C)	Anodization Voltage (V)	Electrolyte	Anodization Time (h)	Products
2	137	10 wt% phosphoric acid	18	p-AAO membrane
5	137	10 wt% phosphoric acid	10	p-AAO membrane
5	137	10 wt% phosphoric acid	23.5	1-D nanostructures
10	137	10 wt% phosphoric acid	6	p-AAO (Figure 2-18b)
10	137	10 wt% phosphoric acid	10	1-D nanostructures (Figure 2-18d)
10	137	10 wt% phosphoric acid	18	1-D nanostructures (Figure 2-11)
10	40	10 wt% phosphoric acid	24	p-AAO membrane

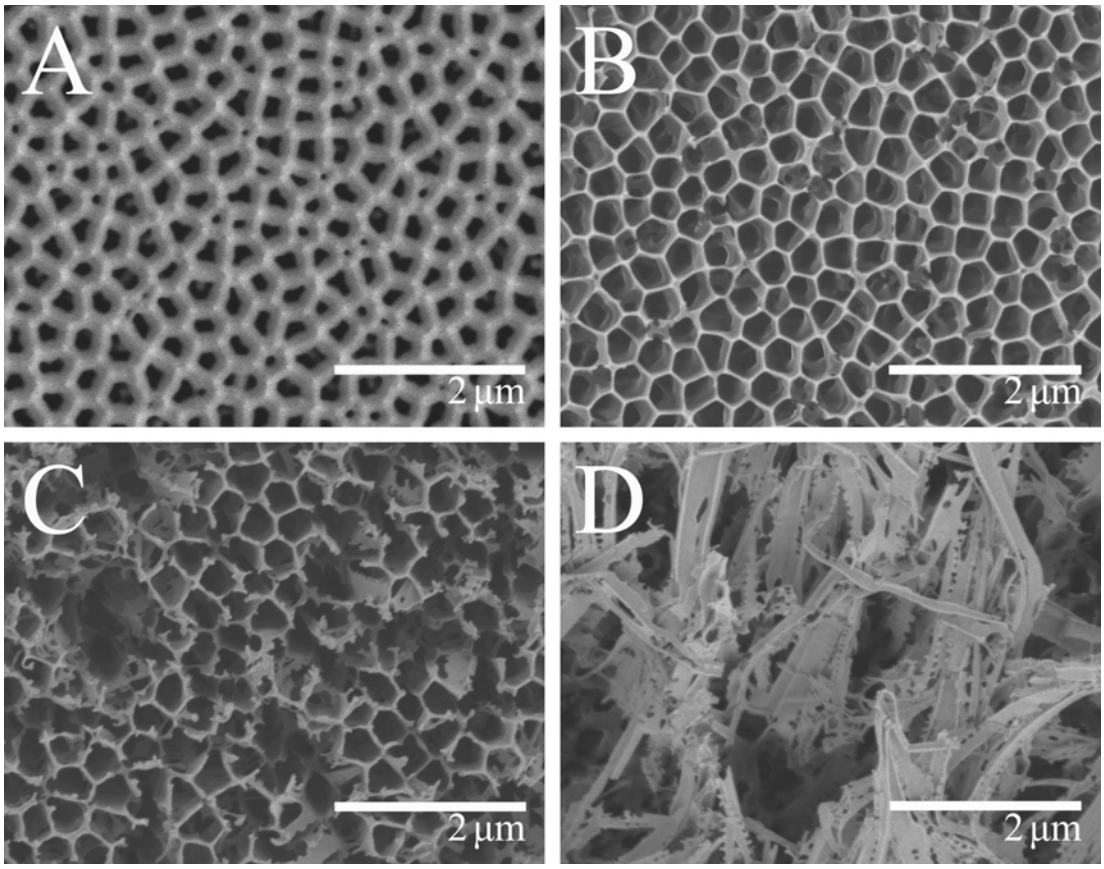

Figure 2-18. SEM images of p-AAO membranes produced with different anodization times.
SEM images of p-AAO membrane at an anodization voltage of 137V in 10 wt% phosphoric acid for A) 1 hour, B) 6 hours, C) 9 hours, and D) 10 hours with a cooling bath temperature of 10˚C.

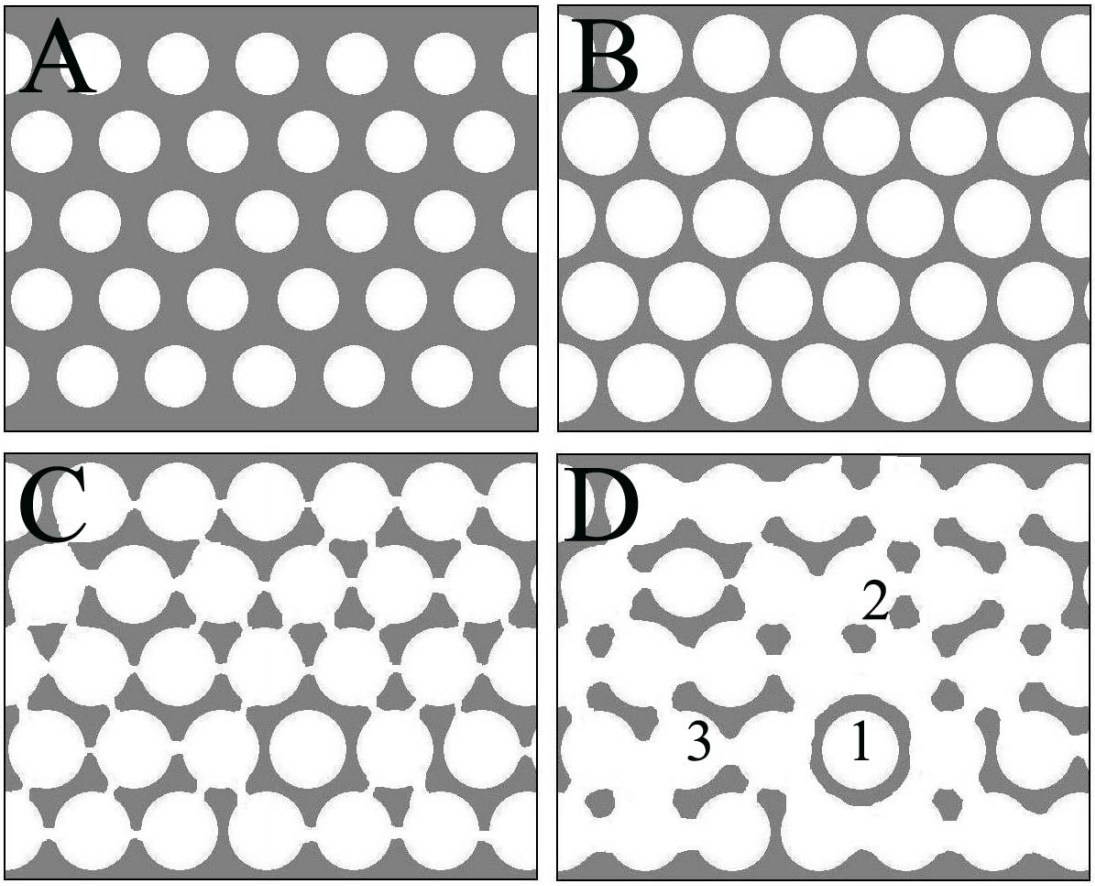

Figure 2-19. Schematic diagrams (top-view) of the possible formation stages of 1-D alumina nanostructures.
(A) Fresh alumina nanochannels. (B) Surface channel walls are thinned by slow dissolution for several hours under the effect of the weak electric field. (C) Perforations form on surface channel walls. (D) Alumina nanotubes, nanowires and nanofascias are created (1, 2 and 3, respectively).

If the anodization voltage and anodization temperature are appropriate, after several hours the surfaces of the channel walls are perforated at the thinnest points (Figure 2-19C). However, if the anodization temperature is sufficiently low or the anodization voltage is quite low, the alumina channel walls retain their shape for a much longer time. Due to the relatively high surface energy and possibly enhanced electric field at sharp edges, the perforated areas tend to dissolve even faster. Consequently, the gaps become larger and the nanochannels exhibit longitudinal fractures. If perforations occur on all of the neighboring junctions of a given pore, an isolated nanotube forms (Figure 2-19D.1). If perforations occur on adjacent tubes, “coordinated” nanowires and nanofascias form on the exterior of the intact nanotubes or nanochannels (Figure 2-19D.2). At intermediate conditions, nanofascias form (Figure 2-19D.3).

2.5.4 Summary

Temperature affects the electric-field-enhanced structural degradation of oxide during anodization. The degradation products reflect the underlying (approximate hexagonal) symmetry of the p-AAO membrane. The net result is a combination of nanotubes, wires, and fascias. SAED and XRD indicate that the 1-D alumina nanostructures are amorphous. This in turn could be exploited as the amorphous nature of the fibrous nanostructures might make it possible to obtain 1-D nanostructures with controllable crystallinity (by annealing[46]) and makes doping by post-treatments feasible.[47]

2.6 Concluding Remarks

By optimizing anodization voltage and electrolyte, p-AAO membranes with different

cell diameters could be fabricated by a two-step anodization of highly pure aluminum foil. The pores of p-AAO membranes are uniform and hexagonally packed. Thickness of the p-AAO membranes could be controlled by anodization time. The pore diameter determined by anodization voltage could be further adjusted by post pore-enlargement etching.

1-D alumina nanostructures could be fabricated using the same apparatus under appropriate electric-field-enhanced structural degradation by adjusting anodization voltage, temperature and time.

By partly opening the bottom ends of nanochannels in p-AAO membranes, electrodeposition of silver into p-AAO templates could be conducted easily under very low DC voltage. Silver nanorod arrays standing on aluminum foil could be fabricated after removing p-AAO templates.

2.7 References

(1) Martin, C. R. *Science* **1994**, *266*, 1961-1966.

(2) Shingubara, S. *J. Nanoparticle Res.* **2003**, *5*, 17-30.

(3) Masuda, H.; Fukuda, K. *Science* **1995**, *268*, 1466-1468.

(4) Jessensky, O.; Muller, F.; Gosele, U. *Appl. Phys. Lett.* **1998**, *72*, 1173-1175.

(5) Rahman, S.; Yang, H. *Nano Lett.* **2003**, *3*, 439-442.

(6) Masuda, H.; Yada, K.; Osaka, A. *Jpn. J. Appl. Phys.* **1998**, *37*, L1340-L1342.

(7) Li, A. P.; Muller, F.; Birner, A.; Nielsch, K.; Gosele, U. *J. Appl. Phys.* **1998**, *84*, 6023-6026.

(8) Choi, J.; Wehrspohn, R. B.; Lee, J.; Gosele, U. *Electrochimica Acta* **2004**, *49*, 2645-2652.

(9) Xu, T. T.; Piner, R. D.; Ruoff, R. S. *Langmuir* **2003**, *19*, 1443-1445.

(10) Li, F.; Zhang, L.; Metzger, R. M. *Chem. Mater.* **1998**, *10*, 2470-2480.

(11) Hulteen, J. C.; Martin, C. R. *Journal of Materials Chemistry*, **1997**, *7*, 1075 - 1087.

(12) Pan, H.; Liu, B.; Yi, J.; Poh, C.; Lim, S.; Ding, J.; Feng, Y.; Huan, C. H. A.; Lin, J. *J. Phys. Chem. B* **2005**, *109*, 3094-3098.

(13) Chiriac, H.; Moga, A. E.; Urse, M.; Ovari, T.-A. *Sensors and Actuators A* **2003**, *106*, 348-351.

(14) Nielsch, K.; Muller, F.; Li, A.-P.; Gosele, U. *Adv. Mater.* **2000**, *12*, 582-586.

(15) Keller, F.; Hunter, M. S.; Robinson, D. L. *J. Electrochem. Soc.* **1953**, *100*, 411-419.

(16) Saedi, A.; Ghorbani, M. *Materials Chemistry and Physics* **2005**, *91*, 417-423.

(17) McConnell, W. P.; Novak, J. P.; Brousseau, L. C.; Fuierer, R. R.; C., T. R.; Feldheim, D. L. *J. Phys. Chem. B* **2000**, *104*, 8925-8930.

(18) Hu, J. T.; Odom, T. W.; Lieber, C. M. *Acc. Chem. Res.* **1999**, *32*, 435-445.

(19) Jana, N. R.; Gearheart, L.; Murphy, C. J. *Chem. Commu.* **2001**, *6*, 617-618.

(20) Zhou, Y.; Yu, S. H.; Wang, C. Y.; Li, X. G.; Zhu, Y. R.; Chen, Z. Y. *Adv. Mater.* **1999**, *11*, 850-852.

(21) Zhou, Y.; Yu, S. H.; Cui, X. P.; Wang, C. Y.; Chen, Z. Y. *Chem. Mater.* **1999**, *11*, 545-546.

(22) Lee, W.; Yoo, H.-I.; Lee, J.-K. *Chem. Commun.* **2001**, *24*.

(23) Zong, R.; Zhou, J.; Li, Q.; Li, L.; Wang, W.; Chen, Z. *Chem. Phys. Lett.* **2004**, *398*, 224-227.

(24) Chaney, S. B.; Shanmukh, S.; Dluhy, R. A.; Zhao, Y.-P. *Appl. Phys. Lett.* **2005**, *87*, 031908.

(25) Pan, Z. W.; Dai, Z. R.; Wang, Z. L. *Science* **2001**, *291*, 1947-1949.

(26) Duan, X.; Huang, Y.; Cui, Y.; Wang, J.; Lieber, C. M. *Nature* **2001**, *409*, 66-69.

(27) Huang, M. H.; Mao, S.; Feick, H.; Yan, H.; Wu, Y.; Kind, H.; Weber, E.; Russo, R.; Yang, P. *Science* **2001**, *292*, 1897-1899.

(28) Xia, Y.; Yang, P.; Sun, Y.; Wu, Y.; Mayers, B.; Gates, B.; Yin, Y.; Kim, F.; Yan, H. *Adv. Mater.* **2003**, *15*, 353-389.

(29) Rao, C. N. R.; Gundiah, G.; Deepak, F. L.; Govindaraj, A.; Cheetham, A. K. *J. Mater. Chem.* **2004**, *14*, 440-450.

(30) Zou, J.; Pu, L.; Bao, X.; Feng, D. *Appl. Phys. Lett.* **2002**, *80*, 1079-1081.

(31) Fang, X.-S.; Ye, C.-H.; Zhang, L.-D.; Xie, T. *Adv. Mater.* **2005**, *17*, 1661-1665.

(32) Valcarcel, V.; Souto, A.; Guitian, F. *Adv. Mater.* **1998**, *10*, 138-140.

(33) Peng, X. S.; Zhang, L. D.; Meng, G. W.; Wang, X. F.; Wang, Y. W.; Wang, C. Z.; Wu, G. S. *J. Phys. Chem. B* **2002**, *106*, 11163-11167.

(34) Zhou, J.; Deng, S. Z.; Chen, J.; She, J. C.; Xu, N. S. *Chem. Phys. Lett.* **2002**, *365*, 505-508.

(35) Fang, X.-S.; Ye, C.-H.; Xu, X.-X.; Xie, T.; Wu, Y.-C.; Zhang, L.-D. *J. Phys.: Condens. Matter* **2004**, *16*, 4157-4163.

(36) Zhao, Q.; Xu, X.; Zhang, H.; Chen, Y.; Xu, J.; Yu, D. *Appl. Phys. A* **2004**, *79*, 1721-1724.

(37) Proost, J.; Van Boxel, S. *J. Mater. Chem.* **2004**, *14*, 3058-3062.

(38) Fang, X. S.; Ye, C. H.; Peng, X. S.; Wang, Y. H.; Wu, Y. C.; Zhang, L. D. *J. Mater. Chem.* **2003**, *13*, 3040-3043.

(39) Gundiah, G.; Deepak, F. L.; Govindaraj, A.; Rao, C. N. R. *Top. Catal.* **2003**, *24*, 137-146.

(40) Pang, Y.-T.; Meng, G.-W.; Zhang, L.-D.; Shan, W.-J.; Zhang, C.; Gao, X.-Y.; Zhao, A.-W.; Mao, Y.-Q. *J. Solid State Electrochem.* **2003**, *7*, 344-347.

(41) Hwang, J.; Min, B.; Lee, J. S.; Keem, K.; Cho, K.; Sung, M.; Lee, M.; Kim, S. *Adv. Mater.* **2004**, *16*, 422-425.

(42) Xiao, Z. L.; Han, C. Y.; Welp, U.; Wang, H. H.; Kwok, W. K.; Willing, G. A.; Hiller, J. M.; Cook, R. E.; Miller, D. J.; Crabtree, G. W. *Nano Lett.* **2002**, *2*, 1293-1297.

(43) Yuan, Z.; Huang, H.; Fa, S. *Adv. Mater.* **2002**, *14*, 303-306.

(44) Tian, Y. T.; Meng, G. W.; Gao, T.; Sun, S. H.; Xie, T.; Peng, X. S.; Ye, C. H.; Zhang, L. D. *Nanotechnology* **2004**, *15*, 189-191.

(45) Pu, L.; Bao, X.; Zou, J.; Feng, D. *Angew. Chem. Int. Ed.* **2001**, *40*, 1490-1493.

(46) Wang, X.; Han, G.-R. *Microelectronic Engineering* **2003**, *66*, 166-170.

(47) Yu, J.-Y.; Chung, S.-W.; Heath, J. R. *J. Phys. Chem. B* **2000**, *104*, 11864-11870.

Chapter III: *In-situ* Fabrication of Dispersed, Crystalline Platinum Nanoparticles Embedded in Carbon Nanofibers Using Porous Anodic Aluminum Oxide Membrane Templates for Polymer Electrolyte Membrane Fuel Cell Applications

3.1 Introduction

To date, reported composites containing highly-dispersed platinum particles in carbon nanomaterials are based on rather complicated synthetic procedures,[1-4] i.e., fabricating mesoporous carbon nanotubes or foams, introducing a platinum salt (usually H_2PtCl_6) into porous carbon, then reducing the platinum salt to platinum metal with hydrogen gas[1,2] or by electrodeposition.[3,4] These procedures require considerable platinum salt and involve a multi-step fabrication process that frequently results in aggregated platinum particles, which in turn lowers the available surface area and decreases the mass activity of catalyst.

Arrays of carbon nanofibers (CNFs) in a controlled geometry enable the realization of potential applications, such as field-emission devices[5] and chemical sensors.[6] Among various nanofabrication techniques, the use of porous anodic aluminum oxide (p-AAO) membrane templates is one of the easiest and widely applied ways to obtain highly ordered nanomaterials.[7-9] The CNFs fabricated via template synthesis are uniform in diameter, nearly hexagonally close-packed, perpendicular to the template mold surface,[10,11] and in some cases exhibit improved physical properties, e. g. field emission.[12]

Furthermore, due to their inherent high surface area, CNFs containing highly dispersed metal nanoparticles are important catalysts.[1,2] For example, the electrocatalytic activity of platinum particles dispersed in carbon nanotubes prepared in mesopores silica templates[1] or AAO membrane templates[2] have been studied. The combination of high surface area and a good dispersion of catalyst is of particular interest in proton exchange membrane fuel cells and direct methanol fuel cells.[3]

The goal of this chapter is to describe the preparation of CNFs containing monodisperse platinum nanoparticles by *in-situ* polymerization of acrylonitrile in a p-AAO membrane template, followed by pyrolysis of polyacrylonitrile (PAN) and concomitant reduction of platinum salt to platinum metal. As shown in Table 3-1, several kinds of platinum-carbon nanocomposites were fabricated using different platinum precursor (platinum acetylacetonate or chloroplatinic acid) with homemade or Whatman membranes. The products were characterized with scanning electron microscopy (SEM), atomic force microscopy (AFM), transmission electron microscopy (TEM), high resolution transmission electron microscopy (HRTEM), and X-ray photoelectron spectroscopy (XPS). For Pt-CNFs and Pt-CNFs' (Table 3-1), single crystalline Pt nanoparticles in the size range of 1 to 4 nm are highly dispersed in the carbon matrix. The electrocatalytic activity for the reduction of oxygen was determined with rotating disc electrode (RDE) voltammetry. The fuel cell performance of the prepared samples was tested in a TELEDYNE MEDUSA RD Fuel Cell Test Station.

Table 3-1. Abbreviations of platinum carbon nanocomposites fabricated using different starting materials and templates.

Sample	Mass ratios of starting materials			Template
	Acrylonitrile	$Pt(acac)_2$	$H_2PtCl_6 \cdot 6H_2O$	
Pt-CNFs	100	1		Homemade p-AAO
Pt-CNFs'	100	1		Whatman p-AAO
Pt-CNFs''	100		6	Whatman p-AAO
CNFs	100			Whatman p-AAO
Pt-C	100	1		None

3.2 Materials and Instrumentation

Materials: Platinum (II) acetylacetonate ($Pt(II)(CH_3COCHCOCH_3)_2$, Pt, 49.6% Alfa Aesar), chloroplatinic acid hexahydrate ($H_2PtCl_6 \cdot 6H_2O$, Sigma Aldrich), oxalic acid (99.5%, Alfa Aesar), copper chloride (99+%, Alfa Aesar), phosphoric acid (86%, Fisher Scientific), hydrochloric acid (37.3%, Fisher Scientific), sulfuric acid (99.999%, Aldrich),sodium hydroxide (98.7%, Mallinckrodt), ethanol (Fisher Scientific), 2,2'-azo-*bis*-isobutyrylnitrile (POLYSCIENCES, INC), 5 wt% perfluorosulfonic acid-PTFE copolymer(5 wt% Nafion alcohol solution, Alfa Aesar), 2-propanol (99.9%, Fisher Scientific), E-TEK (20 wt% HP Pt on Vulcan XC-72, DE NORA ELETTRODI), Nafion 117 film (DuPont), carbon cloth (E-LAT JDL microporous layer, E-TEK), Teflon film (LGS Technologies), hydrogen peroxide (H_2O_2, 31.8%, Fisher Scientific) and Whatman 0.2 μm porous anodic aluminum oxide membrane discs (Fisher Scientific) were used as received, unless stated otherwise. Acrylonitrile monomer (99+%, Aldrich) was freshly distilled prior to use. Homemade p-AAO membranes were fabricated following two-step anodization[13,14] using 0.3 M oxalic acid aqueous solution under a constant voltage of 40 V at 5˚C as stated in section 2.3.1.1. Afterwards, to get a larger pore size, the pores were widened by chemical etching in 5 wt% aqueous phosphorous acid at 30˚C.

Instrumentation: The surface morphology of homemade p-AAO membranes was determined by AFM (Nanoscope IIIa). The SEM images of AAO membrane and Pt-CNFs were obtained using a JEM6300 microscope. The Pt-CNFs, Pt-CNFs', CNFs, and Pt-C were also examined by TEM (JEM-100CX-II) operated at 100 kV and HRTEM (JEM-

2010F-FasTEM) at 200 kV. The XPS measurements of Pt-CNFs were performed on a PHI-5400 spectrometer with a Mg Kα source. The C 1s peak at 284.6 eV was used as a reference.[15,16] X-ray diffraction (XRD) tests of Pt-C, Pt-CNFs', and Pt-CNFs" (Table 3-1) were conducted on a Rigaku Multiflex X-ray diffractometer with a Cu Kα source and a scan speed of 0.5 ˚/minute. Tests of electrocatalytic activity for oxygen reduction reaction were carried out on a BAS RDE-1 system. Fuel cell polarization measurements were conducted on a TELEDYNE MEDUSA RD Fuel Cell Test Station.

3.3 Platinum-Nanoparticle-Embedded Carbon Nanofibers Using Platinum Acetylacetonate as Platinum Precursor

3.3.1 Experimental

3.3.1.1 Synthesis of Pt-CNFs Using Homemade p-AAO Membranes

Pt-CNFs (Table 3-1) were fabricated in the homemade p-AAO membranes. Figure 3-1 shows a schematic diagram outlining the fabrication procedure. P-AAO templates were immersed in distilled acrylonitrile monomer (CH_3CH_2CN) containing 0.1 wt% 2,2'-azo-*bis*-isobutyrylnitrile (AIBN) and 1 wt% platinum (II) acetylacetonate [$Pt(acac)_2$]. Polymerization at 50˚C and cyclization at 220˚C, respectively, were carried out within the p-AAO templates pores in air for ten hours.[17] After removing the residual aluminum substrate in a mixture of 0.1 M copper chloride and hydrochloric acid,[18] the PAN nanofibers in p-AAO membrane were further pyrolyzed under high vacuum at 700˚C[6] for 6 hours. Afterwards, the p-AAO template was dissolved in 6 M sodium hydroxide aqueous solution. The Pt-CNFs were cleaned with distilled water, rinsed with ethanol, and

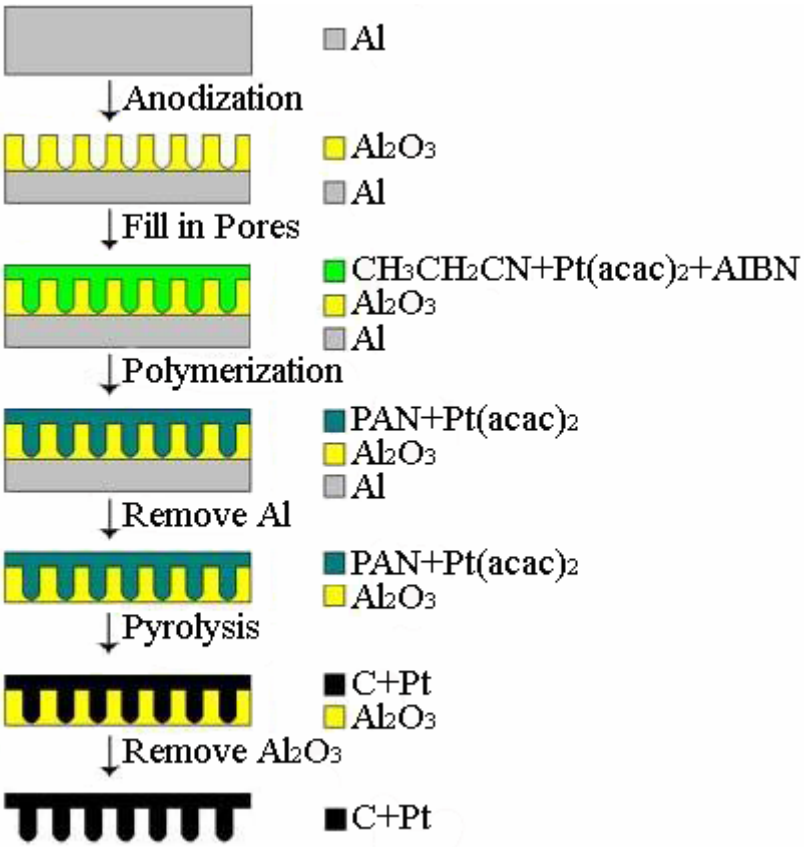

Figure 3-1. Schematic diagram of the fabrication of Pt-CNFs using a homemade p-AAO membrane template.

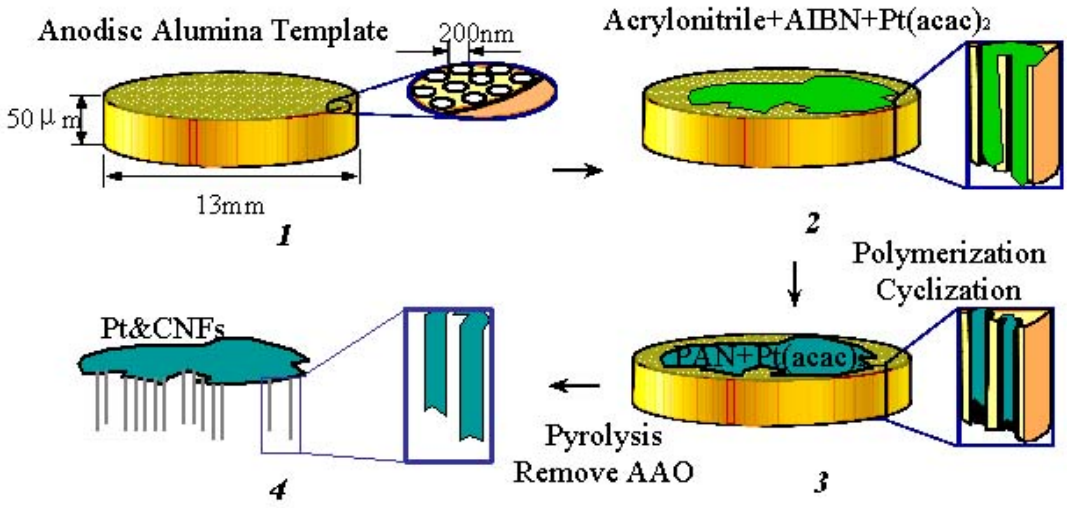

Figure 3-2. Schematic diagram of the fabrication of Pt-CNFs' using a commercial Whatman p-AAO membrane template.

carefully dried in liquid CO_2[19] to reduce aggregation of nanofibers induced by solvent surface tension on drying.

3.3.1.2 Synthesis of Pt-CNFs' Using Commercial Whatman p-AAO Membranes

Pt-CNFs' (Table 3-1) were fabricated following a similar procedure as the fabrication of Pt-CNFs except for replacing homemade p-AAO membranes with Whatman p-AAO membranes. Figure 3-2 shows a schematic diagram of the fabrication procedure. Since there is no aluminum substrate for Whatman p-AAO membrane, there is no Al removal step. The other treatments are the same.

3.3.1.3 Synthesis of Pt-C and CNFs

To understand the formation mechanism for platinum-embedded carbon nanofibers, CNFs and Pt-C were fabricated and the results were contrasted with the Pt-CNFs and Pt-CNFs'.

Pure CNFs were fabricated from the pyrolysis at 700 ˚C of polymer from the polymerization of monomer acrylonitrile with 0.1 wt% AIBN in the Whatman p-AAO template. With no platinum precursor added at the beginning, there was no Pt in the final CNFs.

Pt-C powder was the reaction product from the pyrolysis at 700 ˚C of bulk polymer composites, which were prepared from the polymerization of acrylonitrile with 0.1 wt% AIBN and 1 wt% $Pt(acac)_2$ without an p-AAO template.

3.3.1.4 Preparation of Electrodes and Electrocatalytic Activity Measurements

The electrodes were prepared according to reported methods.[2] 1.0 mg of Pt-CNFs was ultrasonically dispersed in 1.0 ml 5 wt% Nafion and 9.0 ml NANO pure H_2O. 10 μL of the mixture was dropped onto the glassy carbon core (3 mm in diameter). The solvent was slowly evaporated at room temperature over night resulting in a Pt-CNFs-Nafion composite electrode interface (Pt-CNFs electrode).

The electrode was mounted in the BAS RDE-1 system with a Platinum counter electrode and a Ag/AgCl (in 3M NaCl) reference electrode. The electrolyte, 1.0M H_2SO_4 solution, was purged with either O_2 or Ar before measuring electrocatalytic current at room temperature. The catalytic currents over a range of rotation rates (0 to 1000 rpm) were recorded at room temperature with a scan rate of 100 mV/s.

Electrodes were prepared from Pt-CNFs', CNFs, Pt-C, and E-TEK catalyst (with 20 wt% Pt loading on Vulcan carbon) using the same procedure. Electrocatalytic currents were measured under identical conditions with suitable scan ranges. The results were contrasted with the Pt-CNFs electrode. Including Pt-CNFs coated electrode, the five different electrodes are abbreviated as a) Pt-CNFs, b) Pt-CNFs', c) Pt-C, d) CNFs, and e) E-TEK.

3.3.2 Results and Discussion

3.3.2.1 Characterization of Homemade p-AAO Membranes

Hexagonally packed Uniform porous AAO membranes were prepared by the two-step anodization process described in Chapter 2.3.1.1. Figure 3-3A, the top view of the

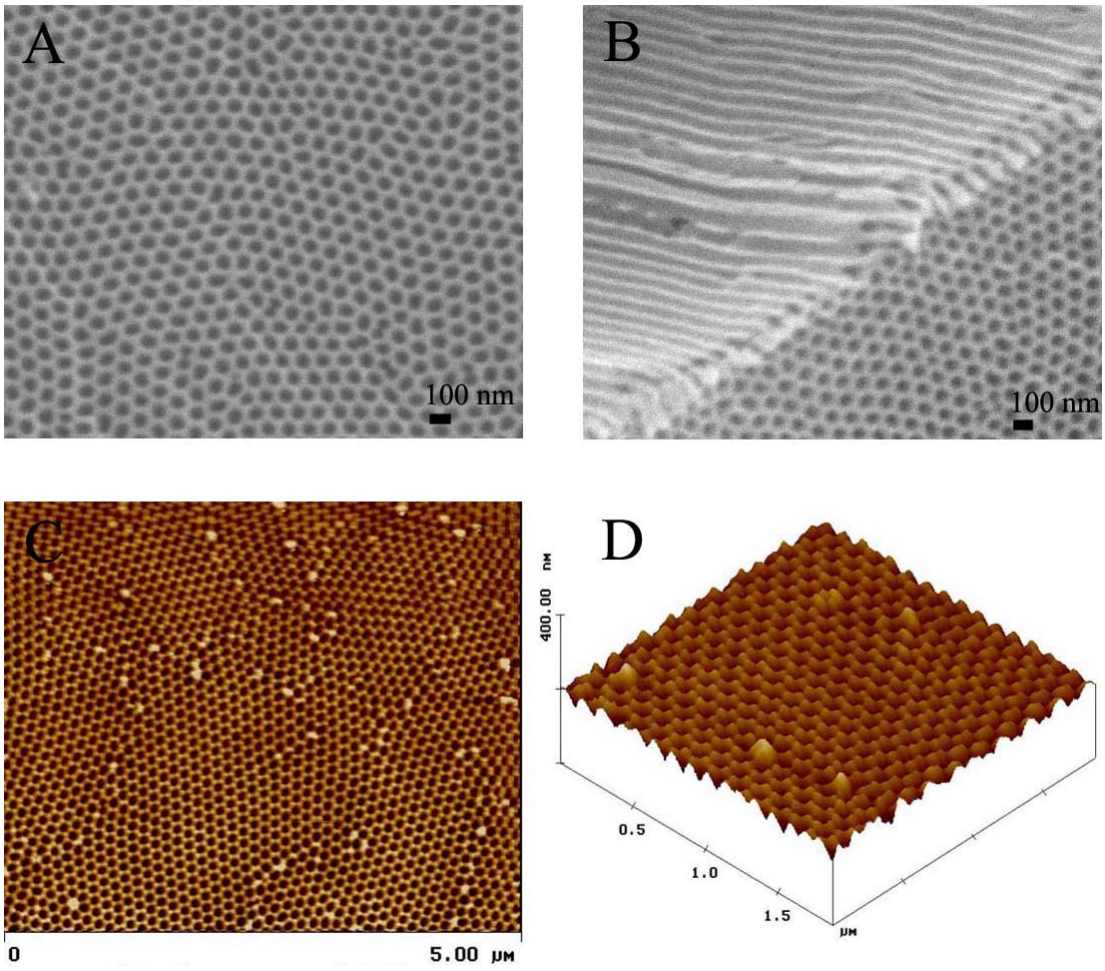

Figure 3-3. SEM and AFM micrographs of a homemade p-AAO membrane.
SEM micrographs of (A) top and (B) cross-sectional views of a homemade p-AAO membrane. Two-dimensional (C) and three-dimensional (D) AFM height images of a homemade p-AAO membranes.

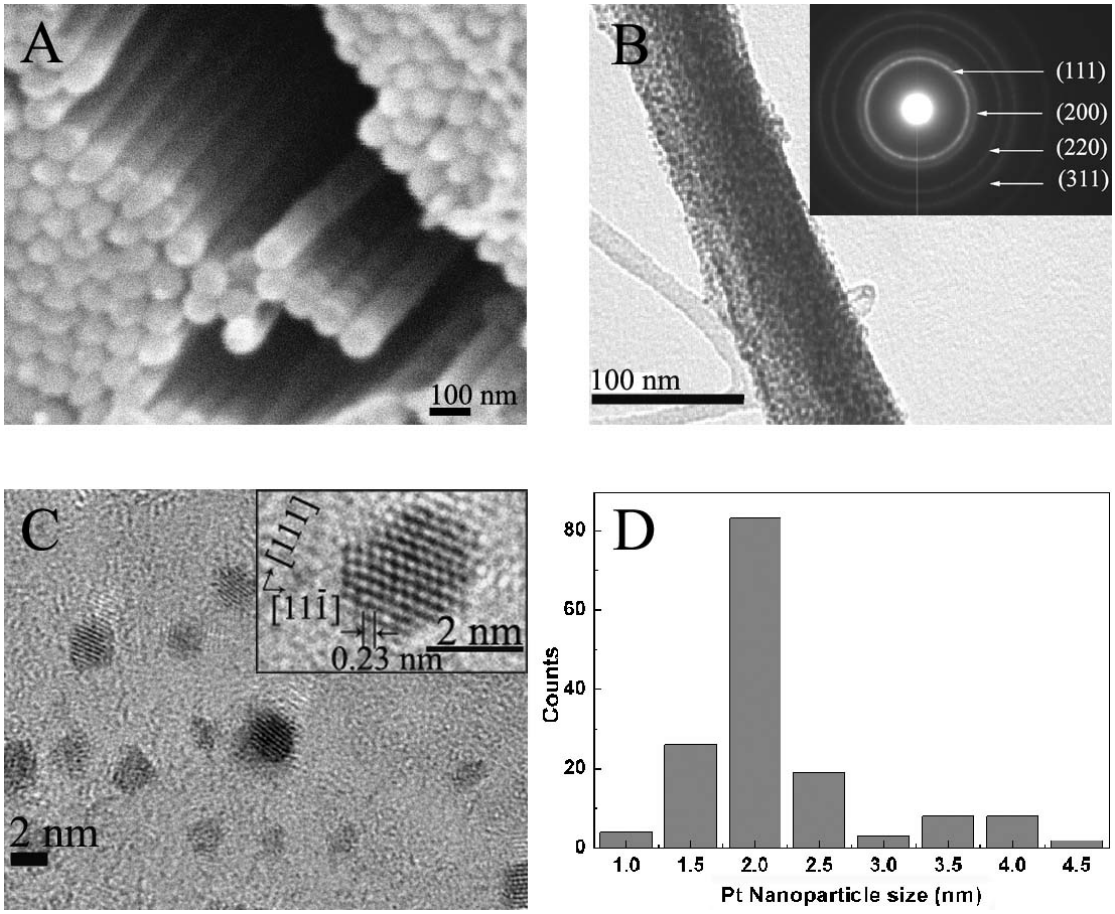

Figure 3-4. EM characterization of Pt-CNFs.

(A) SEM image of the Pt-CNFs; (B) TEM image of a selected area of Pt-CNFs; the upper-right inset is a selected area electron diffraction pattern showing the diffraction rings coming from Pt nanoparticles; (C) HRTEM image of the Pt-CNFs; the upper-right inset is a larger magnification image showing the (1 1 1)and (1 1 -1) plane orientations of cubic, single-crystalline Pt nanoparticle;(D) the size distribution of the embedded Pt nanoparticles in the carbon matrix.

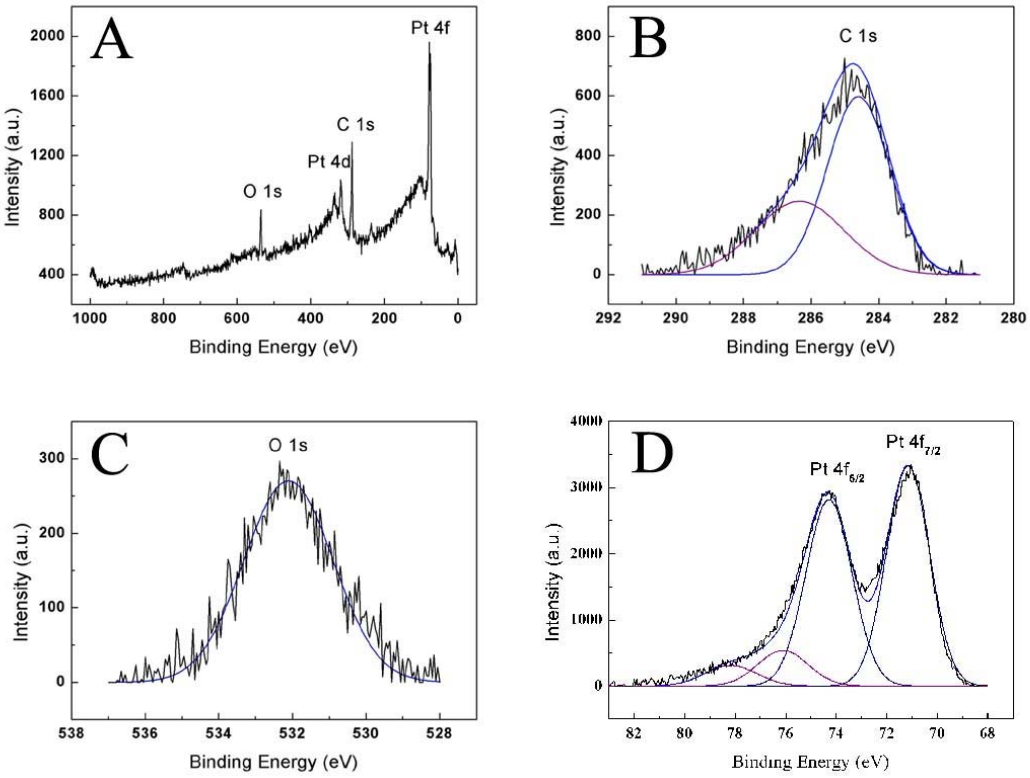

Figure 3-5. XPS characterization of Pt-CNFs.
(A) XPS survey spectrum of the Pt-CNFs; (B) C 1s (C) O 1s (D) Pt 4f XPS spectra of the specimen.

AAO membranes, indicates that the pore openings on the surface are close-packed with ~ 80 nm diameters. Figure 3-3B is a cross-sectional view of the AAO membrane showing that all of the nanopore channels are reasonably straight, parallel and traverse the entire thickness of the membrane. The two-dimensional (Figure 3-3C) and three-dimensional (Figure 3-3D) AFM height images show that the surface morphology of AAO membranes consists of periodically arranged pores (interpore distance of 119 nm) with randomly distributed protuberances as high as 50 nm.

3.3.2.2 Characterization of Pt-CNFs

The morphology and composition of Pt-CNFs was investigated by SEM, TEM, HRTEM and XPS. Figure 3-4A is a SEM image of the Pt-CNFs, which illustrates that uniform nanofibers are straight and parallel to each other, and hexagonally close-packed. The TEM image of the specimen is shown in Figure 3-4B. The diameters of the nanofibers are nearly 80 nm, which matches the pore diameter of the AAO template. The lengths of the nanofibers are determined by the thickness of the AAO template. The upper-right inset in Figure 3-4B shows a selected area electron diffraction (SAED) pattern. The rings correspond to the diffraction from the (1 1 1), (2 0 0), (2 2 0) and (3 1 1) planes of crystalline Pt particles. Figure 3-4C, the HRTEM image of Pt-CNFs, indicates that the Pt nanoparticles embedded in the amorphous carbon matrix are perfectly crystalline and highly dispersed. The upper-right inset in Figure 3-4C is a higher magnification image showing a single Pt nanocrystal with its (1 1 1) and (1 1 -1) plane orientations at an angle of 70.5˚. The inter-plane distance (0.23 nm) corresponds to the distance between two

adjacent (1 1 1) planes. The sizes of the Pt nanoparticles in CNFs matrix are narrowly distributed as shown in Fig 3-4D. Based on measurements of more than 150 nanoparticles, the mean particle size is 2.2±0.7 nm; over 70% are between 1.5 and 2.5 nm.

The oxidation states of the composition elements in Pt-CNFs were determined by XPS. Figure 3-5A shows the survey scan for the specimen, which consists of four peaks, C 1s, O 1s, Pt 3d, and Pt 4f. Unlike reported data,[16] the N peak is barely visible in the survey XPS spectrum; this may be due to the pyrolysis in high vacuum in contrast to the reported studies with pyrolysis under an argon atmosphere. Figures 3-5B to 3-5D show XPS multiplex scans for the C 1s, O 1s and Pt 4f regions respectively. The C 1s signal could be deconvoluted into carbon peaks in two kinds of chemical environments, the graphitic carbon at 284.6 eV and C-O or C=O species at 286.3 eV.[15,16] The oxygen peak at 532.1 eV may also correspond to O=C and O-C species.[16] The Pt 4f signals could be decomposed into two pairs of doublets. The intense peaks centered at 71.1 eV and 74.3 eV, respectively, belong to Pt $4f_{5/2}$ and Pt $4f_{7/2}$ excitations of metallic platinum, while the peaks with binding energies of 76.1 eV and 78.2 eV may be assigned to a small amount of Pt(IV) species on the surface.[15] We conclude therefore, that around 90% of platinum (II) acetylacetonate was reduced to elemental platinum during the pyrolysis of PAN nanofibers.

3.3.2.3 Characterization of Pt-CNFs'

Pt-CNFs' synthesized using commercial Whatman p-AAO membrane was also studied using EM. Figure 3-6A is the SEM image of the aligned nanofibers after

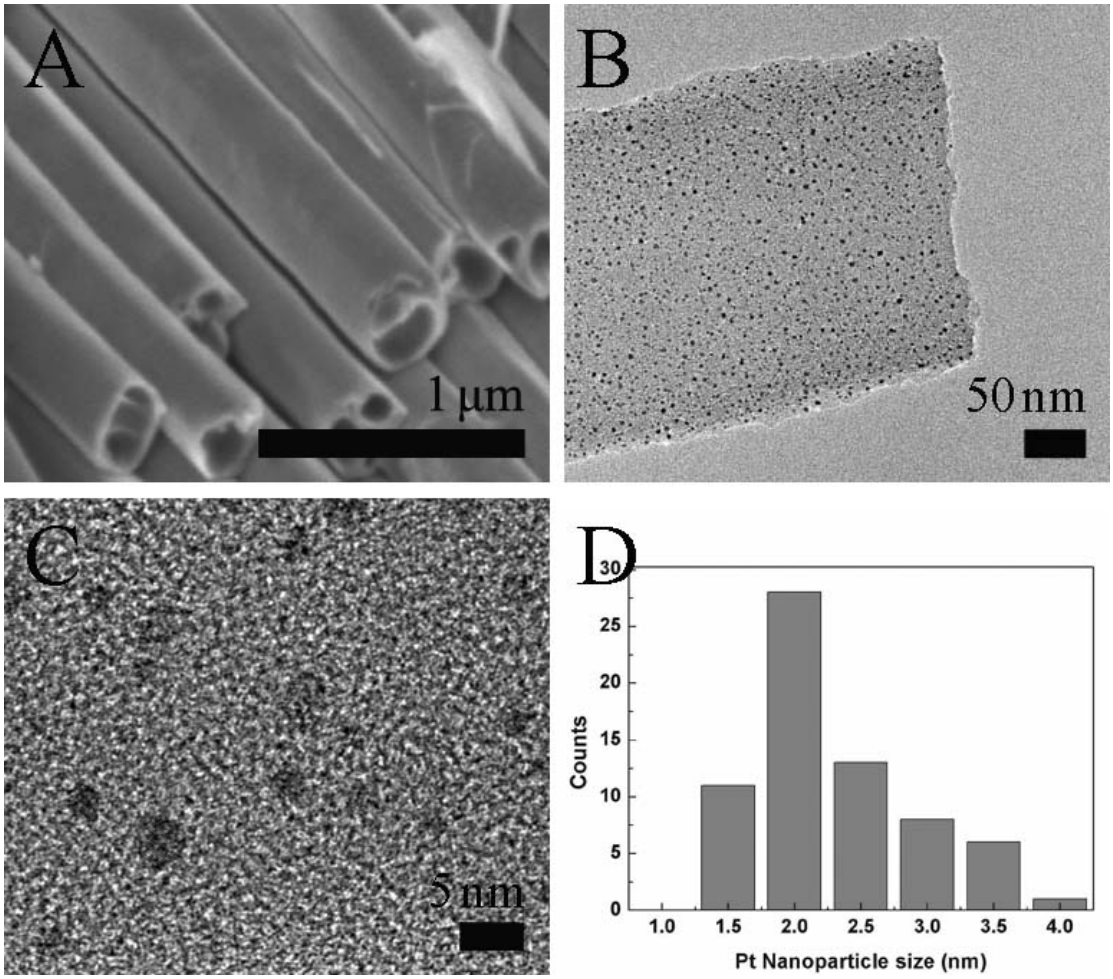

Figure 3-6. EM characterization of Pt-CNFs'.

(A) SEM image of Pt-CNFs'; (B), (C) HRTEM image of the Pt-CNFs' at different magnifications; (D) the size distribution of the embedded Pt nanoparticles in CNFs.

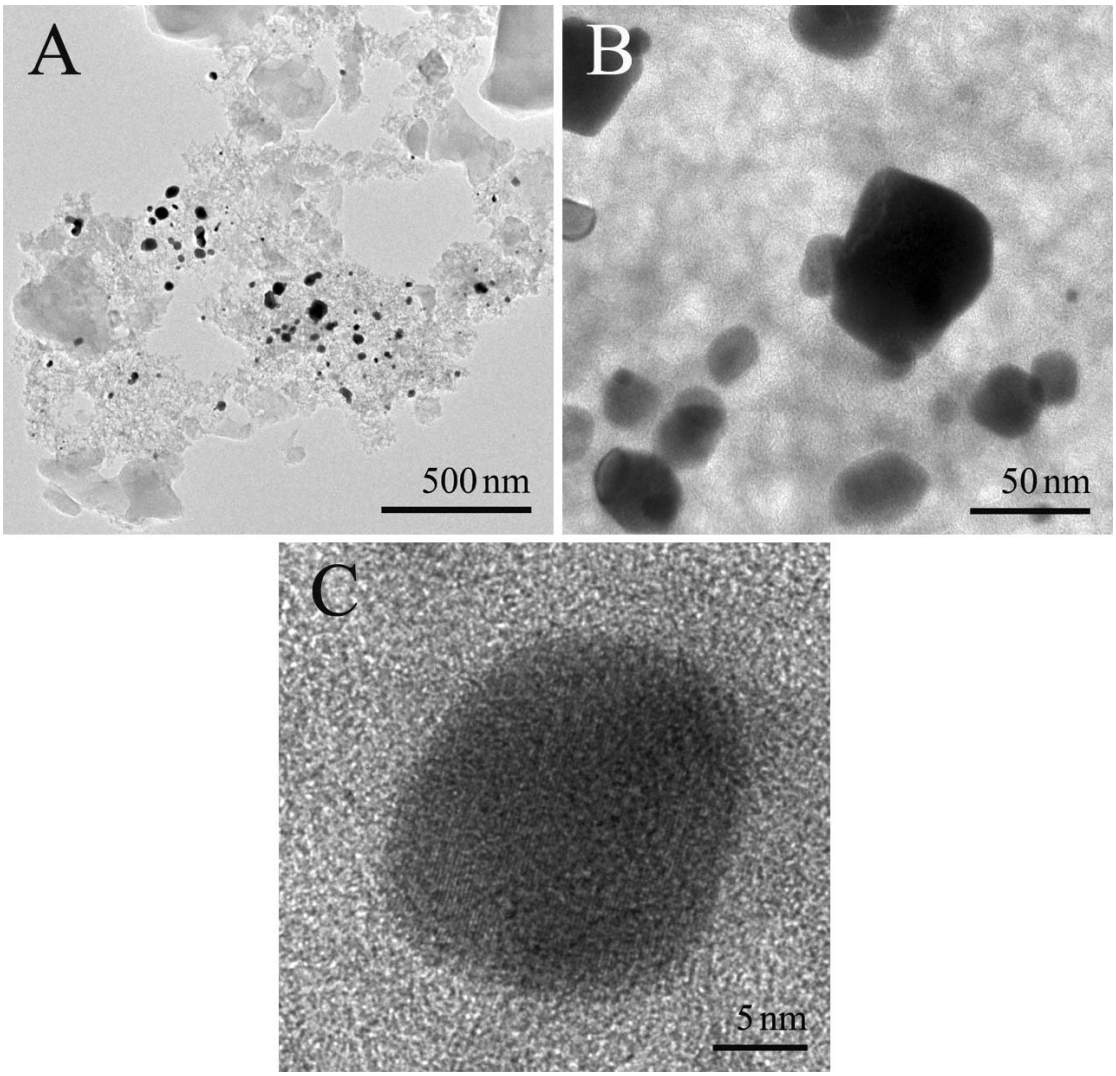

Figure 3-7. EM characterization of Pt-C.
HRTEM images at different resolutions of the Pt-C composite fabricated without using p-AAO templates.

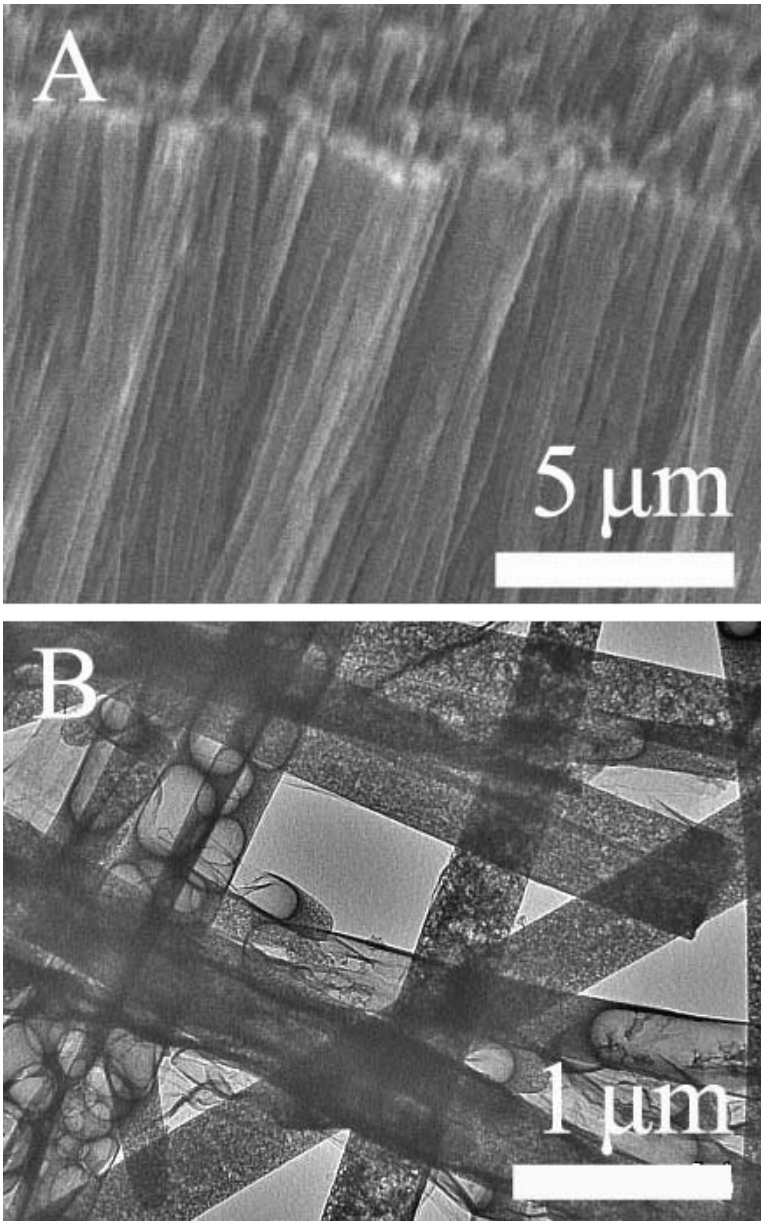

Figure 3-8. EM characterization of CNFs.
(A) SEM and (B) TEM images of the CNFs prepared using Whatman p-AAO templates.

removing the templates. The fibers are straight and hollow, with outer diameter between 300nm to 400nm. This is because the channels of Whatman p-AAO are not uniform in diameter. The thickness of the walls of nanofibers is around 40nm. Figures 3-6B and 3-6C show HRTEM images at different resolutions. Platinum nanoparticles are highly dispersed and uniformly distributed around the carbon fibers. The size distribution of platinum nanoparticles in Pt-CNFs', as shown in Figure 3-6D, is similar to that of Pt-CNFs. The mean diameter is about 2.3±0.6 nm with over 75% of particles in the range of 1.5-2.5 nm.

3.3.2.4 Characterization of Pt-C Composite

Figure 3-7 shows the HRTEM images of Pt-C from pyrolysis of PAN and coincident decomposition of $Pt(acac)_2$ with no template involved during the whole process. Completely different from the results of Pt-CNFs and Pt-CNFs', platinum nanoparticles in Pt-C are much larger and much broadly distributed (15 nm to 70 nm in diameter), which means that serious aggregation and coalescence of platinum nanoparticles happened at high temperature. In addition, platinum particles are not uniform distributed. These results suggest that p-AAO membranes played an important role for forming smaller sized, uniform, and highly dispersed platinum nanoparticles.

3.3.2.5 Characterization of CNFs

SEM and TEM images of the CNFs prepared using Whatman p-AAO template were shown in Figure 3-8. They are well aligned after removing the template (Figure 3-

8A) and the sizes of CNFs are determined by the channels of p-AAO membrane. There is no morphology difference between CNFs and Pt-CNFs' except for no embedded platinum nanoparticles in CNFs. This indicates that the platinum salt does not affect the chemistry of polymerization and pyrolysis at all.

3.3.2.6 E-TEK Catalyst

Structures of ETEK catalyst with 20 wt% platinum loading are reported elsewhere.[20] High power platinum nanoparticles are supported on Vulcan XC-72 carbon particles around 30nm. The platinum nanoparticles are from 1.1 to 4.7 nm, with a mean diameter of 2.2±0.8 nm.[20]

3.3.3 Pt-CNFs Formation Mechanism

Given all the structures above, the formation procedure of the platinum nanoparticles is proposed to occur as following: as the polymerization proceeds, the medium becomes more viscous and the solvent quality of the polymer-rich solution (relative to the monomer) decreases. As a result, the $Pt(acac)_2$ molecules begin to aggregate/precipitate from solution forming platinum-rich domains within the solidifying polymer matrix. The interaction between polymer matrix and p-AAO membrane channels will greatly restrict the movement of polymer chains, which will further inhibit the diffusion ability of platinum-rich domains. In addition, the channel walls will block the diffusion possibility in one dimension. Therefore, these domains of platinum salt decompose with minimal diffusion and are reduced to elemental platinum during the

pyrolysis of PAN nanofibers. The produced platinum nanoparticles are isolated and immobilized in the carbonaceous matrix. Hence, they are unable to diffuse and coalesce during pyrolysis.[21] Without p-AAO membranes, although the diffusion of platinum salt domain is still restricted, the mobility of polymer chains is much higher. As a result, platinum nanoparticles fabricated without p-AAO membrane involved are much larger than those prepared using p-AAO templates. Since the channels of both homemade and Whatman channels are much larger compared to the platinum-rich domains, they do not affect to the size of domains. Therefore, the final size of platinum nanoparticles does not depend much on the diameter of channels.

3.3.4 Electrocatalytic Activity Test

The electrocatalytic activity of the Pt-CNFs for O_2 reduction was studied by RDE voltammetry. Figure 3-9A shows the oxygen reduction hydrodynamic polarization scans in oxygen-purged 1 M sulfuric acid at different rotation rates; the background scan is from an argon-purged solution. The limiting electrocatalytic current plateau decreases with decreasing the rotation rate. Additionally, the curves shifted to a lower voltage after each scan, suggesting that the electrode loses parts of its activity during each measurement. The electrocatalytic current of the five electrodes with the background subtracted is shown in Figure 3-9B. It is obvious that the oxygen reduction happens at much higher voltages (0.94 V and 0.96V relative to the reference electrode respectively) for the Pt-CNFs and Pt-CNFs' electrodes than for each of the controls, the Pt-C (0.22V) or the CNFs (0.28V), or even the ETEK (0.66V) electrode. Hence, the electrocatalytic

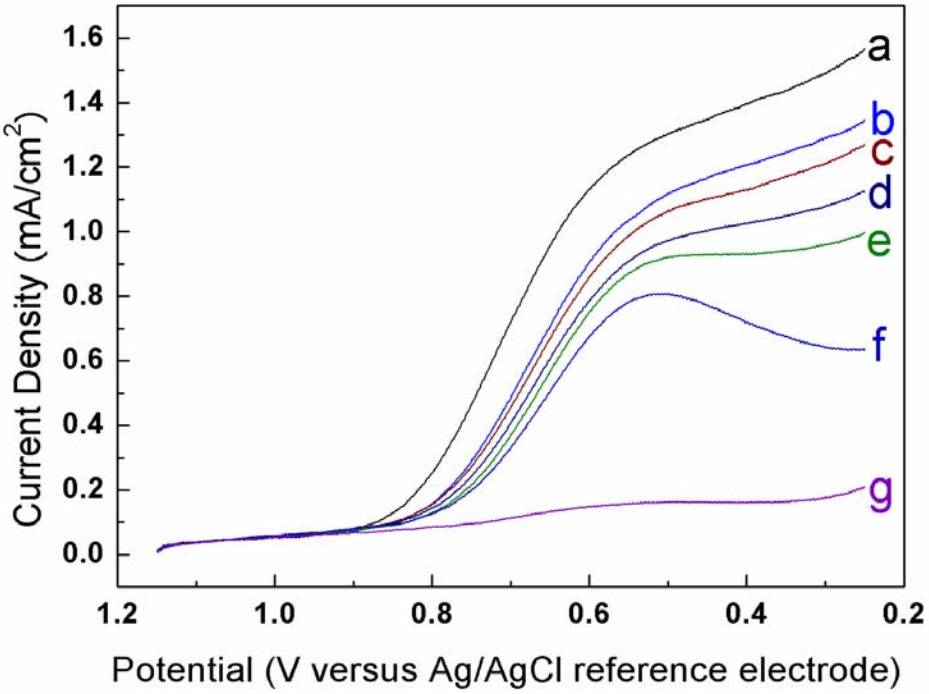

Figure 3-9. Oxygen reduction hydrodynamic polarization scans of Pt-CNFs electrodes at different rotation rates.

Oxygen reduction hydrodynamic polarization scans of Pt-CNFs electrodes in oxygen-purged 1M sulfuric acid at different rotation rates (a, 1000 rpm; b, 800 rpm; c, 600 rpm; d, 400 rpm; e, 200 rpm; f, 0 rpm) and the background scan g in argon-purged electrolyte at 1000 rpm.

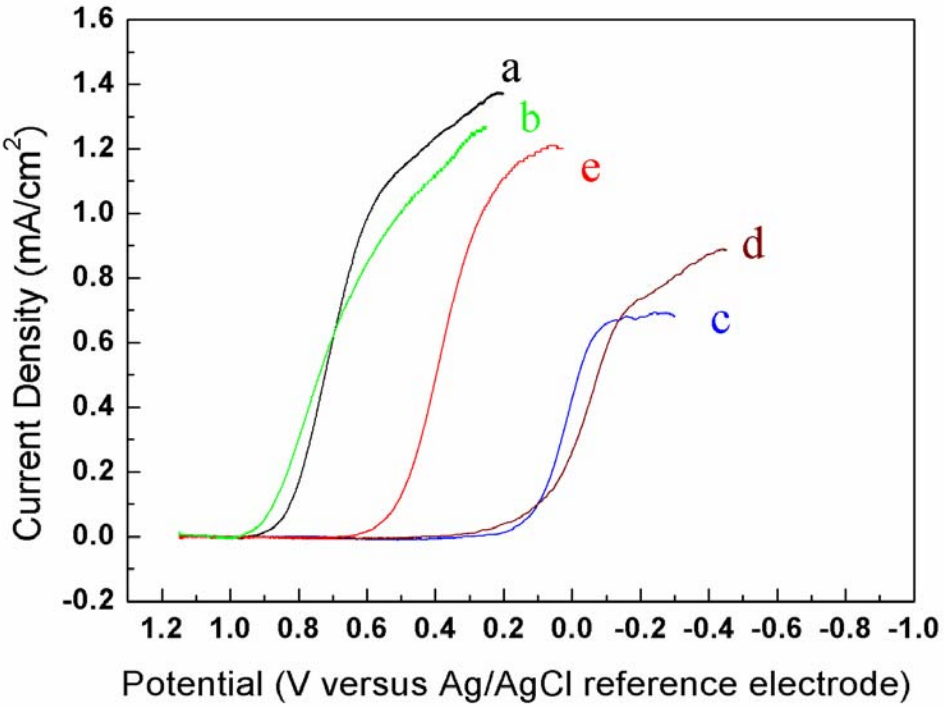

Figure 3-10. Oxygen reduction hydrodynamic polarization scans of different electrodes at 1000 rpm.

Oxygen reduction hydrodynamic polarization scans of different electrodes (a, Pt-CNFs electrode; b, Pt-CNFs' electrode; c, Pt-C electrode; d， CNFs electrode; e, E-TEK electrode) in oxygen-purged 1M sulfuric acid at rotation rate of 1000 rpm with background subtracted.

activity comes from the Pt nanoparticles dispersed in the high surface-area CNFs. Since the preparation of Pt-CNFs and Pt-CNFs' is similar, moreover, the size distribution of platinum nanoparticles in Pt-CNFs and Pt-CNFs' is almost identical, the catalytic activities of both electrodes are almost the same. Given that the Ag/AgCl reference electrode (in 3M NaCl) is 206 mV relative to the normal hydrogen electrode, the Pt-CNFs electrode shows a better catalytic activity than the arrays of carbon nanotubes supporting high dispersions of Pt nanoparticles achieved by more complicated procedures.[1] In fact, the scan of the Pt-CNFs electrode is comparable to data from a pure Pt thin-film electrode.[22]

3.4 Platinum-Nanoparticle-Embedded Carbon Nanofibers Using Chloroplatinic Acid as a Platinum Precursor

3.4.1 Introduction

To increase the platinum loading in CNFs, a larger weight ratio of platinum precursor is required in the starting monomer solution. However, the solubility of $Pt(acac)_2$ in acrylonitrile is limited, and 1 wt% is approximately the maximum concentration, while H_2PtCl_6 shows a much better solubility in acrylonitrile monomer.

From the previous study, we found that the size of platinum nanoparticles did not depend on the pore size of the p-AAO membrane template. In addition, there was not much difference in electrocatalytic activity for the oxygen reduction reaction. Therefore, we used the commercial available Whatman p-AAO membranes as templates for the fabrication of Pt-CNFs" with H_2PtCl_6 as platinum precursor.

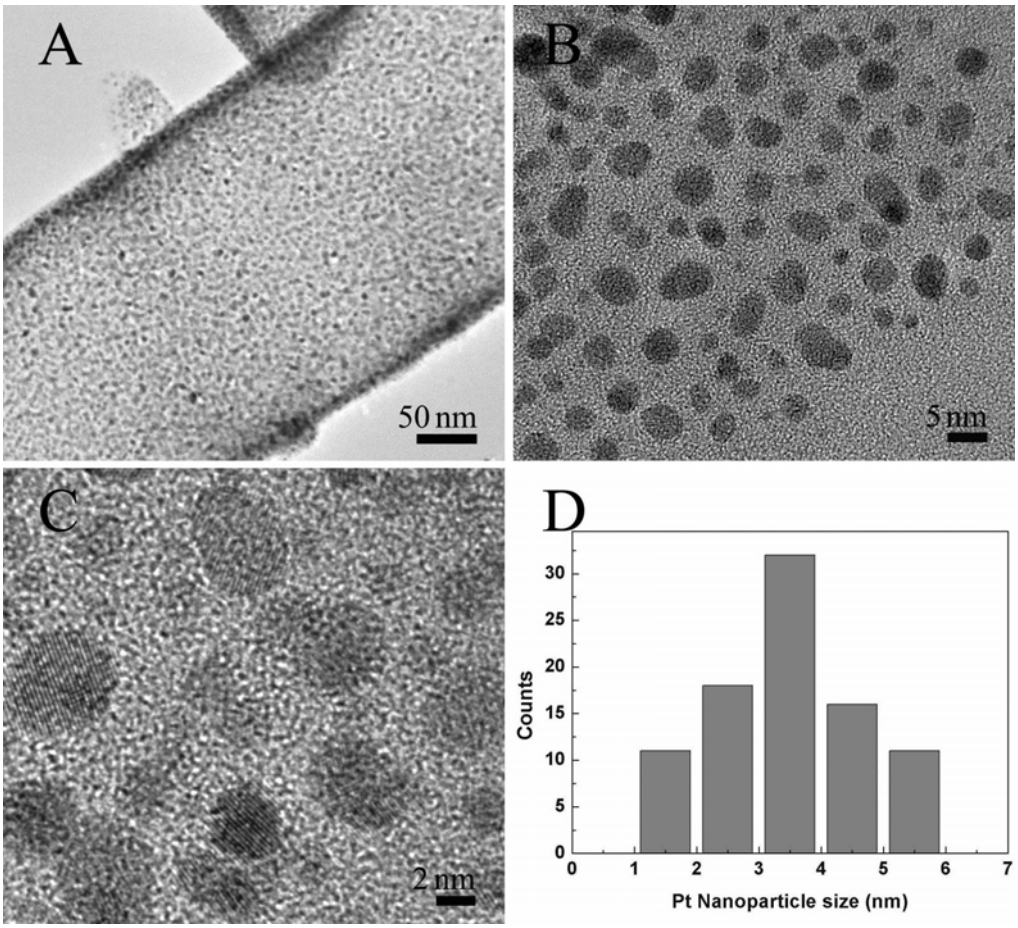

Figure 3-11. EM characterization of Pt-CNFs''.
(A), (B), (C) HRTEM images at different resolutions of the Pt-CNF'' fabricated using H_2PtCl_6 as platinum precursor; (D) the size distribution of the embedded Pt nanoparticles.

Table 3-2. Size distributions of platinum nanoparticles of the prepared catalyst samples.

Sample	HRTEM results (Number Average)		XRD (Volume Average)
	Mean Diameter (nm)	Standard Deviation (nm)	Mean Crystalline Size (nm)
Pt-CNFs	2.2	0.7	
Pt-CNFs'	2.3	0.6	
Pt-CNFs"	3.4	1.1	4.9
Pt-C	>20	>5	24
ETEK (20% Pt)	2.2	0.8	
Pt-CNFs" after fuel cell test	3.4	1.0	

3.4.2 Experimental

The fabrication procedure for Pt-CNFs" (Table 3-1) is the same as stated in section 3.1.1.2. The only difference is the substitution of $Pt(acac)_2$ with $H_2PtCl_6 \cdot 6H_2O$. The starting solution used is 6 wt% $H_2PtCl_6 \cdot 6H_2O$ in acrylonitrile with 0.1 wt% AIBN as initiator. All the other steps are the same.

3.4.3 Results and Discussion

HRTEM images at different resolution of the resulting Pt-CNFs" are shown in Figure 3-11. The platinum nanoparticles are highly dispersed in the PAN based amorphous carbon matrix, just like those in Pt-CNFs and Pt-CNFs'. However, the size of platinum particles is larger. The size distribution, Figure 3-11D, indicates that almost all particles are in the size range of 1.5 to 5.5 nm in diameter. Further statistical analysis shows that the mean diameter is 3.4±1.1 nm, with over 75% particles between 2.5 to 4.5 nm. The size distributions of prepared samples are summarized in Table 3-2.

The mass ratios of platinum in the starting solution for fabricating Pt-CNFs" and Pt-CNFs' are 2.26% and 0.496% ($Pt(acac)_2$ F.W.=393.31, Pt wt.%= 49.6%;$H_2PtCl_6 \cdot 6H_2O$ F.W.= 517.9, Pt wt.%=37.7%). If the same numbers of platinum particles form in the unit volume of starting solutions for both Pt-CNFs" and Pt-CNFs', the average volume ratio should be around 2.26%:0.496%, which equals to 4.56, and the size ratio would be 1.66. The average size ratio of platinum nanoparticles in Pt-CNFs" and Pt-CNFs' from HRTEM results is 3.4±1.1:2.3±0.6, which equals 1.48±0.61. These two data points match very well. Therefore, the number density of platinum rich domains, which is determined by the

diffusion ability of platinum precursor in polymer matrix, are similar for both the fabrication of Pt-CNFs' and Pt-CNFs". A larger amount of platinum precursor produces larger platinum nanoparticles.

Sizes of platinum nanoparticles in the prepared samples could also be obtained from XRD analysis (Figure 3-12). For both Pt-C and Pt-CNFs', the broad peak at around 23-24° is the characteristic peak of the amorphous carbon matrix. Peaks at around 39.6°, 46.1°, 67.3°, 81.1° and 85.6° correspond very well with the reported diffraction patterns on faces of (111), (200), (220), (311), and (222) of face-centered cubic (fcc) platinum.[23] According to Debye-Sherrer's equation

$$D = \frac{0.9\lambda}{\beta \cos\theta} \qquad (1)$$

average crystalline size of particles D is inversely related to the sharpness the peaks, where λ, β, and θ is the wavelength of X-ray source, the width at half height in radians, and the diffraction angle respectively. Pt-CNFs' present very broad platinum peaks in their diffraction patterns, which is characteristic of very small particles. Pt-C presents very sharp platinum peaks, which indicates the size of platinum nanoparticles is large. The wideness of peaks for Pt-CNFs" is in the middle of those of Pt-CNFs' and Pt-C. Therefore, the size of platinum nanoparticles is larger than that in Pt-CNF' and smaller than that in Pt-C. In addition to the platinum diffraction peaks, additional peaks with a 2θ value of 22.8°, 32.7°, and 53.0° were presented in the XRD curve of Pt-CNFs". It is difficult to assign these peaks to any specific species, although peaks at 32.7°, and 53.0° are most likely from diffraction of PtO_2. These peaks, which are also observed from commercial ETEK catalyst, may correspond to several platinum oxidized species, such as

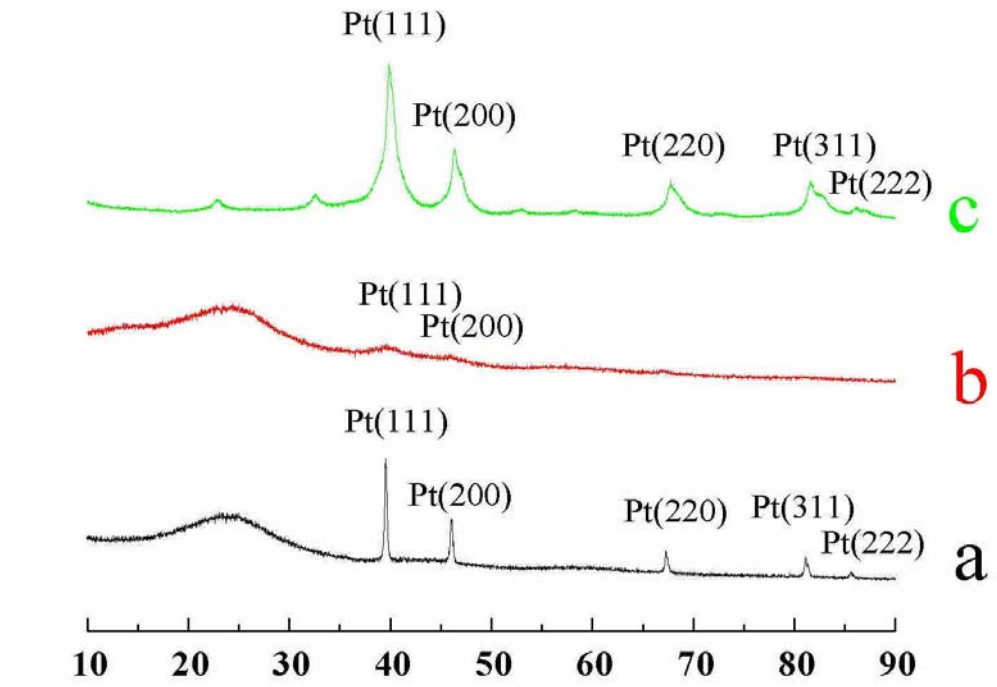

Figure 3-12. XRD characterizations of a) Pt-C, b) Pt-CNFs, and c) Pt-CNFs''.

PtO, PtO_2, or $Pt(OH)_x$.[20] The average diameters of platinum nanoparticles in Pt-C and Pt-CNFs" calculated using the Debye-Sherrer's equation from the (111) face[20] reflections are around 24 nm and 4.9 nm, respectively, which are slightly larger than those from the statistical results of HRTEM images. This is because XRD determines the volume-averaged crystal sizes,[24] while mean sizes from HRTEM images are the number average. Large size crystals weight more in volume average than in number average; therefore, the average sizes from XRD are larger than those from HRTEM. It is hard to determine the average size of platinum nanoparticles in Pt-CNFs' using the XRD pattern, since the platinum peak is too weak to be distinguished from the background.

3.5 Fuel Cell Test

3.5.1 Experimental

3.5.1.1 Pretreatment of Nafion 117 Film

To remove any organic impurities, commercial Nafion 117 films were pretreated by boiling in a 3 wt% H_2O_2 aqueous solution for one hour, followed by boiling in distilled water for one hour. Films were then treated in boiled 0.5M sulfuric acid aqueous solution for one hour to remove any metallic impurities and ensure the membrane was in the acid form. Afterwards, the film was immersed in boiled distilled water for another hour to remove any trace of acid. At last, the pretreated films were stored in distilled water for future use.

Table 3-3. Elemental analysis of the catalyst for PEMFC measurements.

Sample	Elemental mass ratio (%) (analyzed by Atlantic Microlab Inc)					Upper limit of Pt mass ratio (%)
	C	H	N	O	Cl	
Pt-CNFs'	59.50	12.25	1.98	13.17		13.1
Pt-CNFs"	16.15	1.01	2.97	10.96	Trace <0.25%	68.91
Pt-CFs	51.98	1.03	11.85	8.10	Trace 0.25%	27.04

Table 3-4. Membrane electrode assemblies prepared for fuel cell performance testing.

Sample	Cathode			Anode		
	Catalyst	Nafion ionomer loading (mg/cm^2)	Platinum loading (mg/cm^2)	Catalyst	Nafion ionomer loading (mg/cm^2)	Platinum loading (mg/cm^2)
MEA-1	ETEK (20% Pt)	0.8	0.2	ETEK (20% Pt)	0.8	0.2
MEA-2	Pt-CNFs'	<0.93	<0.15	ETEK (20% Pt)	0.8	0.2
MEA-3	Pt-CNFs"	<0.66	<0.56	ETEK (20% Pt)	0.8	0.2

3.5.1.2 Preparation of Catalyst Inks

Pt-CNFs', Pt-CNFs'' and ETEK catalyst inks were prepared by dispersing the respective catalyst (Pt-CNFs' or Pt-CNFs'' or ETEK (20 wt% Pt loading)) in 5 wt% Nafion alcohol solution with a mass ratio of catalyst to Nafion at 5 to 4. Afterwards, an appropriate amount of 2-propanol was added to the mixture. The addition of isopropanol would dilute the catalyst dispersion, which made the coated electrode layer more smooth and uniform. The slurry was ultrasonicated for over 30 minutes to form a uniform catalyst ink.[25]

3.5.1.3 Fabrication of Membrane Electrode Assemblies

Membrane electrode assemblies (MEA) were fabricated using the prepared catalyst ink. The platinum mass ratio of the prepared sample needs to be determined to calculate the platinum loading in MEAs. However, there is no direct way to get the platinum ratio because of the light elements in the sample (EDX and XPS could not detect H very well). Sample was analyzed by Atlantic Microlab Inc to determine the mass ratio of C, H, O, N and Cl (Table 3-3). The left mass margin would mainly be attributed to Pt (little amount of Al, Na may remain in sample after etching of p-AAO template).

The prepared catalyst inks were carefully coated to 5 cm^2 active regions on both sides of dry pretreated Nafion 117 films using a mask. To test the oxygen reduction performance of different catalysts, ETEK ink was used for anode; Pt-CNFs' ink, Pt-CNFs'' ink, and ETEK ink were used for cathode. As was shown in Table 3-3, three MEAs were fabricated for fuel cell testing. The amount of ink actually coated on Nafion

film was calculated by deducting the mass of remained ink from the mass of ink before coating. The total loadings of catalyst and Nafion ionomer, and the platinum loadings on each side of MEAs are listed in Table 3-4.

3.5.1.4 Construction of Fuel Cells

E-LAT carbon cloths with diffusion layer were used in the fuel cell test to assure proper electrical contact between the MEA and the graphite gas flow plates, and good gas diffusion (as was shown in Figure 1-3). To get better contact, carbon cloth with diffusion layer was pretreated. Each piece of carbon cloth with 5 cm^2 in area was uniformly coated with a mixture of 60mg 5 wt% Nafion alcohol solution and 0.1ml isopropanol and then heated at 110 °C for 10 minutes. The loading of Nafion ionomer on E-LAT carbon cloth was 0.6 mg/cm^2.

The fabricated membrane electrode assembly (MEA), having 5 cm^2 geometric electrode area, was sandwiched between two pieces of Nafion ionomer treated carbon cloth with5 cm^2 in area. No hot pressing was used for our experiments. Then the MEA with carbon cloth was loaded into a single-cell test fixture. The test cell was composed of, from one side to the other, cathode iron current-collector end plates, graphite O_2 gas-flow plates, Teflon films (with 5cm^2 area cut in the center), Nafion ionomer treated E-LAT carbon cloth, cathode catalyst layer, Nafion 117 film, anode catalyst layer, Nafion ionomer treated E-LAT carbon cloth, Teflon films, graphite H_2 gas-flow plates and anode iron current-collector end plates. The function of the Teflon film was to prevent fuel leaking. The single cell was connected to the TELEDYNE MEDUSA RD Fuel Cell Test

Station for PEMFC measurements.

3.5.1.5 PEMFC Measurements

Fuel cell polarization measurements were conducted on the TELEDYNE MEDUSA RD fuel cell test station with humidified H_2 and O_2 flow rates regulated at 0.1mL/S. The temperatures of anode, cathode, and cell were controlled to get a desired relative humidity and cell operation temperature. The cell was operated at three conditions: a)100% relative humidity at 80 °C (the settings are anode temperature 91 °C, cathode temperature 81 °C, cell temperature 80 °C), b) 70% relative humidity at 50 °C (the settings are anode temperature 50 °C, cathode temperature 45 °C, cell temperature 50 °C), and c) 100% relative humidity at 25 °C (the settings are anode temperature 25 °C, cathode temperature 25 °C, cell temperature 25 °C). For all MEAs, the PEMFC was first operated at 80 °C with 100% relative humidity first, then at 50 °C with 70% relative humidity, then at 25 °C with 100% relative humidity. Before each test, the cell was stabilized at that condition over night. Scan rate was set as 0.1 A/point and 20 seconds/point.

3.5.2 Results and Discussion

3.5.2.1 Structure of MEAs

The FE-SEM images of cathode catalyst layer of MEA-3, which is composed of Pt-CNFs" and Nafion ionomer, are shown in Figure 3-13A and B. Because of the long time sonication during the preparation of catalyst ink, nanofibers are broken into small

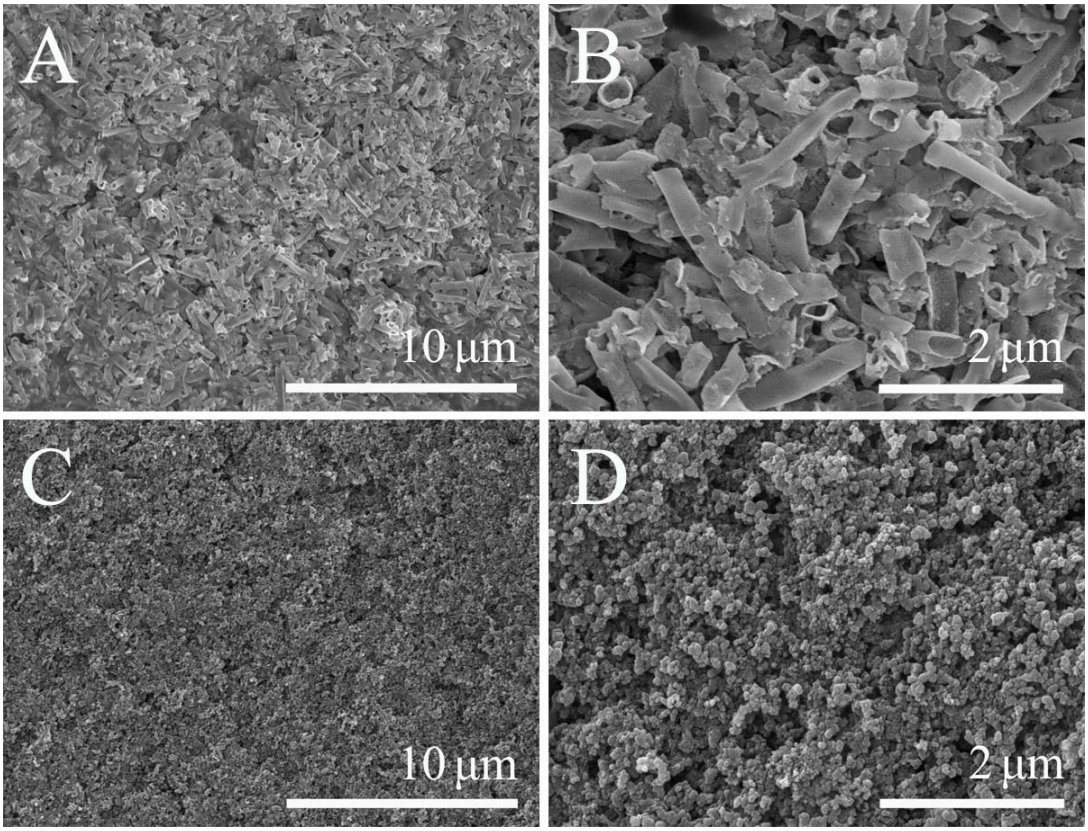

Figure 3-13. FE-SEM images of the cathode and anode of MEA-3.
(A), (B) FESEM images of the cathode of MEA-3 prepared by ink of Pt-CNFs" and Nafion alcohol solution; (C), (D) FESEM images of the anode of MEA-3 prepared by ink of ETEK catalyst and Nafion alcohol solution.

pieces around several microns in length. The broken pieces still keep the nanotube structure and form a uniform layer on the Nafion 117 film. The anode catalyst layer is a very uniform and porous layer (Figure 3-13C and D), which is composed of platinum-supported Vulcan-72 carbon particles and Nafion ionomer.

3.5.2.2 PEMFC Polarization Curves of the MEAs

Figure 3-14 shows the PEMFC polarization curves of three MEAs at different conditions, and Figure 3-15 is the performance comparison of three MEAs at each condition. As was shown in Figure 3-14A and B, ETEK catalyst performs the best at 80 °C with 100% relative humidity, while for Pt-CNFs' and Pt-CNFs" catalysts, the best condition is 50 °C with 70% relative humidity (Figure 3-14C to F). Open circuit voltage as high as 1.0V was achieved using Pt-CNFs" as cathode catalyst.

For MEA-3 (Pt-CNFs" catalyst as cathode), significant potential drops were recorded at high current densities for all test conditions. This is characteristic of the "diffusion-limited regime",[26] a region where potential drop is mainly determined by mass-transfer polarization. This phenomenon should stem from the structure of Pt-CNFs". Since platinum nanoparticles are embedded in a carbon matrix, it would be a little more difficult for oxygen to diffuse to the platinum surface in Pt-CNFs" than that in ETEK catalyst, where the platinum nanoparticles are on the surface of carbon powders. At high current density, the consumption of oxygen is too fast and a slow oxygen diffusion would limit the current. Therefore, diffusion control is more obvious for Pt-CNFs" catalyst and the potential drop is more pronounced at large current density for MEA-3.

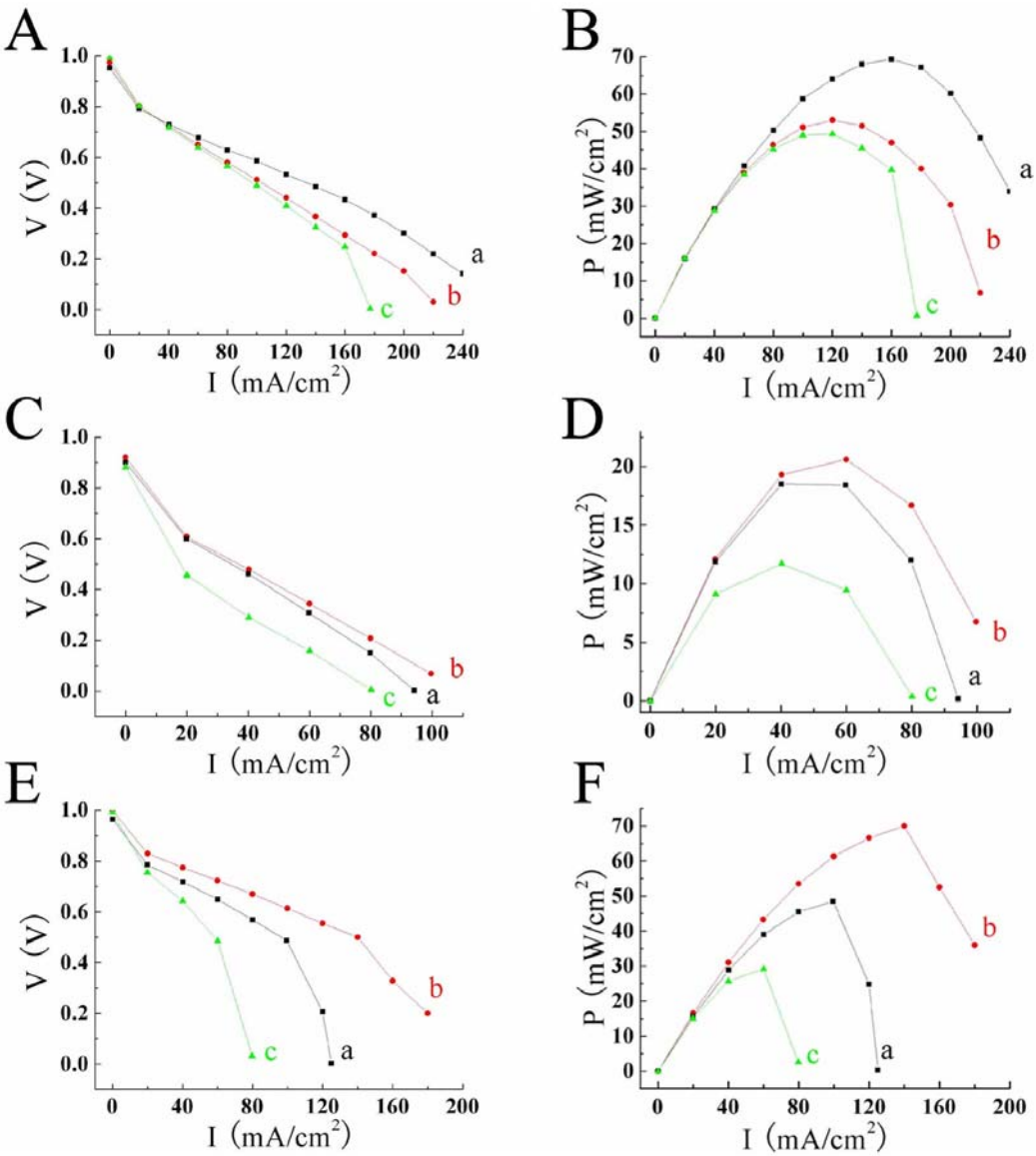

Figure 3-14. PEMFC polarization curves for each MEA at different conditions.
(A) and (B), (C) and (D), and (E) and (F) are PEMFC polarization curves for MEA-1, MEA-2, and MEA-3, respectively, at different conditions. (a, b, and c in cures correspond to testing at 80˚C 100% relative humidity, 50˚C 70% relative humidity, and 25˚C 100% relative humidity, respectively.)

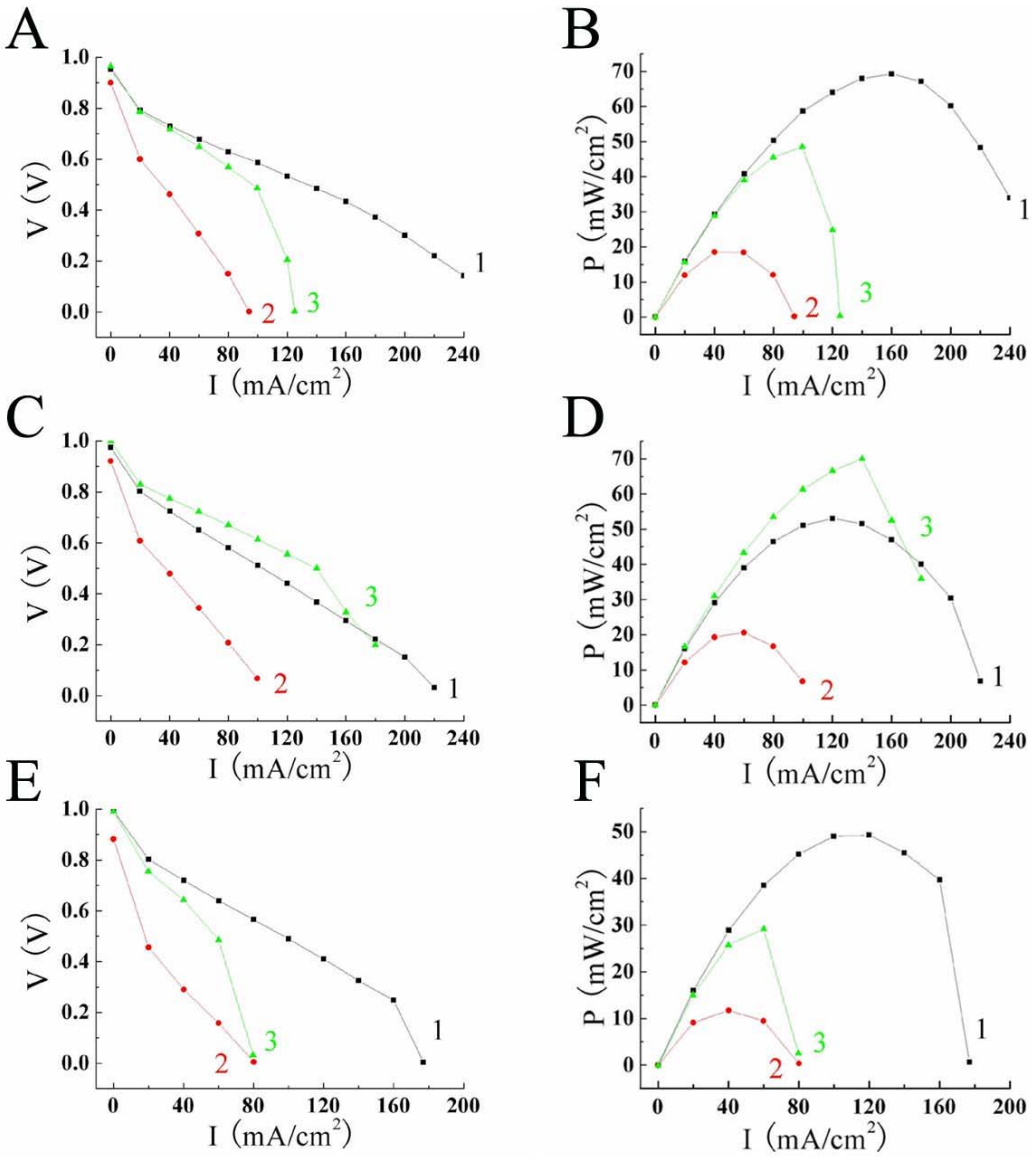

Figure 3-15. Comparison of PEMFC polarization curves of all MEAs at each condition.

(A) and (B), (C) and (D), and (E) and (F) are comparison of PEMFC polarization curves for all three MEAs at 80˚C 100% relative humidity, 50˚C 70% relative humidity, and 25˚C 100% relative humidity, respectively. (1, 2, and 3 in curves correspond to MEA-1, MEA-2, MEA-3, respectively.)

Normally, catalysts show better results at higher temperature, while for our case, operation at 50 °C with 70% relative humidity show the best results for both Pt-CNFs' and Pt-CNFs". The main reason lies in the water control at the cathode.[25] At 80 °C with 100% relative humidity, the water amount is too high and it tends to flood the catalyst layer, which would block the diffusion of fuel and reduce the efficiency of the catalyst. At 50 °C with 70% relative humidity, the water amount is much lower and the flooding effect is less pronounced. Therefore, the MEAs show much better performance.

ETEK catalyst performs much better than Pt-CNFs' and Pt-CNFs" catalyst at 80 °C with 100% relative humidity and 25 °C with 100% relative humidity (Figure 3-15A,B,E, and F). However, at 50 °C with 70% relative humidity, MEA-3 gives the best results (Figure 3-15C and D). Considering the platinum loading at cathode of different MEAs, the ETEK catalyst possesses the highest specific platinum efficiency. This is contrary to the results of RDE experiments (section 3.3.4), where the Pt-CNFs' shows better electrocatalytic activity than ETEK catalyst. This indicates that the techniques for the preparation of catalyst ink and MEAs do not work well with Pt-CNFs' and Pt-CNFs", structures of which is clearly different form that of a common catalyst, e.g. E-TEK.

3.5.2.3 PEMFC Voltage Decay Study of the MEAs

Figure 3-16 shows voltages of test cells with three different MEAs operated at a constant current of 0.02A/cm^2 for over 20 hours at 80 °C with 100% relative humidity. MEA-1 with the ETEK catalyst as cathode shows the highest overall voltages at this condition, followed by MEA-3 (with Pt-CNFs"), then MEA-2 (with Pt-CNFs').A linear

approximation of the voltage decay rates for these three MEAs yields $5.21*10^{-7}$ V/s, $3.10*10^{-7}$ V/s, and $5.68*10^{-7}$ V/s, which equal to 1.9 mV/h, 1.1 mV/h, and 2.0 mV/h, for MEA-1, MEA-2, and MEA-3, respectively. These data suggest that MEA-3, or the Pt-CNFs' catalyst show better durability than ETEK catalyst and Pt-CNFs". This may due to the special structure of Pt-CNFs'. Since the platinum nanoparticles are embedded in carbon matrix in Pt-CNFs' instead of sticking on the surface of carbon (as for ETEK catalyst), it is more difficult for the coalescence of platinum nanoparticles to happen via migration on the carbon support during the PEMFC operation. While for Pt-CNFs", although it possesses similar structure to Pt-CNFs', the platinum loading is much higher and the carbon matrix is much lower. Therefore, the platinum agglomeration by corrosion of the carbon support would show strong effect and make the decay rate bigger. Compared with some published data (25 μA/hr),[24] the voltage decay rate of ETEK catalyst during the fuel cell operation is too fast. Optimization of the cell assembly needs to be studied.

3.5.2.4 Structures of Platinum Nanoparticles after PEMFC Measurements

Pt-CNFs" from the cathode of MEA-3 after fuel cell testing was characterized using HR-TEM to study the stability of platinum nanoparticles. As was shown in Figure 3-16, after fuel cell testing for over 160 hours, the structure of Pt-CNFs" does not change. The platinum nanoparticles are still highly dispersed in amorphous carbon matrix. The statistical analysis of the size of platinum nanoparticles shows that the average diameter is 3.4±1.0nm, with around 75% of particles in the range of 2.5 to 4.5nm. The size of

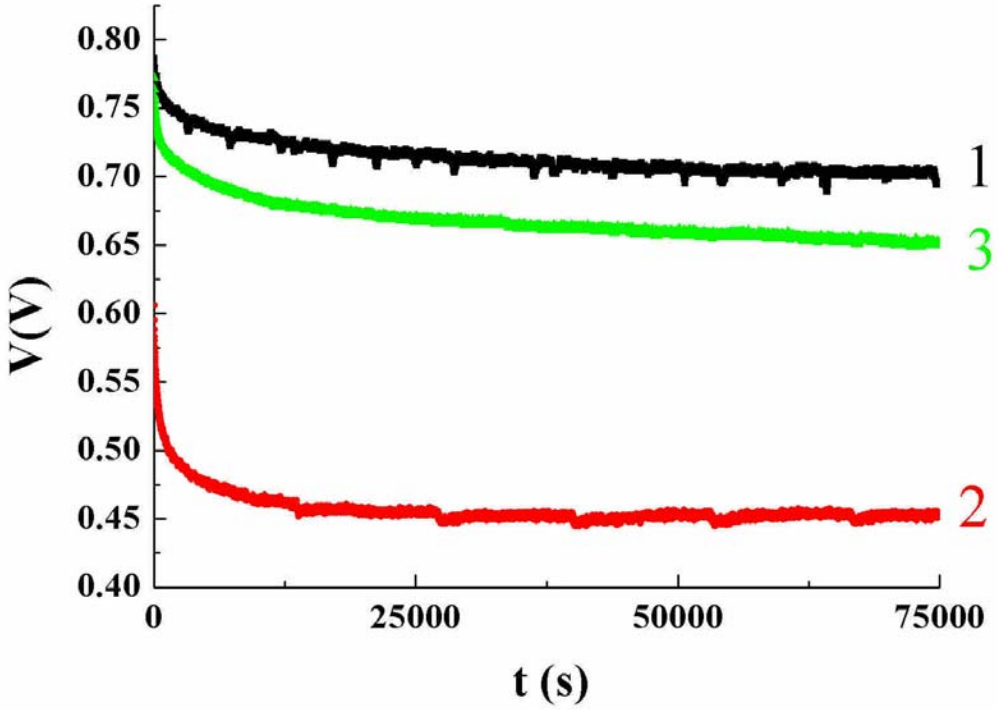

Figure 3-16. Fuel cell measurements of three MEAs at constant current density of 0.02 mA/ cm^2.

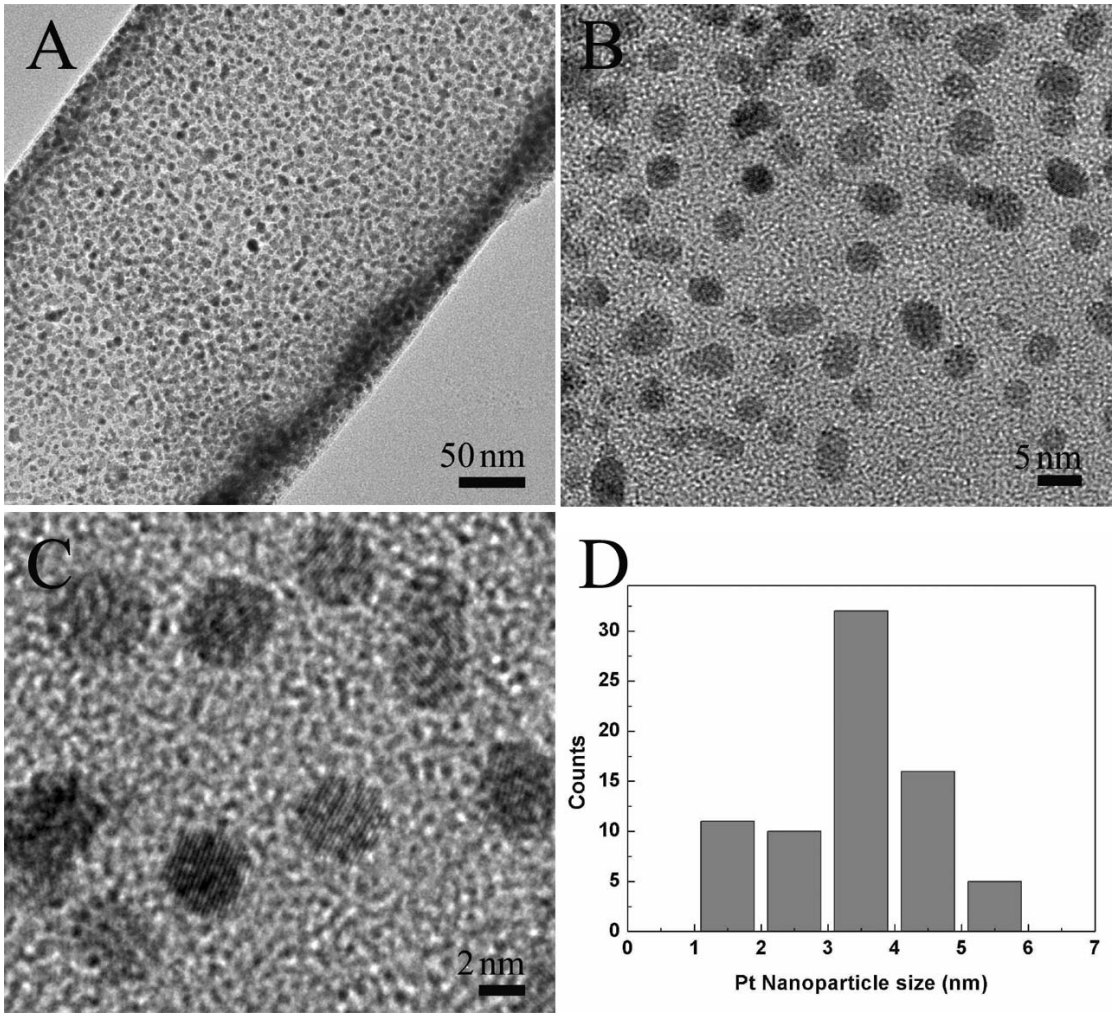

Figure 3-17. EM characterization of Pt-CNFs'' catalyst after PEMFC measurements. (A), (B), (C) HRTEM images at different resolutions of the Pt-CNF'' after PEMFC measurements for 170 hours; (D) the size distribution of the embedded Pt nanoparticles after fuel cell test.

platinum nanoparticles after the fuel cell measurements is essentially the same as that before measurements (as discussed in section 3.4.2), which suggests that no aggregation or coalescence happened after the 160 hours PEMFC measurements.

3.6 Concluding Remarks

Porous AAO templates enable *in situ* fabrication of PAN-based carbon nanofibers containing highly dispersed Pt nanoparticles. By changing the platinum precursor mass ratio, embedded platinum nanoparticles with different mean diameters could be prepared. RDE voltammetry shows that these new composite materials have a better electrocatalytic activity than commercial ETEK catalyst and similar materials fabricated via more complicated procedures.

The PEMFC measurement of the MEAs made from the Pt-CNFs' and Pt-CNFs'' did not show the positive results as we expected. Considering all the effects, the main reason could be the techniques of making MEAs do not adapt well to the prepared catalyst. Future research should focus on optimizing the techniques for ink preparation and coating process. The best operation conditions of the prepared catalyst should also be determined.

3.7 References

(1) Joo, S. H.; Choi, S. J.; Oh, I.; Kwak, J.; Liu, Z.; Terasaki, O.; Ryoo, R. *Nature* **2001**, *412*, 169-172.

(2) Rajesh, B.; Karthik, V.; Karthikeyan, S.; Thampi, K. R.; Bonard, J. M.; Viswanathan, B. *Fuel* **2002**, *81*, 2177-2190.

(3) Wang, C.; Waje, M.; Wang, X.; Tang, J. M.; Haddon, R. C.; Yan, Y. *Nano Lett.* **2004**, *4*, 345-348.

(4) Tang, H.; Chen, J.; Huang, Z.; Wang, D.; Ren, Z.; Nie, L.; Kuang, Y.; Yao, S. *Carbon* **2004**, *42*, 191-197.

(5) de Heer, W. A.; Chatelain, A.; Ugarte, D. *Science* **1995**, *270*, 1179-1180.

(6) Kong, J.; Franklin, N. R.; Zhou, C.; Chapline, M. G.; Peng, S.; Cho, K.; Dai, H. *Science* **2000**, *287*, 622-625.

(7) Martin, C. R. *Science* **1994**, *266*, 1961-1966.

(8) Li, F.; Zhang, L.; Metzger, R. M. *Chem. Mater.* **1998**, *10*, 2470-2480.

(9) Shingubara, S. *J. Nanoparticle Res.* **2003**, *5*, 17-30.

(10) Hulteen, J. C.; Chen, H. X.; Chambliss, C. K.; Martin, C. R. *Nanostructured Mater.* **1997**, *9*, 133-136.

(11) Rahman, S.; Yang, H. *Nano Letters* **2003**, *3*, 439-442.

(12) Gao, H.; Mu, C.; Wang, F.; Xu, D.; Wu, K.; Xie, Y.; Liu, S.; Wang, E.; Xu, J.; Yu, D. *J. Appl. Phys.* **2003**, *93*, 5602-5605.

(13) Masuda, H.; Fukuda, K. *Science* **1995**, *268*, 1466-1468.

(14) Jessensky, O.; Muller, F.; Gosele, U. *Appl. Phys. Lett.* **1998**, *72*, 1173-1175.

(15) Liu, Z.; Lee, J. Y.; Chen, W.; Han, M.; Gan, L. M. *Langmuir* **2004**, *20*, 181-187.

(16) Ye, S.; Vijh, A. K.; Dao, L. H. *J. Electrochem. Soc.* **1997**, *144*, 90-95.

(17) Bu, H.; Rong, J.; Yang, Z. *Macromol. Rapid Commun.* **2002**, *23*, 460-464.

(18) Xu, T. T.; Piner, R. D.; Ruoff, R. S. *Langmuir* **2003**, *19*, 1443-1445.

(19) Cheng, B.; Murry, C. W.; Samulski, E. T. *Mater. Res. Soc. Symp. Proc.* **2003**, *737*, 413-417.

(20) Fachini, E. R.; Diaz-Ayala, R.; Casado-Rivera, E.; File, S.; Cabrera, C. R. *Langmuir* **2003**, *19*, 8986-8993.

(21) Dai, J.; Bruening, M. L. *Nano Lett.* **2002**, *2*, 497-501.

(22) Poirier, J. A.; Stoner, G. E. *J. Electrochem. Soc.* **1994**, *141*, 425-430.

(23) Pt:4-0802. *1971 Inorganic Index to the powder diffraction*.

(24) Ferreira, P. J.; la O', G. J.; Shao-Horn, Y.; Morgan, D.; Makharia, R.; Kocha, S.; Gasteiger, H. A. *J. Electrochem. Soc* **2005**, *152*, A2256-A2271.

(25) Antolini, E. *J. Appl. Electrochem.* **2004**, *34*, 563-576.

(26) Arico, A. S.; Creti, P.; Kim, H.; Mantegna, R.; Giordano, N.; Antonucci, V. *J. Electrochem. Soc.* **1996**, *143*, 3950-3959.

Chapter IV: Fabrication of Platinum Nanoparticle-Embedded Carbon Fibers Using Electrospinning

4.1 Introduction

One-dimensional nanomaterials have attracted broad interest due to their unique characteristics and potential applications.[1,2] Among the various fabrication methods, electrospinning is simple, versatile and low-cost. A variety of nanofibers,[3-9] including polymers, ceramics, and composites, can be fabricated using electrospinning. The prepared nanofibers are extraordinary long, uniform and tunable in diameter (typically between 50-500nm), and possess ultra high surface area per unit mass. These fibers might be applied to many areas,[10-12] such as nanosensors, magnetic device and solar cells.

The standard setup for electrospinning includes a high-voltage power supply, a capillary spinneret with a metallic needle, and a grounded collector. Sometimes, a syringe pump is used to control the flow rate of solution. In a typical electrospinning process, a high voltage is applied between the needle and the collector, and the induced electrostatic field charges the surface of a polymer solution (or melt) droplet. When the applied electric field overcomes the surface tension of the droplet, a charged liquid jet will be ejected through the capillary spinneret. The route of the charged jet is controlled by the electric field. The repulsive forces between the charges carried with the jet enormously stretch the jet to form continuous, ultrathin fibers to be collected on the substrate screen. Final structures of electrospun fibers depend on the system parameters, such as the molecular weight, molecular weight distribution, architecture of polymer, and the viscosity, conductivity and surface

tension of solution, and the process parameters, such as the electric potential, distance between the needle and collector, and flow rate.[10] Generally, when the other parameters are fixed, a larger electric potential, a larger needle-to-collector distance, a smaller flow rate, and a lower concentration of polymer solution will produce nanofibers with a smaller diameter.

This chapter describes the method of making platinum-embedded carbon fibers (Pt-CFs) using electrospinning. Furthermore, the polymer electrolyte membrane fuel cell (PEMFC) performance of the fabricated Pt-CFs is studied.

4.2 Materials and instrumentation

Materials: Chloroplatinic acid hexahydrate ($H_2PtCl_6 \cdot 6H_2O$, Sigma Aldrich), polyacrylonitrile (PAN, Aldrich), laboratory film (Parafilm), platinum (II) acetylacetonate ($Pt(acac)_2$, $Pt(II)(CH_3COCHCOCH_3)_2$, 49.6% Alfa Aesar), and N,N-dimethylformamide (DMF, $HCON(CH_3)_2$, American Burdick & Jackson) were used as received, unless stated otherwise.

Instrumentation: A high voltage power supply (Gamma High Voltage Research ES-30P, 5 Watt, maximum voltage 30 kV, and maximum current output 160 μA) was used to provide the high potential for electrospinning. The experiments were conducted in a homemade electrospinning setup. The surface morphology of the prepared Pt-CFs and the structures of embedded platinum nanoparticles were characterized by field emission scanning electron microscopy (FE-SEM, Hitachi S4700) and high resolution transmission electron microscopy (HRTEM, JEM-2010F-FasTEM), respectively. An energy dispersive X-ray (EDX) spectrometer installed in a JEOL JEM6300 was used for elemental analysis. Selected area electron diffraction (SAED) installed in a JEOL JEM-100CXII was used to determine

the crystalline structure of the materials. PEMFC tests of Pt-CFs were conducted in TELEDYNE MEDUSA RD Fuel Cell Test Station.

4.3 Fabrication of Platinum-Embedded Carbon Fibers Using Electrospinning

4.3.1 Experimental

The polymer solution for electrospinning was prepared by refluxing the mixture of $H_2PtCl_6 \cdot 6H_2O$, PAN and DMF with a mass ratio of 1:2:18 at 100˚C for 2 hours.[13] The prepared polymer solution with platinum salt dissolved was clear and viscous.

The schematic diagram of the homemade electrospinning equipment is shown in Figure 4-1. For safety, all parts except the power supply were placed in a Plexiglas box (45cm*40cm*60cm). The front side of the box was hinged to act as a door. A syringe with a blunt-end needle (22 gauge) was inserted into a small circular opening in the center of the top plate of the box. A grounded circular copper plate collector (15 cm in diameter) was placed on a grounded lab jack, so that the distance between the needle and the collector could be varied.

The polymer solution for electrospinning was stored in the syringe. The flow rate of solution was controlled by gravity and electrical field. 10 kV was applied between the needle and the copper plate collector. The gap between the tip of the needle and the surface of collector was adjusted to 10 cm; therefore, the electric field was around 1kV/cm. To make the electrospun nanofiber film easy to peel off, the copper collector was covered with a thin layer of parafilm.

After electrospinning, the nanofiber film composed of PAN and platinum salt was heated at 700˚C for 6 hours in vacuum to pyrolyze the PAN and reduce the Pt salt to

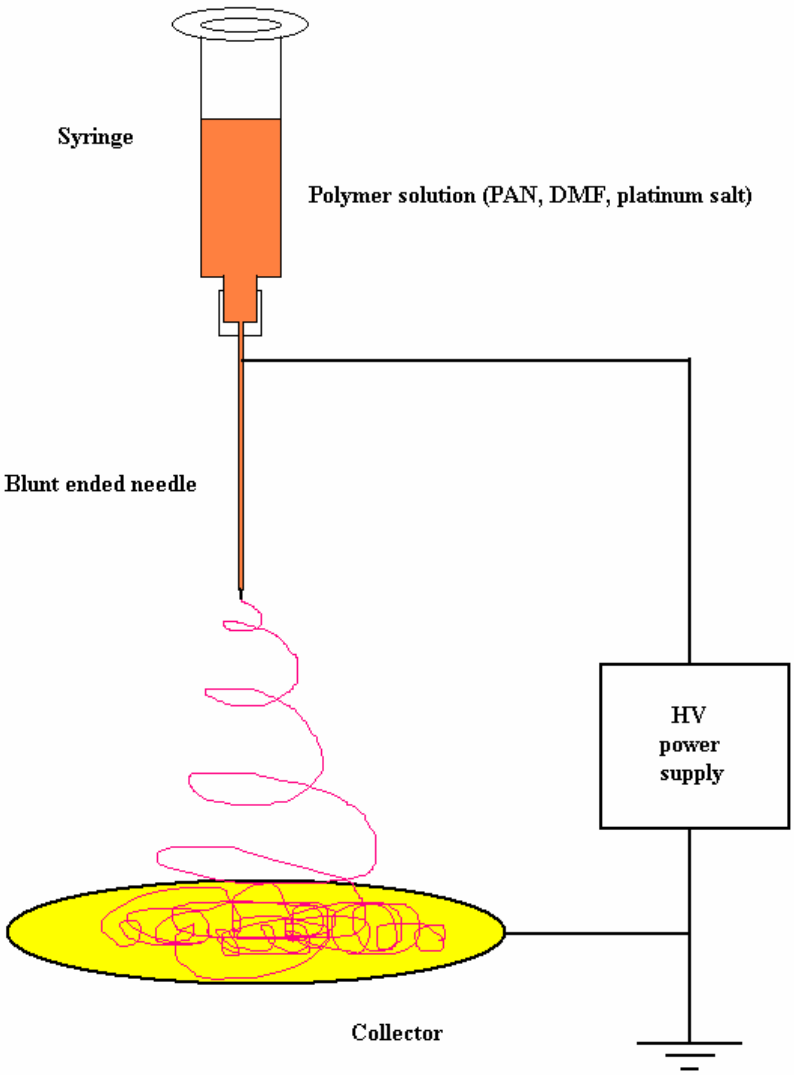

Figure 4-1. Schematic diagram of the homebuilt electrospinning setup.
The high voltage power supply provides an electric field at 1 kV/cm. Polymer solutions stored in the syringe is electrospun through the needle under the electric field. The electrospun fine fibers are collected by the grounded collector.

elemental platinum. Pyrolysis at 900˚C was also conducted for comparison to study the growth of platinum nanoparticles at different temperatures.

Electrospun fibers using $Pt(acac)_2$ as platinum precursor were prepared following the same procedure. To study the effect of electrospinning on the structure of products, Pt-C composite was prepared using the same starting polymer precursor in bulk by pyrolysis at 700 ˚C for 6 hours without the electrospinning process.

4.3.2 Results and Discussion

4.3.2.1 Pt-CFs Prepared at 700 ˚C

The fabricated Pt-CFs were characterized using FE-SEM and HRTEM. As shown in the FE-SEM images (Figure 4-2A and B), the prepared fibers, with a mean diameter ~0.5 μm, are nondirectional. The clear FE-SEM image (no Au was sputter coated) suggests the material has very good electron conductivity. Figure 4-2C shows the HRTEM image of the prepared materials. Platinum nanoparticles (black spots) are uniformly distributed in carbon fibers with a medium diameter around 3 nm. No statistical analysis was conducted to determine the exact size distribution of platinum nanoparticles, since the edges of many embedded platinum nanoparticles are hard to resolve.

Figure 4-2 parts E and D show the EDX results of the sample before and after the pyrolysis. Before heating, there are three strong peaks, C, Pt and Cl; while after heating, only Pt and C peaks remain. The disappearing of Cl peak suggests that H_2PtCl_6 is decomposed and reduced to elemental platinum during the pyrolysis of PAN. Elemental analysis results by Atlantic Microlab Inc. are listed in Table 3-3. The mass percentage of Pt is less than 27 wt%, and the amount of chlorine is undetectable.

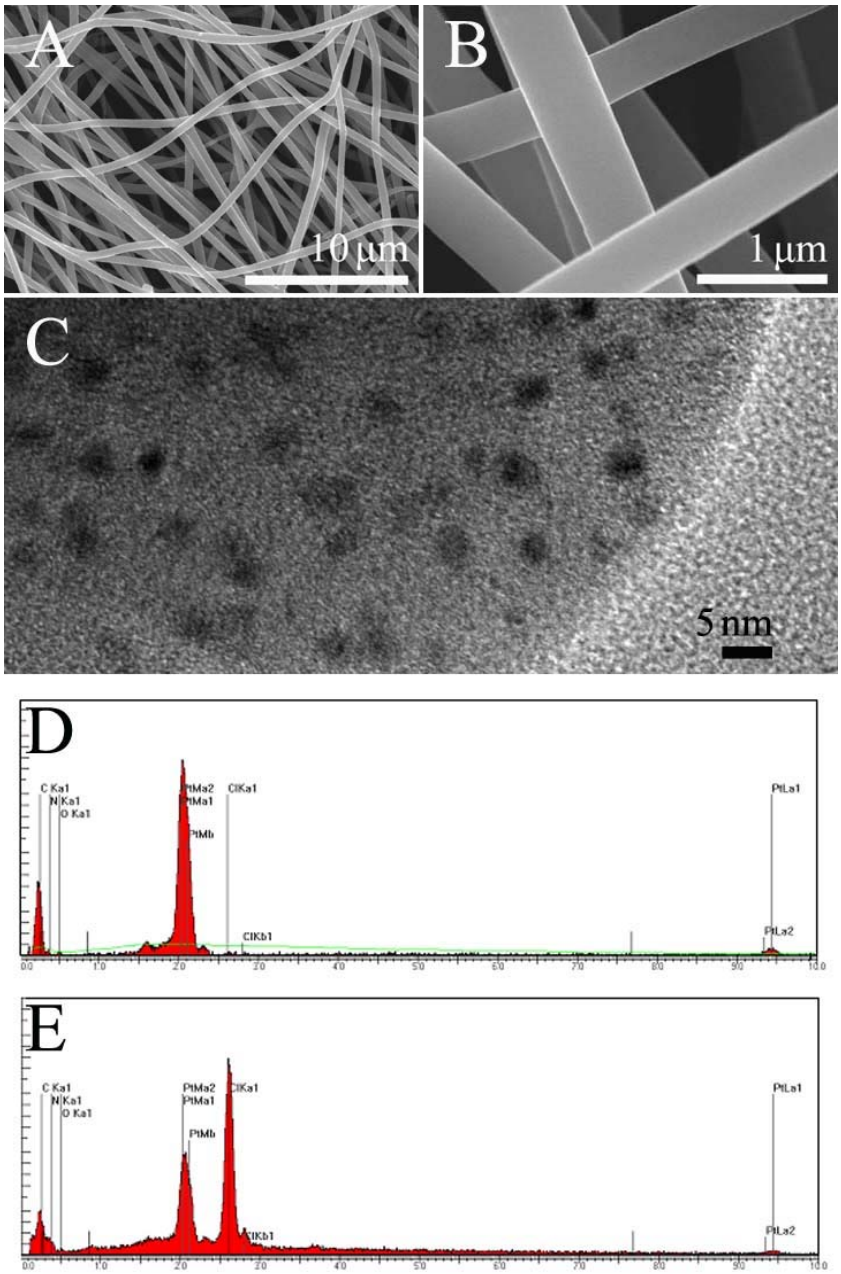

Figure 4-2. Pt-CFs prepared using electrospinning and pyrolysis at 700°C.
(A), (B) FE-SEM and (C) HRTEM images of Pt-CFs after electrospinning and pyrolysis at 700°C for 6 hours; EDX analysis of the sample after (D) and before(E) pyrolysis. The black spots in (C) are Pt nanoparticles.

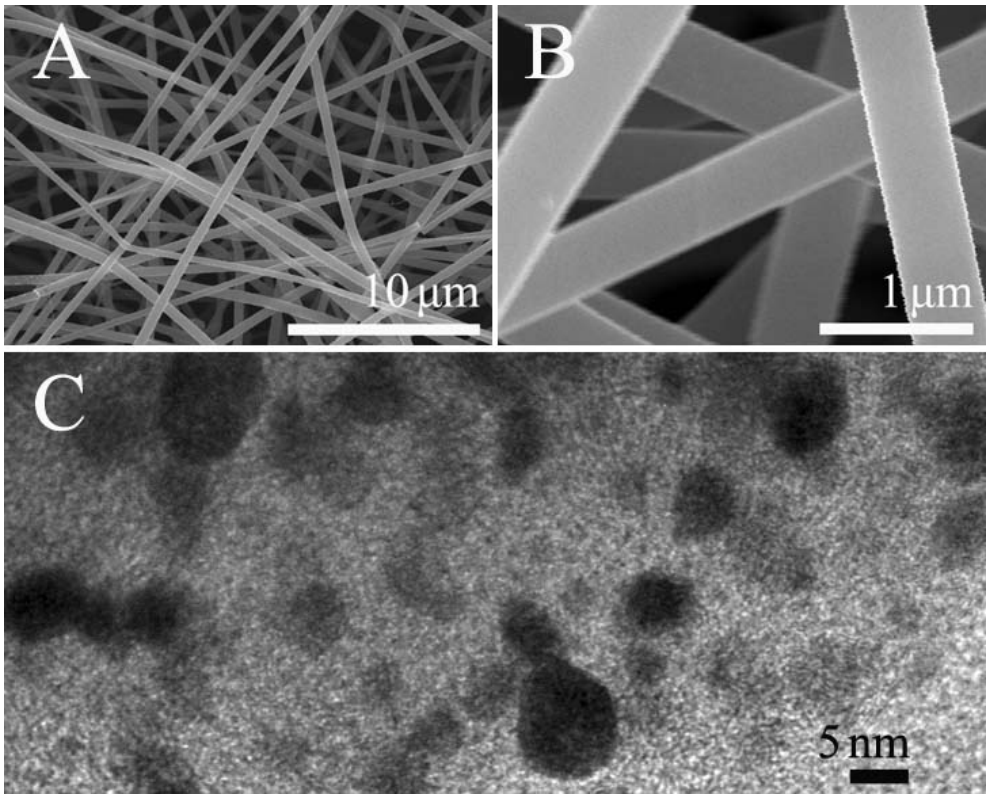

Figure 4-3 Pt-CFs prepared using electrospinning and pyrolysis at 900°C.
(A), (B) FE-SEM and (C) HRTEM images of Pt-CFs after electrospinning and pyrolysis at 900°C for 6 hours. The black spots in (C) are Pt nanoparticles.

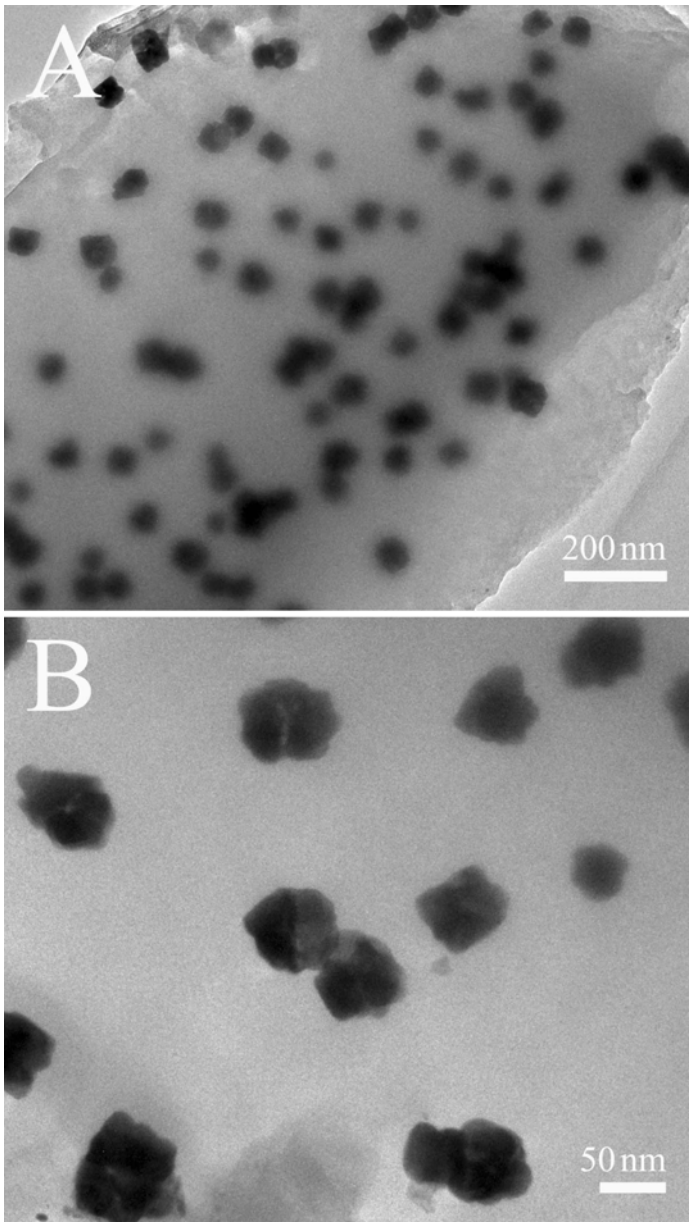

Figure 4-4. HRTEM images of Pt-C composites prepared at 700°C with no electrospinning process.

4.3.2.2 Pt-CFs Prepared at 900 ˚C

Figure 4-3 parts A and B show the FE-SEM images of the Pt-CFs pyrolysis at 900°C for 6 hours. The average diameter of carbon fibers is almost the same as those at 700°C. However, the structure of the embedded platinum nanoparticles changes a lot. As shown in Figure 4-3C (HRTEM image), platinum nanoparticles are larger than those in Figure 4-2C. Particles over 10nm are observed. This indicates that serious aggregation and coalescence of platinum nanoparticles happened during pyrolysis at 900°C.

According to the Stokes-Einstein equation,[14]

$$D = \frac{k_b T}{6\pi\eta R}$$

the diffusion coefficient D of isolated spherical particles (with radius R) in a viscous medium (viscosity η) is linearly related to the absolute temperature T. Therefore, at 900°C, the diffusion of platinum nanoparticles is faster, which could induce aggregation of platinum nanoparticles and subsequent coalescence. The nanoparticles might also grow through the solid state through diffusion-driven Ostwald ripening:[15] the growth of larger particles at the expense of smaller ones which have a higher solubility.

4.3.2.3 Effect of Electrospinning on the Size of Platinum Nanoparticles

Figure 4-4 shows the HRTEM images of Pt-C prepared using the same starting solution by pyrolysis at 700°C for 6 hours without the electrospinning step. The embedded platinum particles are much larger (mean diameter ~50 nm) than those in Figure 2-3C. This suggests that the electrospinning process is important for controlling the size of platinum nanoparticles. The obtained fiber structure after electrospinning possesses a much larger specific surface area. The mobility of polymer chains at the air/fiber interface is greatly

decreased similar to those in contact with a substrate,[16] which could also restrict movement of the entangled polymer chains inside the fiber. Since each fiber is only hundred nanometers wide, almost all polymer molecules would feel this effect. Therefore, the diffusion coefficients of platinum salt and elemental platinum nanoparticles in the PAN nanofibers are much less than that in PAN bulk. These effects might account for the much smaller platinum nanoparticles (around 3 nm) seen embedded in the carbon fiber matrix.

4.3.2.4 Electrospun Fibers Prepared Using $Pt(acac)_2$ as Platinum Precursor

Figure 4-5 (A) shows the TEM image and SAED of the product using $Pt(acac)_2$ as platinum precursor after pyrolysis at 700 °C for 6 hours. However, it is hard to distinguish platinum nanoparticles in the carbon nanofibers and no Pt diffraction appeared under SAED (the rings are from the diffraction of the amorphous carbon fiber matrix). The EDX elemental analysis further confirms that the strong Pt peak before electrospinning disappears after heat treatment (Figure 4-5B and C).

The reason for the platinum loss apparently stems from the use of $Pt(acac)_2$. $Pt(acac)_2$ is known to undergo sublimation without thermal degradation in the temperature range of 160 to 170 ˚C.[17] During the heating process, $Pt(acac)_2$ near the surface of electrospun fibers could evaporate out of the polymer matrix before the decomposition reaction happens. Since electrospun fibers possess ultrahigh specific surface area, a large amount of platinum salt is lost during heating. The sublimed platinum salt is decomposed to black metal powder on the reaction vessel wall. This is not the case for the fabrication of platinum-embedded carbon nanofibers using p-AAO membrane templates (chapter 3), because $Pt(acac)_2$ is trapped by the p-AAO channels during heat treatment, preventing evaporation out of the polymer matrix.

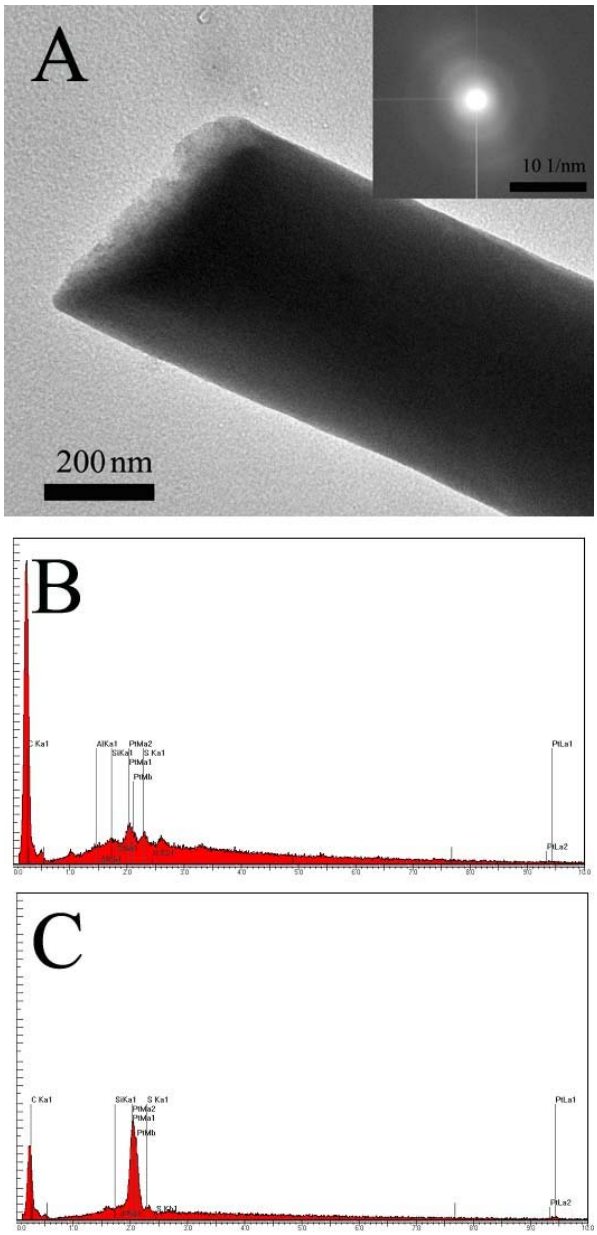

Figure 4-5 Pt-CFs prepared at 700°C using $Pt(acac)_2$ precursor.
(A) TEM images of Pt-CFs prepared using $Pt(acac)_2$ precursor after electrospinning and pyrolysis at 700°C for 6 hours; EDX analysis of the sample after (B) and before (C) pyrolysis. The upper-right inset in A is a SAED pattern.

To get platinum nanoparticles embedded in carbon fibers using $Pt(acac)_2$ as precursor, an extra step of chemical reduction (using hydrogen) is necessary before pyrolysis.[18,19]

4.4 Fuel Cell Test

4.4.1 Preparation of Cathode with Electrospun Pt-CFs Film

A 5 cm^2 electrospun Pt-CF film was pretreated with a 5 wt% Nafion-alcohol solution as stated in section 3.5.1.4. Then the Nafion-coated Pt-CF film was directly sandwiched between a piece of carbon cloth with a diffusion layer and a Nafion 117 film on the cathode side. The ink method was used to prepare the anode of MEA using ETEK catalyst (20% Pt loading) as stated in section 3.5.1.2. The prepared MEA was sandwiched in the single-cell test fixture and the PEMFC measurements were carried out on a TELEDYNE MEDUSA RD Fuel Cell Test Station at 80 °C with 100% relative humidity.

The polarization curve is shown in Figure 4-6. Although the open circuit voltage is around 0.75V, it could not support much current. Voltage dropped dramatically after a small current was added. This may be induced partly due to bad contact among the Pt-CF film, carbon cloth and Nafion film. The main reason for low power density is that most of the platinum nanoparticles are embedded in carbon fibers as shown in Figure 4-2A and are not accessible to oxygen.

4.4.2 Preparation of Cathode with Pt-CFs Using the Ink Method

A MEA was also prepared using the ink method. The electrospun Pt-CFs were first sonicated in ethanol for two hours to destroy the web structure and make separated fibers. Afterwards, the separated Pt-CFs were dispersed in Nafion-alcohol solution under sonication

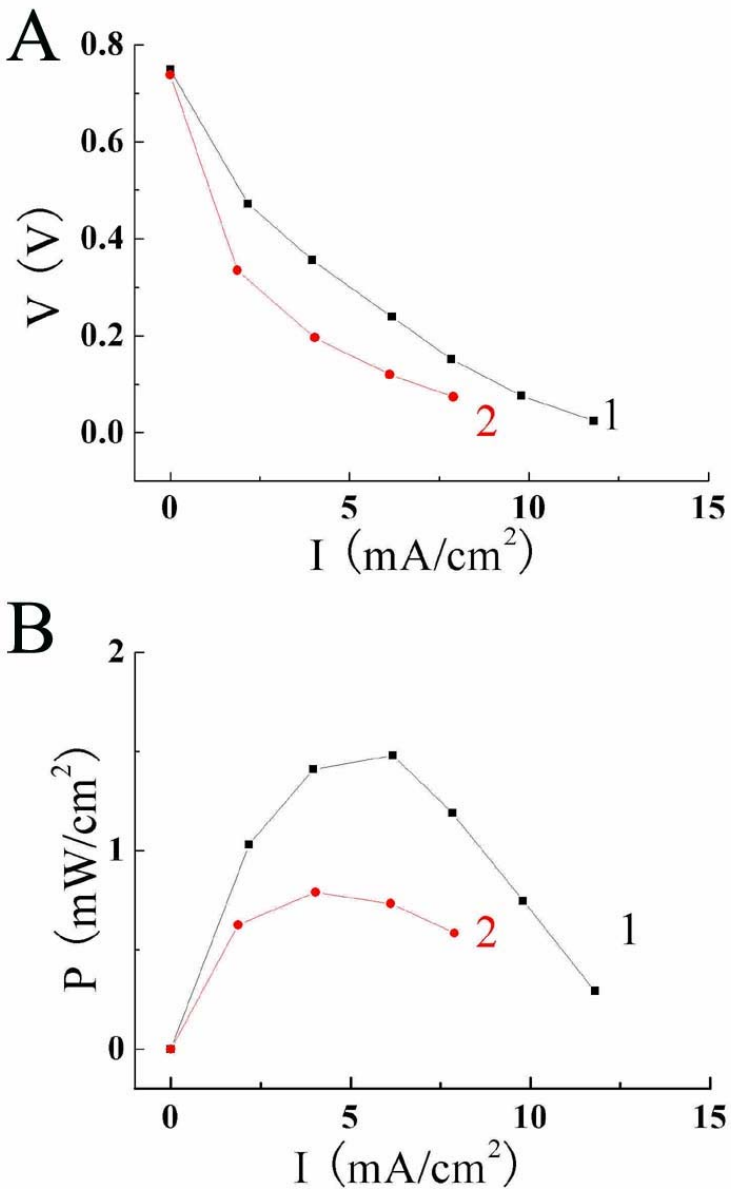

Figure 4-6 PEMFC polarization curves for MEAs with Pt-CFs.
PEMFC (A) I-V and (B) I-P curves for (1) MEA prepared with Pt-CFs film and (2) MEA with Pt-CFs ink at 80˚C with 100% relative humidity.

to prepare Pt-CF catalyst ink. The mass ratio of Pt-CFs to Nafion ionomer was 5:4. Even after sonication for over one hour, Pt-CFs still could not be dispersed well in Nafion solution; Pt-CFs were aggregated in the solution. The prepared catalyst ink was then coated on one side of Nafion film as cathode catalyst. ETEK catalyst was coated on the other side for anode reaction. The MEA was sandwiched in the test cell and connected to the Medusa test station for PEMFC measurements at 80 °C with 100% relative humidity.

Just as the PEMFC prepared with the Pt-CF film, the cell with Pt-CF ink could not support much current (Figure 4-6). This could partly be attributed to the bad quality ink prepared with Pt-CFs. Still, the most important reason for low current density is that most of the platinum nanoparticles are covered by carbon and are not active for the reduction of oxygen.

4.5 Concluding Remarks

In conclusion, by electrospinning the PAN solution with H_2PtCl_6 dissolved, PAN fibers with platinum salt embedded could be fabricated at an electric field of 1 kV/cm. During the pyrolysis of PAN (700 ˚C), platinum salt is decomposed and reduced to platinum metal coincidently. The platinum nanoparticles embedded in carbon fibers are narrowly distributed with a mean diameter around 3 nm. Pyrolysis at higher temperature (900 ˚C) produced much larger platinum nanoparticles. The prepared Pt-CFs was applied to a PEMFC test in either a film structure or a separated fiber structure (catalyst ink). However, because most of platinum nanoparticles are not accessible to oxygen, as well as incompatibility of Pt-CFs with conventional MEA preparation techniques, PEMFCs with Pt-CFs could not support much current. For better fuel cell performance, Pt-CFs need to be post treated to form a

porous structure and expose more platinum nanoparticles to oxygen fuel. A more suitable ink preparation technique needs to be developed.

4.6 References

(1) Pan, Z. W.; Dai, Z. R.; Wang, Z. L. *Science* **2001**, *291*, 1947-1949.

(2) Duan, X.; Huang, Y.; Cui, Y.; Wang, J.; Lieber, C. M. *Nature* **2001**, *409*, 66-69.

(3) Kameoka, J.; Czaplewski, D.; Liu, H.; Craighead, H. G. *J. Mater. Chem.* **2004**, *14*, 1503-1505.

(4) McCann, J. T.; Li, D.; Xia, Y. *J. Mater. Chem.* **2005**, *15*, 735-738.

(5) Ge, J. J.; Hou, H.; Li, Q.; Graham, M. J.; Greiner, A.; Reneker, D. H.; Harris, F. W.; Cheng, S. Z. D. *J. Am. Chem. Soc.* **2004**, *126*, 15754-15761.

(6) Huang, Z.-M.; Zhang, Y.-Z.; Kotaki, M.; Ramakrishna, S. *Comp. Sci. Tech.* **2003**, *63*, 2223-2253.

(7) Xie, X.-L.; Mai, Y.-W.; Zhou, X.-P. *Mater Sci. Eng. R* **2005**, *49*, 89-112.

(8) Li, D.; Xia, Y. *Adv. Mater.* **2004**, *16*, 1151-1170.

(9) Hou, H.; Ge, J. J.; Zeng, J.; Li, Q.; Reneker, D. H.; Greiner, A.; Cheng, S. Z. D. *Chem. Mater.* **2005**, *17*, 967-973.

(10) Chronakis, I. S. *J. Mater. Proc. Tech.* **2005**, *167*, 283-293.

(11) Song, T.; Zhang, Y.; Zhou, T.; Lim, C. T.; Ramakrishna, S.; Liu, B. *Chem. Phys. Lett.* **2005**, *415*, 317-322.

(12) Song, M. Y.; Kim, D. K.; Ihn, K. J.; Jo, S. M.; Kim, D. Y. *Nanotechnology* **2004**, *15*, 1861-1865.

(13) Ye, S.; Vijh, A. K.; Dao, L. H. *J. Electrochem. Soc.* **1997**, *144*, 90-95.

(14) Cole, D. H.; Shull, K. R.; Baldo, P.; Rehn, L. *Macromolecules* **1999**, *32*, 771-779.

(15) Lee, S.; Daruka, I.; Kim, C. S.; Barabasi, A.-L.; Merz, J. L.; Furdyna, J. K. *Phys. Rev. Lett.* **1998**, *81*, 3479-3482.

(16) Guico, R. S.; Narayanan, S.; Wang, J.; Shull, K. R. *Macromolecules* **2004**, *37*, 8357-8363.

(17) Barison, S.; Fabrizio, M.; Carta, G.; Rossetto, G.; Zanella, P.; Barreca, D.; Tondello, E. *Thin Solid Films* **2002**, *405*, 81-86.

(18) Hou, H.; Reneker, D. H. *Adv. Mater.* **2004**, *16*, 69-73.

(19) Reneker, D. H.; Hou, H. *PCT Int. Appl.* **2005**, *WO 2005044723 A2*.

Chapter V: Superhydrophobic Behavior of Nanopillars and Lotus Leaf-Like Structures Made of Perfluoropolyether Derivatives

5.1 Introduction

The lotus effect,[1] a water droplet rolling down a lotus leaf while removing superficial dirt particles along its way, has captured the attention of many materials scientists recently as there are potential applications arranging from self-cleaning surfaces (building exteriors, windshields, and fabrics)[2-4] to reduced friction surfaces for microfluidic channels.[5] These phenomena derive from the lotus leaf's unusual surface topography,[1,6,7] consisting of micrometer-scale protuberances decorated with nanometer-sized hair- or flake-like fine structure in conjunction with a hydrophobic epicuticular wax layer on the leaf surface (Figure 5-1). The lotus leaf's multi-scale topographic surface exhibits superhydrophobicity—a water droplet contact angle in excess of 150˚. In addition to superhydrophobicity, low-contact-angle hysteresis[8-11] is necessary for the self-cleaning process. Dirt particles on the leaf lie on the tips of the fine protrusions which in turn, have low adhesion forces. Therefore, dirt preferentially adheres to the surface of rolling droplets and the surface self cleans.

Considerable effort has been expended on fabricating superhydrophobic and self-cleaning surfaces. According to the Cassie-Baxter equation,[12] both a rough surface and a low-surface-energy material are prerequisite for a high contact angle, so generally, most attempts to fabricate such surfaces fall into two categories.[13] One centers around methods that cover a rough surface with a low-surface-energy material; the second involves

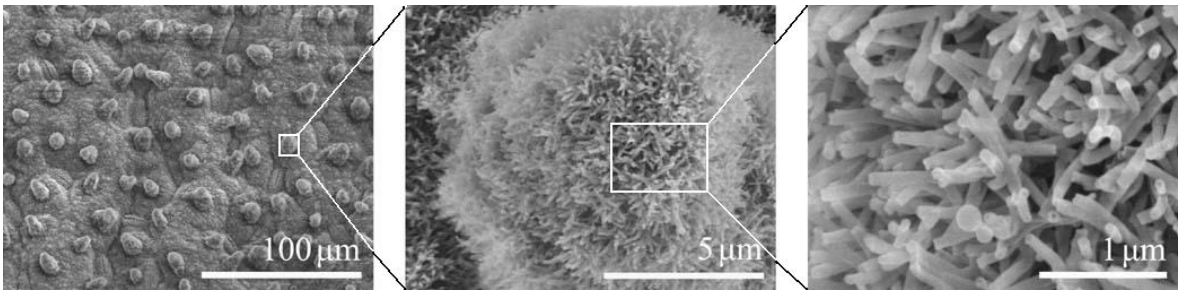

Figure 5-1. FE-SEM images of the surface structures of *Rosa Plena Lotus* leaf at different magnifications. Scale bars 100 m, 5 m, and 1 m, respectively. Note the multi-scale features ranging from ~ 10 m to ~ 100 nm, which are necessary for the superhydrophobic lotus effect.

roughening of a surface of hydrophobic material. Previous methods of generating rough surfaces include electrospinning,[14,15] template methods,[16-18] plasma, reactive ion or chemical etching,[8,11,19] chemical vapor deposition,[20-22] electro-deposition,[23,24] nanorod array growth,[25] polymer solution evaporation,[26] and textured block copolymer morphologies.[27,28] Low-surface-energy coating materials include polytetrafluoroethylene,[22] semifluorinated silanes,[29,30] fluorinated copolymers,[31] and aliphatic thiols.[23] Most of the methods disclosed to date require multi-step fabrication or surface treatments and many of the fabricated superhydrophobic surfaces are neither flexible nor translucent, which limits applications.

Recently, DeSimone and co-workers reported the fabrication of solvent-resistant photocurable perfluoropolyethers (PFPEs),[32,33] which are low-surface-tension liquids at room temperature and solidify on UV irradiation (prepolymer crosslinking). Cross-linked PFPEs exhibit low surface energy, high gas permeability, low toxicity, and extremely high chemical stability, like Teflon, which makes this material an ideal coating material.

This chapter describes the preparation of flexible, translucent superhydrophobic films made of crosslinked styrene end-functionalized perfluoropolyether (s-PFPE) and a highly fluorinated styrene sulfate ester (SS) that has a lotus leaf-like topography. The multi-scale topography on the s-PFPE-SS film is made via a simple process: UV irradiation of the prepolymer using a textured p-AAO membrane as a mold. Contact angle measurements show that the fabricated film exhibits superhydrophobic characteristics with a low contact angle hysteresis. Theoretical calculations indicate that a water droplet on the s-PFPE-SS fine structure (nanopillars) is in a Cassie state[34] — the droplet is lying on top of the lattice of nanopillars.

5.2 Materials and Instrumentation

Aluminum foils (99.99%, Alfa Aesar), phosphoric acid (86%, Fisher Scientific), ethanol (Fisher Scientific), glass slides (Gold Seal), 20 micron glass spheres (Duke Cooperation Company) were used as received, unless stated otherwise. s-PFPE and SS were synthesized by Zhilian Zhou in Professor DeSimone's group at UNC-Chapel Hill.

Morphology characterizations of the prepared samples were carried out using a FE-SEM (Hitachi S4700). A thin layer of gold (around 10 nm thick) was coated onto the surface of s-PFPE-SS samples using a sputter coater (Cressington 108 auto) to obtain high quality images. A UV chamber (ELC500 Light Exposure System, Electro Lite Corporation) was used for curing s-PFPE-SS precursors. Water contact angle measurement was done using a KSV CAM200 contact angle goniometer, and 32-bit Windows based KSV CAM software based on the true Young & Laplace equation allows extraction of the contact angles. An electronic mixer (Thermolyne 16700 Mixer) was used to provide constant shake to glass particles in ethanol. Dent structures on the surfaces of electrochemically polished aluminum foils were made using a hydraulic press (PHI melt press).

5.3 s-PFPE-SS Nanopillars

5.3.1 Experimental

P-AAO membranes with cell diameters around 400 nm were fabricated by anodization of aluminum foil in 0.3M phosphoric acid at 180V at 2˚C following the well-known two-step procedures.[35-37] Experimental details were stated in section 2.3.1.2. A range of p-AAO membranes with different pore sizes and membrane thicknesses can be achieved by controlling the anodization time. After formation, the p-AAO membranes were immersed

in 5% H_3PO_4 aqueous solution for a 40 minute post treatment at 30 ˚C for pore enlargement. Lastly, p-AAO membranes were cleaned with water and dried in air for future use.

The low modulus of the originally reported PFPE[32] (8MPa) makes it rather difficult to remove from the p-AAO mold. Typically the p-AAO has 100 nm diameter pores that are several microns in length (the thickness of the anodized layer). By using a styrene end-functionalized s-PFPE and copolymerizing it with a highly fluorinated styrene sulfate ester, the resulting cross-linked s-PFPE-SS exhibits a higher modulus (114 MPa) while maintaining all the other advantages of PFPE. The structure of s-PFPE, SS and s-PFPE-SS was shown in Figure 5-2.

s-PFPE and SS precursors were mixed with a weight ratio of 40% to 60% at 80 ˚C and cured on the surface of a p-AAO membrane using UV light under an Ar atmosphere. The prepolymer infiltrates the template and yields, after it is peeled off, a low surface energy (inverted) replica of the template membrane mold, i.e., an array of nanopilars with diameters and heights determined by the p-AAO membrane template. The surface properties of the samples were characterized by contact angle measurements.

5.3.2 Results and Discussion

5.3.2.1 s-PFPE-SS Nanopillars with an Aspect Ratio of 20

Figure 5-3A is the top-view FE-SEM image of the as-prepared p-AAO membrane which was made by anodizing aluminum foil in 0.3M H_3PO_4 aqueous solution at 2˚C for 20 minutes; the pores were enlarged in 5% H_3PO_4 aqueous solution at 30˚C for 40 minutes. The pores are approximately hexagonally close-packed with uniform diameters (~140 nm).

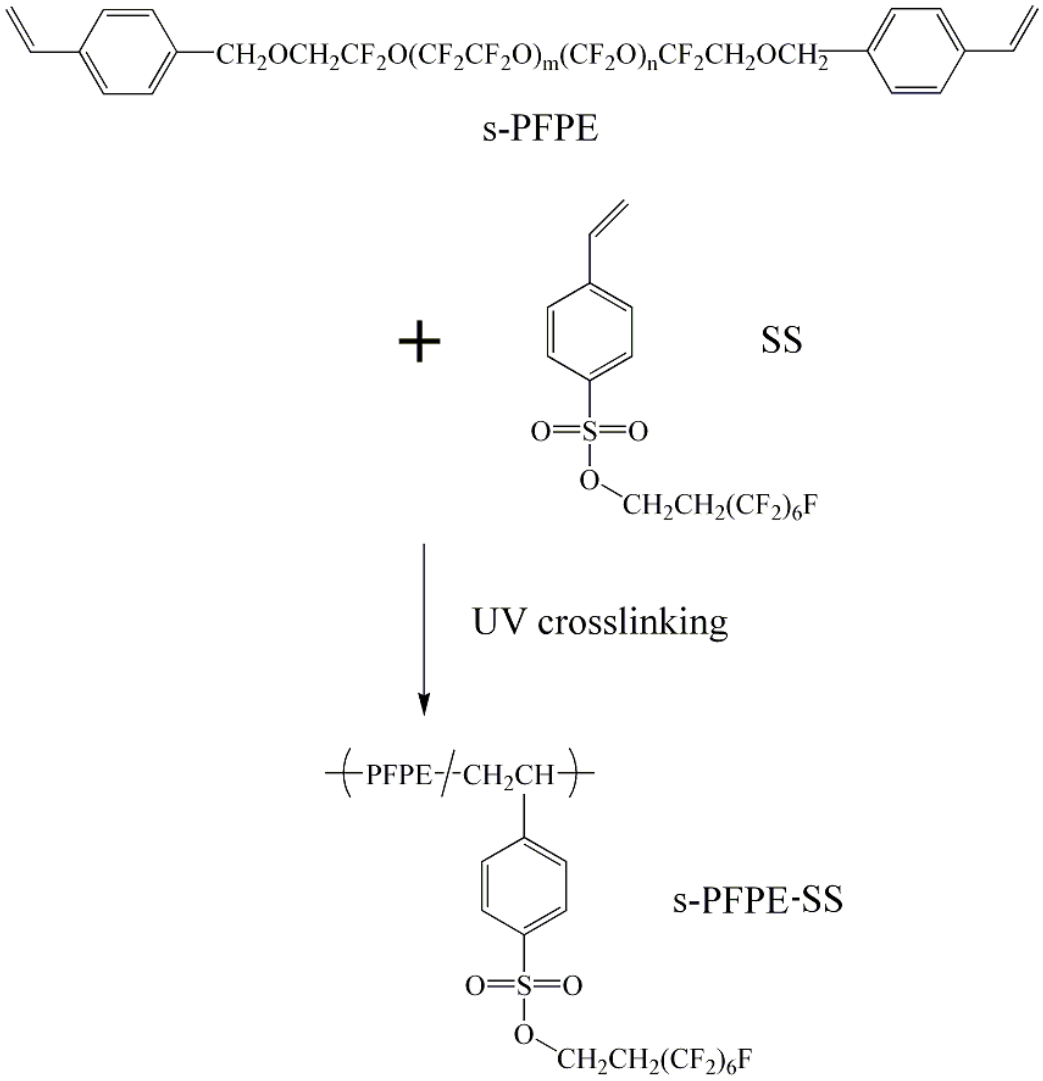

Figure 5-2. Chemical structures of s-PFPE, SS, and s-PFPE-SS.
The combination of s-PFPE and SS monomers provides a co-polymer with much higher modulus than pure s-PFPE, but with extremely low surface energy.

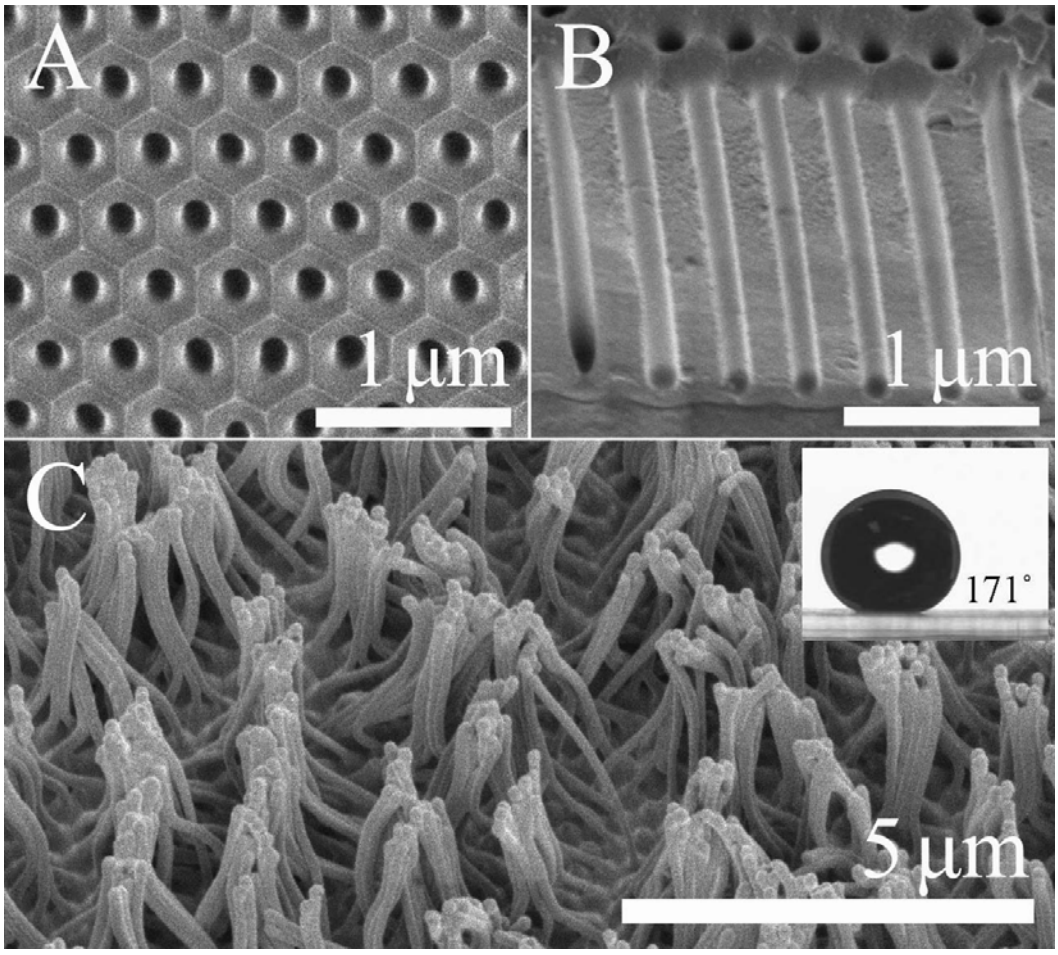

Figure 5-3. s-PFPE-SS nanopillars with an aspect ratio of 20.
A) Top view, B) 30 degree angle side view FE-SEM images of p-AAO membrane template anodized for 20 minutes at 180V. C) FE-SEM image of s-PFPE-SS nanopillar film peeled from the p-AAO membrane. The inset is a water droplet, with extremely high contact angle, sitting on the s-PFPE-SS nanopillars.

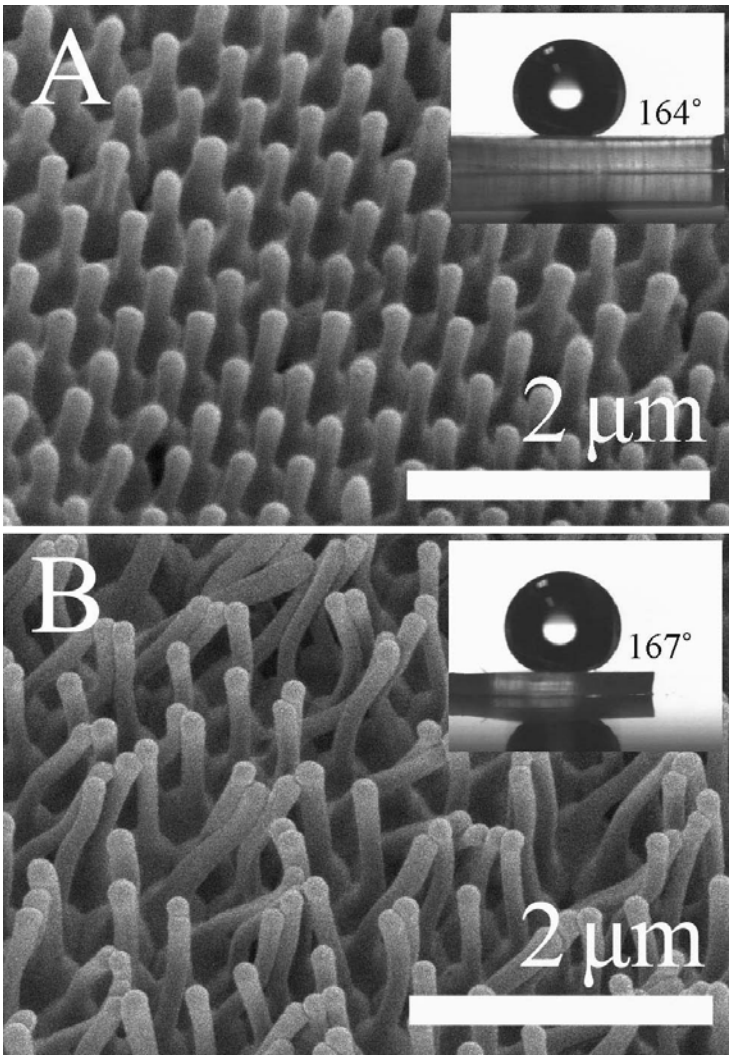

Figure 5-4. s-PFPE-SS nanopillars with an aspect ratio of 10 and 15.
FE-SEM micrographs of s-PFPE-SS nanopillar films peeled from p-AAO membranes anodized at 180V for A) 10 minutes, B) 15 minutes and pore enlarged in 5% phosphoric acid aqueous solution at 30˚C for 40 minutes. The inset in the top right corner of each image is the water droplet on the as-prepared s-PFPE-SS nanopillar film.

Figure 5-3B shows an oblique (30 degree angle) view of a cross-section of the p-AAO membrane. The pore channels are straight and parallel with a uniform diameter along the pore length; the pore bottom has a hemi-spherical shape. The length of the channels is about 3 μm. The FE-SEM image of the s-PFPE-SS nanopillars film peeled off of the p-AAO membrane is shown Figure 5-3C. The resulting s-PFPE-SS nanopillars have an aspect ratio of ~20, are uniform in length, and have diameters that match the pore diameter. Because of the high aspect ratio and flexibility of polymeric s-PFPE-SS, the nanopillars collapse into conical bundles. The inset shows a water droplet on the partially bundled s-PFPE-SS nanopillar surface. Static contact angles as high as 171˚ were observed.

5.3.2.2 s-PFPE-SS Nanopillars with an Aspect Ratio of 10 and 15

s-PFPE-SS nanopillar films with different pillar lengths were fabricated using p-AAO membranes with different thicknesses (anodization times). Figure 5-4A shows an image of s-PFPE-SS nanopillars made using a p-AAO membrane anodized for 10 minutes with further pore-enlargement for 40 minutes. The nanopillars, with lengths around 0.7 μm, are straight and parallel to each other. The tips of the nanopillars are hemispherical, which is the negative replica of the pore bottom in the p-AAO membrane. A maximum static water contact angle of 164˚ was observed (inset of Figure 5-4A). A FE-SEM image of nanopillars nearly 1.5 μm long is shown in Figure 5-4B. The template was made from a p-AAO membrane anodized for 15 minutes with pore-enlargement for 40 minutes. Some of the nanopillars are separate and some of them are aggregated into bundles; this topology is an intermediate state between that shown in Figure 5-3C and that in Figure 5-4A. The inset shows the static water contact angle (~167˚).

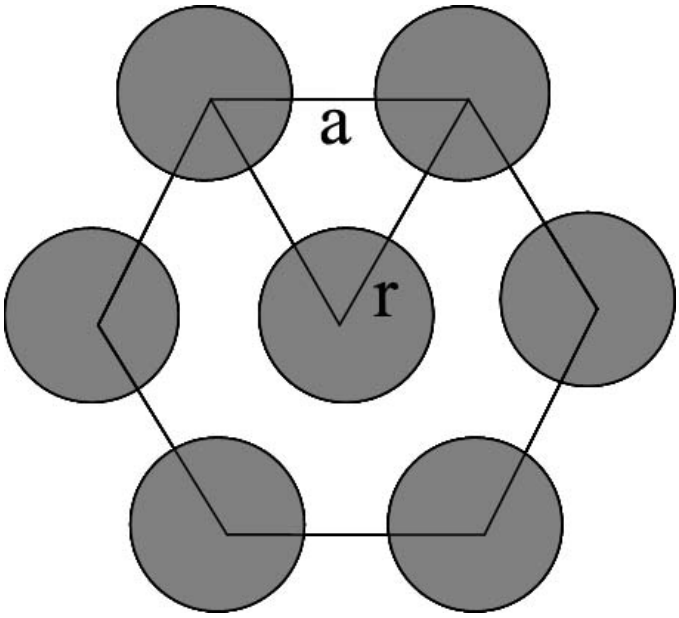

Figure 5.5. A schematic illustration of the unit cell of hexagonally close-packed s-PFPE-SS nanopillars.

5.3.2.3 The Status of Water Droplet on s-PFPE-SS Nanopillars

Although all the s-PFPE-SS nanopillar surfaces show water contact angles above 150˚, which suggests that the as-prepared surfaces possess superhydrophobicity, the status of a water droplet on s-PFPE-SS nanopillars is not clear. The Cassie-Baxter formula, which gives the apparent contact angle θ_r^c of a droplet on a rough surface (with a surface fraction ϕ_s) in the Cassie state,

$$\cos\theta_r^c = -1 + \phi_s(\cos\theta + 1) \qquad (1)$$

can give some insights into the situation. The surface fraction ϕ_s corresponds to the ratio of actual area of liquid-solid contact to the horizontal projected area of the substrate; θ is the water contact angle on a flat surface having the same chemical composition. For the surface fabricated from a p-AAO membrane anodized for 10 minutes (Figure 5-4A), the separated nanopillars are hexagonally close packed and the tips are hemispherical. A schematic illustration of the unit cell for this case is shown in Figure 5-5. If the water droplet only contacts the hemispherical tips of the nanopillars, the value of surface fraction ϕ_s can be estimated from

$$\phi_s = \frac{3 * 2\pi r^2}{6 * \frac{1}{2} * \frac{\sqrt{3}}{2} a^2} \qquad (2)$$

where r is the radius of the s-PFPE-SS nanopillars and a is inter-pillar distance. For the s-PFPE-SS nanopillars in Figure 5-4A, the radius r is ~70 nm and the interpillar distance a is ~400 nm; these parameters yield a value of 0.24 for surface fraction ϕ_s. The contact angle of water droplet on flat s-PFPE-SS surface is approximately 104˚. So the apparent angle given by Cassie-Baxter formula is θ_r^c =145˚. However the actual contact angle, 164˚,

is much larger. This result requires a much smaller surface fraction. Substituting the θ_r^c in Cassie-Baxter formula with 164˚, the required value for the surface fraction ϕ_s^* =0.052, which is 25% of surface fraction ϕ_s. Therefore, we infer that the water droplet lies on the tips of nanopillars with air trapped beneath the pillars. And moreover, the water contacts only 22% of the hemispherical surface of the nanopillars. When the nanopillars are longer and form cone-like bundles, this further reduces the contact area between the water droplet and s-PFPE-SS nanopillars. This, in turn, would further lower the surface fraction and increase the water contact angle. Therefore, the maximum static water contact angle increases as the nanopillar length increases.

5.4 Lotus Leaf-Like Structures

5.4.1 Experimental

A lotus leaf-like topography with multiple structural scales composed of the low surface energy s-PFPE-SS elastic network can be fabricated using a modest variation on the template method. The fabrication process is outlined here and in Figure 5-6. A glass slide was first immerged in 0.3 M H_2SO_4 aqueous solution at 90˚C overnight.[38,39] The treated glass was cleaned using distilled water and dried with compressed air. An appropriate amount of 20 micron glass spheres (Duke Cooperation Company) were dispersed in ethanol and the suspension was placed onto the surface of glass slide. Under a delicate process of vibration with solvent evaporation, a monolayer of glass spheres is obtained on the surface of glass slide. By pressing the monolayer of spheres on glass into the aluminum foil using a hydraulic press[40] (PHI melt press) under a pressure of approximate 3200 kg cm^{-2}, an array of concave features—the negative replica of the close-packed glass spheres—was embossed into the

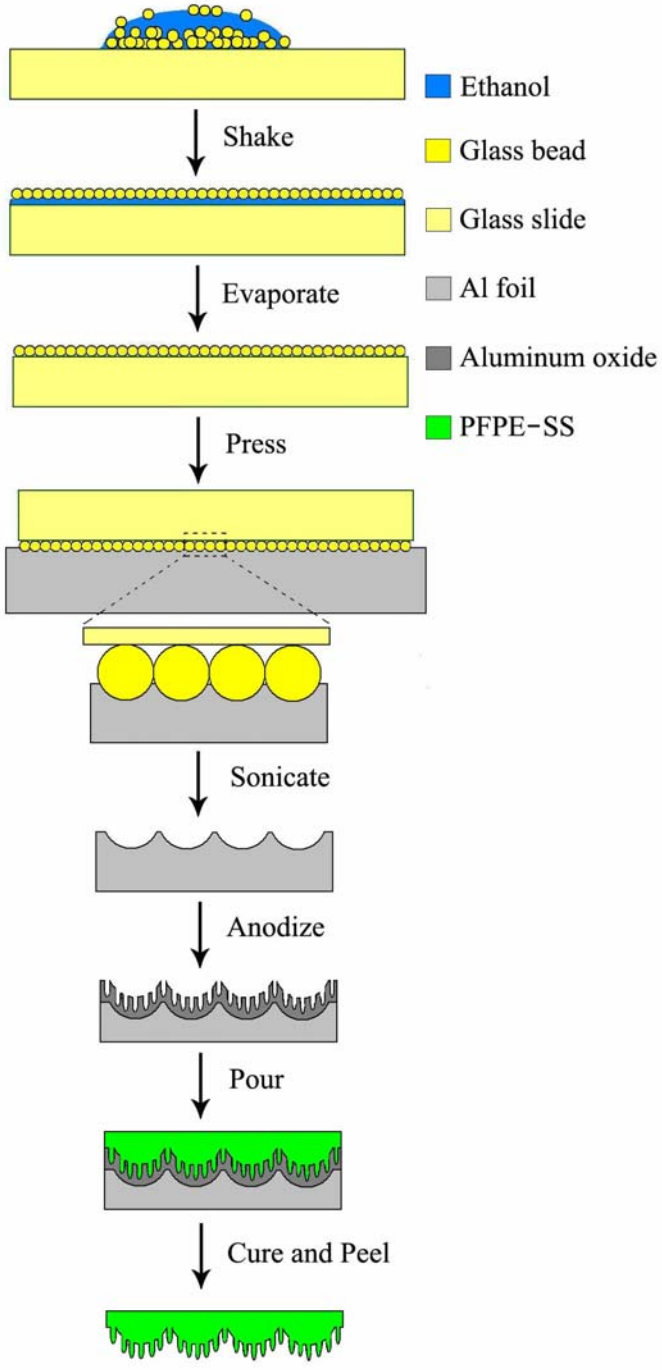

Figure 5-6. A schematic illustration of the procedure for the fabrication of a lotus leaf-like s-PFPE-SS structure.

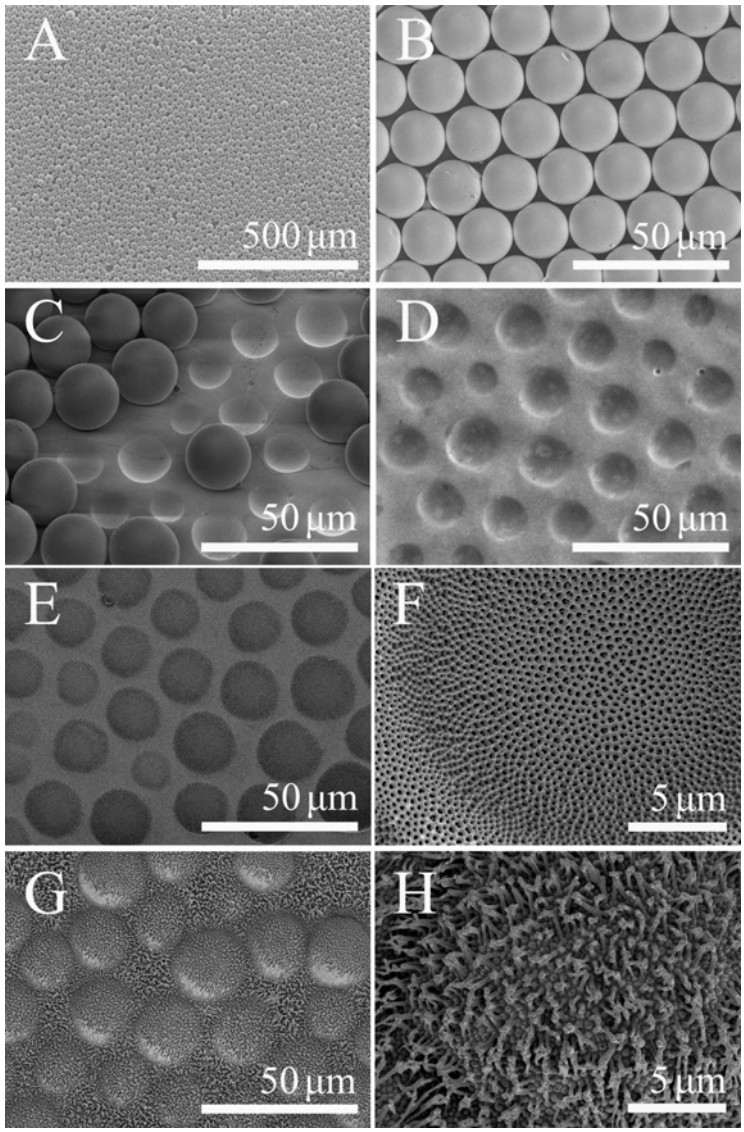

Figure 5-7. FE-SEM micrographs of s-PFPE-SS lotus leaf-like structures.
FE-SEM micrographs of (A), (B) glass sphere monolayer at different magnification, (C) dimpled aluminum foil after press the glass spheres into the aluminum, (D) dimpled aluminum foil after sonication, (E),(F) honeycomb like p-AAO membrane at different magnifications and (G),(H) lotus leaf-like s-PFPE-SS molded replica at different magnifications.

surface of aluminum. The glass spheres can be removed from the dimpled aluminum surface by sonication. Following the same anodization procedure, the dimpled aluminum develops a honeycomb of porous channels in the conformal p-AAO membrane; the hexagonal pores are

normal to the hemispherical dimples. Similar to the conventional flat p-AAO template method, the liquid mixture of s-PFPE and SS precursors was added to the patterned porous surface of the membrane and cured under an Ar atmosphere with UV irradiation. Afterwards, the cross-linked s-PFPE-SS film was peeled off of the textured p-AAO template and contact angles were measured.

5.4.2 Results and Discussion

The FE-SEM micrographs associated with the different fabrication steps of the multi-scale, lotus leaf-like s-PFPE-SS structure are shown in Figure 5-7. Figure 5-7A shows a FE-SEM image of a monolayer of glass spheres on a glass slide. A uniform area around 1 cm^2 could be readily obtained; Figure 5-7B is a magnified image of the ~20 micron glass sphere monolayer. It indicates that the glass spheres are approximately hexagonally close-packed. Figure 5-7C shows the dimpled aluminum foil after pressing the glass sphere monolayer into the aluminum. After the pressing stage most of the glass spheres remain in embedded in the aluminum foil. Figure 5-7D shows the FE-SEM micrograph of dimpled aluminum foil after sonication; all the glass spheres are removed from the aluminum foil surface and the concave dimples are apparent. Figure 5-7E shows the FE-SEM image of the honeycomb of pores in the p-AAO membrane (anodized in 0.3M H_3PO_4 aqueous solution at 180V for 20 minutes at 2˚C; after the two-step anodization, pore enlargement was conducted in 5% H_3PO_4 aqueous solution for 40 minutes at 30˚C). Figure 5-7F is a FE-SEM micrograph of the membrane at a larger magnification. Since the aluminum foil retains the micron-scale dimples after the two step anodization, the dimpled structure on the aluminum foil surface does not appear to affect the anodization: the pores are normal to the surface, parallel and straight. This also explains

why the pore openings at the bottom of the concave dimples appear larger than the fore-shortened openings on those oblique surfaces in the top view FE-SEM image. Figure 5-7 parts F and H show the corresponding FE-SEM images of the lotus leaf-like s-PFPE-SS structure that is peeled from the porous, dimpled p-AAO membrane. These images clearly show that 20 micron hemispherical "dimples" populating the s-PFPE-SS are punctuated by hundred nanometer s-PFPE-SS pillars. This topography has two distinct spatial scales and mimics the lotus leaf surface. It yields a maximum static contact angle of 169˚.

5.5 Dynamic Contact Angle Study

Recent studies have suggested that the static contact angle does not reflect the ability of water drops to stick to a substrate[10] and does not adequately describe the hydrophobicity of a surface.[9] In addition to a large contact angle, a low contact angle hysteresis is thought to play an important role in the self-cleaning phenomenon. Contact angle hysteresis is the difference between the advancing and receding contact angle values. Advancing and receding contact angle measurements were performed as the following; drops exhibit an advancing edge by addition of liquid into the drop on a surface with a micro syringe, and a receding edge on withdrawing liquid from the drop. Water contact angles of the flat s-PFPE-SS surface, the s-PFPE-SS nanopillars on a flat surface from a p-AAO membrane template anodized for 20 minutes (Figure 5-3C), and the lotus leaf-like s-PFPE-SS topography (Figure 5-7G) are shown in Table 5-1. Both the s-PFPE-SS nanopillars on a flat surface and the lotus

Table 5-1. Dynamic and static contact angles measured different s-PFPE-SS structures. Dynamic and static contact angles measured on a flat s-PFPE-SS surface, s-PFPE-SS nanopillars fabricated using a flat p-AAO membrane anodized for 20 minutes (Figure 5-3C) and the lotus leaf-like s-PFPE-SS structure (Figure 5-7G). Tilt angles at which water droplet begins to roll are also listed.

	Advancing contact angle (˚)	Receding contact angle (˚)	Static contact angle (˚)	Tilt angle at which water droplet begins rolling down(˚)
s-PFPE-SS Flat surface	107	73	104	
s-PFPE-SS nanopillars (Figure 5-3C)	173	162	171	3
lotus leaf-like s-PFPE-SS structure (Figure 5-7G)	170	160	169	3

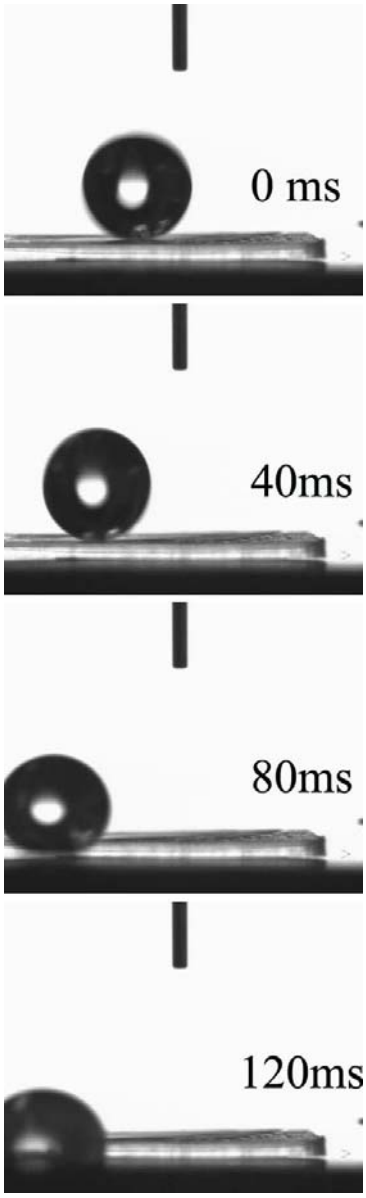

Figure 5-8. Motion of a water droplet on a flat s-PFPE-SS film punctuated with nanopillars (Figure 5-3C) (p-AAO membrane anodized for 20 minutes at 180V).

leaf-like topography show a small contact angle hysteresis (~10˚), which is much less than that of a smooth (untextured) s-PFPE-SS surface. The underlying reason is that the hair-like nanopillars present a discontinuous contact line with the water droplet, decreasing friction and lowering the energy barrier for the advancing and receding drop.[8,9]

When the flat surface comprised of s-PFPE-SS nanopillars was tilted to ~3˚ relative to horizontal, a 5 mg water droplet began rolling because of gravity. The lotus leaf-structured surface also requires a tilt angle of ~3˚ for the water droplet to move. This suggests that the adhesion force between the water drop and the multi-scale structured s-PFPE-SS surface is small.

5.6 Dynamic Behaviors of Water Droplets on Structured s-PFPE-SS Surfaces

In addition to the static and dynamic contact angle measurements, the dynamic behavior of water on a flat s-PFPE-SS film punctuated with nanopillars was studied. The dynamics of a water droplet falling onto the surface mimics rain falling onto a lotus leaf. The images shown in Figure 5-8 were taken with a digital CCN fire-wire camera at a rate of 25 frames per second on the CAM 200 contact angle goniometer. A microsyringe attached to a needle with an inner diameter of 0.15mm and an outer diameter of 0.30 mm was employed to form a water droplet. The tip of the needle was 3.4mm away from the surface of s-PFPE-SS nanopillars, which in turn was tilted approximately 0.5˚ relative to the horizontal. A water droplet with a 2.2 mm diameter detached from the needle, hit the s-PFPE-SS nanopillars surface and rolled on the s-PFPE-SS nanopillar surface to the working stage with no hesitation. Fine fibrous debris on the s-PFPE-SS nanopillared flat surface and the multi-scale

lotus leaf-like topography could be removed by the moving water droplet. These observations are reminiscent of the water repellant lotus leaf and its self-cleaning property.

5.7 s-PFPE Nanopillars

s-PFPE nanopillars were also prepared using p-AAO membrane templates. However, since the modulus of s-PFPE (2 MPa) is much lower than that of s-PFPE-SS, s-PFPE nanopillars film could not be peeled off from the p-AAO membrane if the nanochannels were too deep (approximate one micron). The experimental procedure is the same as that for s-PFPE-SS nanopillars, with s-PFPE-SS precursor substituted by s-PFPE precursor. The p-AAO membrane was anodized at 180V for 10 minutes. s-PFPE cured in p-AAO membranes with deeper nanochannels could not be peeled off from the template.

Figure 5-9 shows the FE-SEM images of the p-AAO membrane and the peeled s-PFPE pillars. Surprisingly, the diameter of pillars is around 260 nm, which is much larger than the diameter of p-AAO channels (140nm). The expansion of nanopillars may be induced from the stress stored between the polymer chains during curing.

Motions of the polymer chains in the nanochannels are restricted due to the interaction between the channel walls and the s-PFPE precursor. During the crosslinking process, this restriction would greatly limit the rearrangement of polymer chains, and stress is produced among the polymer networks. After s-PFPE nanopillars are peeled off from the template, the restriction disappears and the stress is dissipated. Since s-PFPE is an elastomer, the diameter of pillars expands. The aspect ratio of the prepared s-PFPE nanopillars is around 3. The largest static contact angle obtained from the surface of s-PFPE nanopillars film is 159˚.

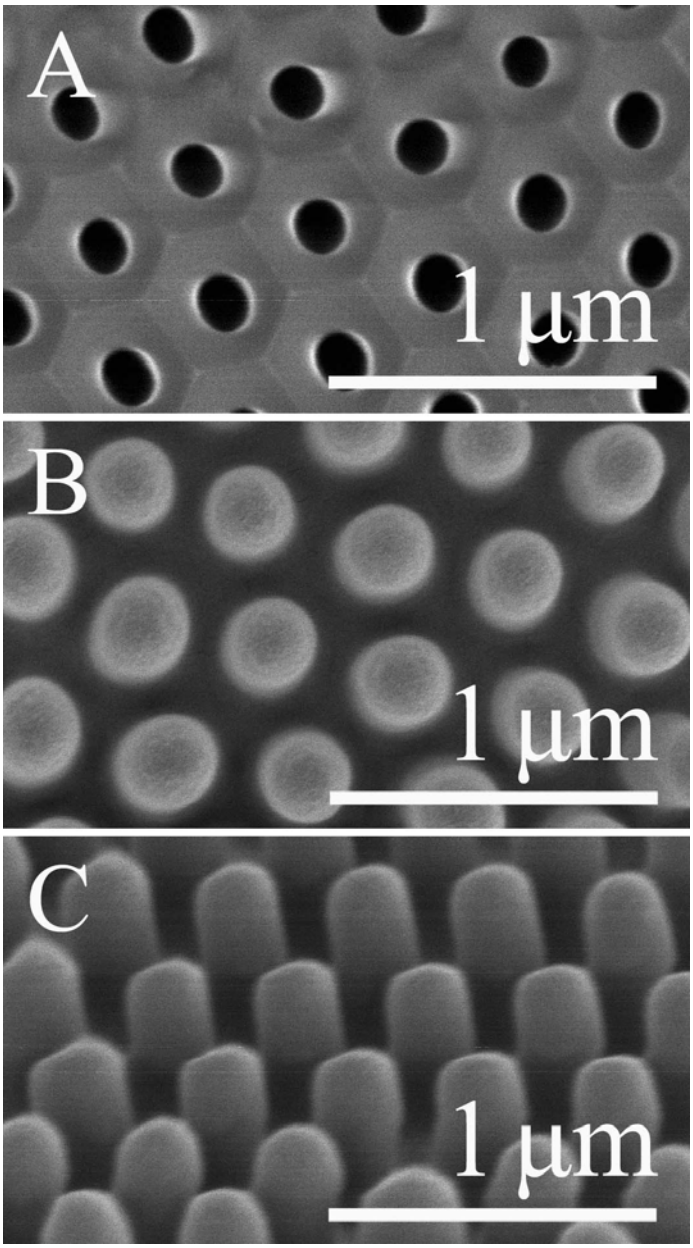

Figure 5-9. FE-SEM micrographs of s-PFPE nanopillars.
FE-SEM micrographs of (A) a p-AAO membrane anodized at 180V for 10 minutes, (B) top, and (C) side views of s-PFPE nanopillar films peeled from the p-AAO membrane.

5.8 Concluding Remarks

In conclusion, patterned p-AAO membranes fabricated using the two step aluminum anodization process yields superhydrophobic films punctuated with s-PFPE-SS nanopillars having controllable aspect ratios. A s-PFPE-SS topography that mimics the multi-scale roughness of a lotus leaf surface was obtained by a simple UV-induced crosslinking reaction of a low surface energy prepolymer on a p-AAO template. The s-PFPE-SS nanopillars with lengths of ~3 μm and with two spatial scale structures—micro dimples and punctuated with nanopillars, lotus leaf-like topography—show low contact angle hysteresis and self cleaning.

5.9 References

(1) Barthlott, W.; Neinhuis, C. *Planta* **1997**, *202*, 1-8.

(2) Callies, M.; Quere, D. *Soft Matter* **2005**, *1*, 55-61.

(3) Quere, D. *Nature Mater.* **2002**, *1*, 14-15.

(4) Nakajima, A.; Hashimoto, K.; Watanabe, T. *Monatshefte fur Chemie* **2001**, *132*, 31-41.

(5) Choi, C.-H.; Kim, C.-J. *Phys. Rev. Lett.* **2006**, *96*, 066001.

(6) Furstner, R.; Barthlott, W.; Neinhuis, C.; Walzel, P. *Langmuir* **2005**, *21*, 956-961.

(7) Cheng, Y.-T.; Rodak, D. E. *Appl. Phys. Lett.* **2005**, *86*, 144101.

(8) Oner, D.; McCarthy, T. J. *Langmuir* **2000**, *16*, 7777-7782.

(9) Chen, W.; Fadeev, A. Y.; Hsieh, M. C.; Oner, D.; Youngblood, J.; McCarthy, T. J. *Langmuir* **1999**, *15*, 3395-3399.

(10) Quere, D.; Lafuma, A.; Bico, J. *Nanotechnology* **2003**, *14*, 1109-1112.

(11) Krupenkin, T. N.; Taylor, J. A.; Schneider, T. M.; Yang, S. *Langmuir* **2004**, *20*, 3824-3827.

(12) Cassie, A. B. D.; Baxter, S. *Trans. Faraday Soc.* **1944**, *40*, 546-551.

(13) Feng, L.; Li, S.; Li, Y.; Li, H.; Zhang, L.; Zhai, J.; Song, Y.; Liu, B.; Jiang, L.; Zhu, D. *Adv. Mater.* **2002**, *14*, 1857-1860.

(14) Ma, M.; Hill, R. M.; Lowery, J. L.; Fridrikh, S. V.; Rutledge, G. C. *Langmuir* **2005**, *21*, 5549-5554.

(15) Jiang, L.; Zhao, Y.; Zhai, J. *Angew. Chem. Int. Ed.* **2004**, *43*, 4338-4341.

(16) Feng, L.; Li, S.; Li, H.; Zhai, J.; Song, Y.; Jiang, L.; Zhu, D. *Angew. Chem. Int. Ed.* **2002**, *41*, 1221-1223.

(17) Jin, M.; Feng, X.; Feng, L.; Sun, T.; Zhai, J.; Li, T.; Jiang, L. *Adv. Mater.* **2005**, *17*, 1977-1981.

(18) Feng, L.; Song, Y.; Zhai, J.; Liu, B.; Xu, J.; Jiang, L.; Zhu, D. *Angew. Chem. Int. Ed.* **2003**, *42*, 800-802.

(19) Youngblood, J. P.; McCarthy, T. J. *Macromolecules* **1999**, *32*, 6800-6806.

(20) Li, H.; Wang, X.; Song, Y.; Liu, Y.; Li, Q.; Jiang, L.; Zhu, D. *Angew. Chem. Int. Ed.* **2001**, *40*, 1743-1746.

(21) Li, S.; Li, H.; Wang, X.; Song, Y.; Liu, Y.; Jiang, L.; Zhu, D. *J. Phys. Chem. B* **2002**, *106*, 9274-9276.

(22) Lau, K. K. S.; Bico, J.; Teo, K. B. K.; Chhowalla, M.; Amaratunga, G. A. J.; Milne, W. I.; McKinley, G. H.; Gleason, K. K. *Nano Lett.* **2003**, *3*, 1701-1705.

(23) Jiang, Y.; Wang, Z.; Yu, X.; Shi, F.; Xu, H.; Zhang, X. *Langmuir* **2005**, *21*, 1986-1990.

(24) Zhao, N.; Shi, F.; Wang, Z.; Zhang, X. *Langmuir* **2005**, *21*, 4713-4716.

(25) Feng, X.; Feng, L.; Jin, M.; Zhai, J.; Jiang, L.; Zhu, D. *J. Am. Chem. Soc.* **2004**, *126*, 62-63.

(26) Erbil, H. Y.; Demirel, A. L.; Avci, Y.; Mert, O. *Science* **2003**, *299*, 1377-1380.

(27) Han, J. T.; Xu, X.; Cho, K. *Langmuir* **2005**, *21*, 6662-6665.

(28) Minko, S.; Muller, M.; Motornov, M.; Nitschke, M.; Grundke, K.; Stamm, M. *J. Am. Chem. Soc.* **2003**, *125*, 3896-3900.

(29) Zhai, L.; Cebeci, F. C.; Cohen, R. E.; Rubner, M. F. *Nano Lett.* **2004**, *4*, 1349-1353.

(30) Miwa, M.; Nakajima, A.; Fujishima, A.; Hashimoto, K.; Watanabe, T. *Langmuir* **2000**, *16*, 5754-5760.

(31) Yabu, H.; Takebayashi, M.; Tanaka, M.; Shimomura, M. *Langmuir* **2005**, *21*, 3235-3237.

(32) Rolland, J. P.; Van Dam, R. M.; Schorzman, D. A.; Quake, S. R.; DeSimone, J. M. *J. Am. Chem. Soc.* **2004**, *126*, 2322-2323.

(33) Wood, C. D.; Michel, U.; Rolland, J. P.; DeSimone, J. M. *J. Fluorine Chem.* **2004**, *125*, 1671-1676.

(34) Patankar, N. A. *Langmuir* **2004**, *20*, 7097-7102.

(35) Masuda, H.; Fukuda, K. *Science* **1995**, *268*, 1466-1468.

(36) Masuda, H.; Yada, K.; Osaka, A. *Jpn. J. Appl. Phys.* **1998**, *37*, L1340-L1342.

(37) Li, A. P.; Muller, F.; Bimer, A.; Nielsch, K.; Gosele, U. *J. Appl. Phys.* **1998**, *84*, 6023-6026.

(38) Micheletto, R.; Fukuda, H.; Ohtsu, M. *Langmuir* **1995**, *11*, 3333-3336.

(39) Yan, X.; Yao, J.; Lu, G.; Li, X.; Zhang, J.; Han, K.; Yang, B. *J. Am. Chem. Soc.* **2005**, 7688-7689.

(40) Asoh, H.; Nishio, K.; Nakao, M.; Tamamura, T.; Masuda, H. *J Electrochem. Soc.* **2001**, *148*, B152-B156.

Chapter VI: Future Directions

6.1 Preparation of a Solar Cell with Silver Nanorod Array Electrodes

Silver nanorod arrays standing on an aluminum substrate were fabricated by electrodeposition on a treated porous anodic aluminum oxide (p-AAO) membrane template (Chapter 1). As reported by Dr. Chu, a p-AAO membrane on indium doped tin oxide (ITO) glass was fabricated by anodizing an aluminum film deposited on ITO glass.[1] Therefore, silver nanorod arrays standing on the surface of ITO glass can be fabricated using electrodeposition following the same procedure stated in Chapter 1. The gaps between silver nanorods can be filled with titanium oxide using a sol-gel method.[1-3] This fabricated nanostructure may find application in solar cells. As shown in Figure 6-1, this is an ideal back contact electrode for dye-sensitized solar cells. The produced electrons on titanium oxide powders can travel to the ITO glass through the silver nanorods instead of hopping through the titanium powder. The transfer of electrons would be much faster, which can greatly reduce the efficiency-reducing leak reaction, i.e., the conducting electrons react with molecules in solution during transport in the semiconductor layer before reaching the back contact electrode.[4]

6.2 Optimization of Membrane Electrode Assembly Preparation for Polymer Electrolyte Membrane Fuel Cells

Polymer electrolyte membrane fuel cells (PEMFCs) are complex systems. The performance of a fuel cell depends on not only the property of materials but also the

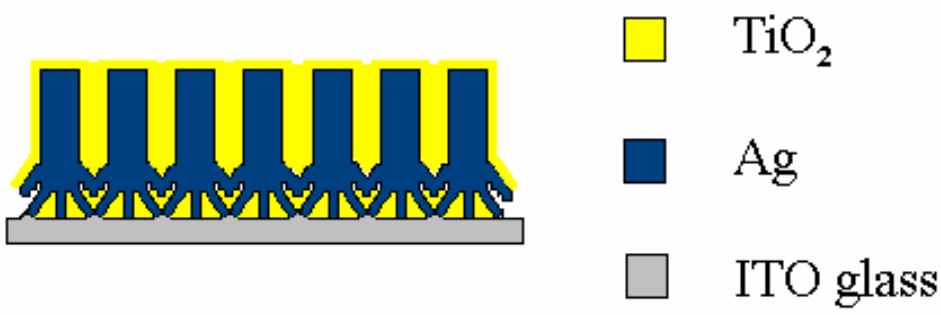

Figure 6-1. Schematic diagram of silver nanorods arrays standing on an ITO glass slide with the gaps between nanorods filled with titanium oxide.

engineering techniques used to construct the cells. The catalyst ink is generally composed of catalyst (a powder of Pt dispersed on carbon) and a Nafion ionomer alcohol solution. Once the ink is prepared, it is applied to the Nafion film in a number of different ways. The oxidation of hydrogen and reduction of oxygen is localized at the three-phase boundary among gases, proton conductive Nafion membrane and carbon-supported platinum catalyst. Addition of proton conductive Nafion ionomer to the electrode extends the reactive layer, and improves the utilization of catalyst and the interfacial contact with the Nafion membrane. However, too much Nafion ionomer may block the interconnection of catalyst powders and reduce the catalyst efficiency. Thus, one must use an optimal loading of Nafion ionomer in the reactive layer, generally around 0.6-1.0 mg/cm^2. [5]

The structure of the prepared catalyst (platinum nanoparticles embedded in carbon nanofibers) using template method (Chapter 3) is very different from the general reported catalyst (platinum nanoparticles supported on the surface of carbon powders). Although the prepared catalyst possesses excellent catalytic activity, the preparation of catalyst ink and the construction of a membrane electrode assembly (MEA) needs to be optimized to get good fuel cell performances.

The optimal composition of electrode (i.e., mass ratio of prepared catalyst to Nafion ionomer) can be determined by testing the fuel cell performance with different Nafion loadings. The method of MEA preparation also requires studying. Hot-pressing after catalyst ink painting on Nafion film may be needed to provide a better interfacial contact between electrode and membrane. At last, the fuel cell operation conditions need optimization to provide a good fuel flow and water control.

6.3 Optimization of the Preparation of Platinum-Nanoparticle-Embedded Carbon Fibers Using Electrospinning

Platinum-nanoparticle-embedded carbon fibers (Pt-CFs) prepared from electrospinning can be directly applied to PEMFCs (Chapter 4). This electrospinning method is simple and high-yield relative to the template-based method. However, the Pt nanoparticles are covered by carbon matrix and are not accessible to fuel gas. The carbon matrix needs to be porous to expose the platinum nanoparticles.

There are two possible methods to overcome this problem. One is post treatment. Nanopores can be produced in carbon fibers by reaction with water vapor at high temperature.[6] The other method is making copolymer fibers. Solutions of platinum salt, polyacrylonitrile (PAN) and a second polymer dissolved in DMF can be prepared for electrospinning. The second polymer in electrospun fibers can either be chemically etched before pyrolysis or be burned out at high temperature to make a porous fiber structure.

6.4 Preparation of a Platinum Alloy Catalyst for Direct Methanol Fuel Cells

6.4.1 Direct Methanol Fuel Cells

A direct methanol fuel cell (DMFC) is similar to a PEMFC except using methanol as fuel at the anode instead of hydrogen. Just as in PEMFCs, a DMFC is composed of a polymer electrolyte membrane (usually Nafion), electrodes (usually Pt or Pt alloy), back layers and current collector layers. Electrochemical reactions occur in a DMFC. Methanol is oxidized to CO_2 via reaction with H_2O at the anode (1). For each CH_3OH molecule, 6 electrons and 6 protons are formed. Electrons travel through the outer circuit and protons travel through the internal polymer electrolyte membrane. At the cathode, they react with O_2

and create H_2O (2).

Anode: $CH_3OH + H_2O \rightarrow CO_2 + 6H^+ + 6e^-$ (1)

Cathode: $3/2O_2 + 6H^+ + 6e^- \rightarrow 6H_2O$ (2)

Cell reaction: $CH_3OH + 3/2O_2 \rightarrow CO_2 + 2H_2O$ (3)

The advantage of DMFCs lie in that storage of methanol is similar to ordinary fuel storage, while hydrogen storage requires a bulky and heavy system and is a very challenging issue. It is also necessary to point out that since methanol is one of the smallest organic molecules, DMFCs could be regarded as the bridge from PEMFCs to more complicated hydrocarbon (e.g. ethanol) fuel cell in the future. This makes DMFCs very special. However, DMFCs have their own shortcomings. The first problem lies in methanol crossover, which lowers the fuel cell efficiency. The crossover problem can be overcome by changing the polymer electrolyte membrane chemistry. The second one is the involvement of water at the anode, which requires design consideration in the fuel cell (especially the backing layer). The third one, maybe the most important of all, is the oxidation of methanol, which is more complicated and difficult than that of hydrogen. The reversible potential for methanol oxidation is 0.04V (1), but methanol presents a relatively high overpotential on a Pt electrode.[7]

To obtain high fuel cell output voltage, the oxidation of methanol occurring at relative low voltage is required. The polymer electrolyte membrane in a DMFC is proton conductive only when it is water saturated. So both cathode and anode electrochemical reactions need to happen below the boiling temperature of water. The oxidation of methanol is much more difficult than oxidation of hydrogen. To oxidize methanol at low temperature, powerful catalysts are needed. Pt or Pt-based catalysts (e.g. Pt-Ru, Pt-W) are the only effective

catalysts found to date.

6.4.2 Mechanism of Methanol Oxidization

Although the mechanism of methanol oxidation on Pt is still under discussion, it is generally believed to be the following.[7-9]

$$CH_3OH \rightarrow CH_2OH + H^+ + e^- \quad (4)$$

$$Pt\text{-}CH_2OH \rightarrow Pt_2\text{-}CHOH + H^+ + e^- \quad (5)$$

$$Pt_2\text{-}CHOH \rightarrow Pt_3\text{-}COH + H^+ + e^- \quad (6)$$

$$3Pt + 3H2O \rightarrow 3Pt\text{-}OH + 3H^+ + e^- \quad (7)$$

$$Pt_3\text{-}COH + Pt\text{-}OH \rightarrow Pt_2\text{-}CO + H_2O \quad (8)$$

$$Pt_2\text{-}CO + Pt\text{-}OH \rightarrow Pt\text{-}COOH \quad (9)$$

$$Pt\text{-}COOH + Pt\text{-}OH \rightarrow CO_2 + H_2O \quad (10)$$

Methanol is adsorbed onto the platinum catalyst first, and it releases H^+ and e^- easily (step 4-6). To let the oxidation proceed, three adjacent Pt sites are needed for each methanol molecule.[7] However, the dehydrogenation stops at some point and the composition of methanolic residue is still under debate. Different compositions, such as CO, COH, CHO, and HCOOH have been suggested. The following oxidations (step 8-10) happen at a much higher potential via reaction with adsorbed water. CO_2 forms as the final product.

Step 7 is supposed to be the rate determining step. Water is the oxygen donor for oxidation of methanol. Without adsorbed water, no further reaction would happen. However, on the other side, the absorption of water is also competing with adsorption of methanol. So water has a two-way effect.[8] While the decomposition of water on Pt requires high voltage, Ru splits water at low potentials.[10]

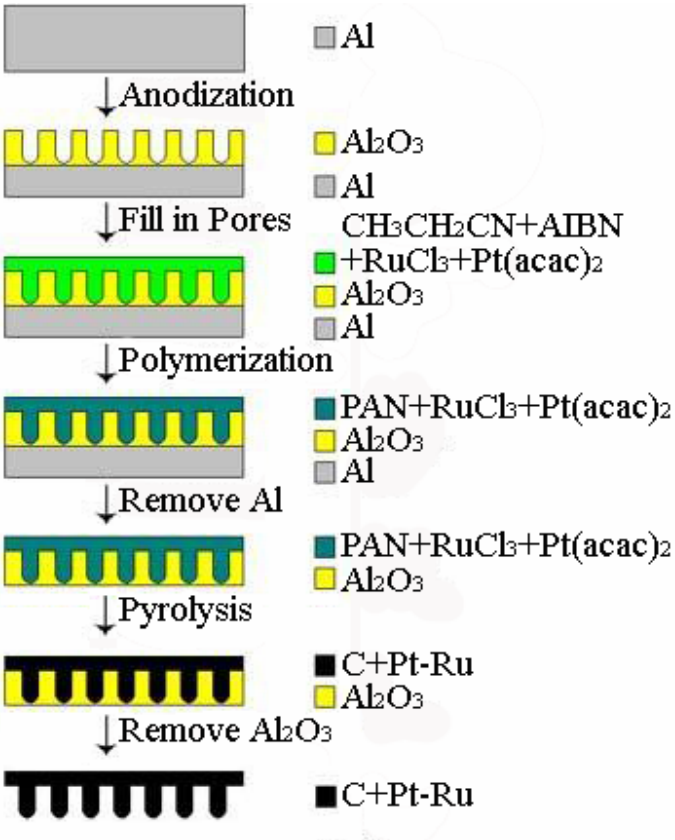

Figure 6-2. Schematic diagram of the fabrication of Pt-Ru alloy nanoparticles embedded in carbon nanofibers using a p-AAO membrane template.

6.4.3 Platinum Alloy Catalyst

The adsorption and catalytic activity of Pt are modified via the incorporation of a second metal. Better electrocatalytic activity for the oxidation of methanol can be achieved by using binary catalysts or ternary catalysts. Many experiments are conducted and Pt-Ru, Pt-W, Pt-Sn are found to enhance the activity for methanol oxidation.[7]

$$Ru\text{-}H_2O \rightarrow Ru\text{-}OH + H^+ + e^- \quad (11)$$

$$Pt\text{-}CO + Ru\text{-}OH \rightarrow Pt + Ru + CO_2 + H^+ + e^- \quad (12)$$

Besides the lower water splitting potential (11), the better resistance to CO poisoning (12) is assumed to be the key factor. Several fabrication methods for binary catalysts are suggested. For example, H. Hoster et al. obtained Ru clusters on a Pt surface by evaporation of Ru under ultra high vacuum.[10] E.V. Spinace et al. reported spontaneous deposition of platinum on Ru nanoparticles.[11] Pt-Ru ally could also be fabricated through spontaneous deposition out of Pt ion and Ru ion solutions.[12]

6.4.4 Future Directions for the Fabrication of Platinum Alloys

DMFCs are one of the most promising technologies that adopt methanol as fuel. The oxidation of methanol is the most important and crucial issue in DMFCs. Although the mechanism of electrocatalysis of methanol oxidation is still under discussion, it is generally believe that the oxidation proceeds via reaction with adsorbed water. Binary or ternary catalysts show better electrocatalytic activity than Pt due to their lower water splitting potentials and higher resistance to CO poisoning. Improving the catalytic activity of Pt-based catalysts or searching for less expensive catalysts would be the main research subject in methanol-oxidation field in the future.

Highly dispersed Pt nanoparticles in carbon nanofibers (Pt-CNFs) were fabricated using the template-based method (Chapter 3). It is possible to add another appropriate Ru salt [e.g. $Ru(acac)_3$ or $RuCl_3$] to the initial solution (acrylonitrile, AIBN and Platinum salt). The Pt-Ru alloy catalyst should be formed during the pyrolysis of PAN nanofibers by following the same procedure stated in Chapter 3 (Figure 6-2).

Although Pt-Sn is seldom seen, it is reported to be one of the best catalysts.[7] To obtain a Pt-Sn binary catalyst, using crystalline SnO_2[13] nanoparticles may be a possible route. Pt can be electrodeposited onto SnO_2 nanoparticles, then SnO_2 can be reduced to Sn and form Pt-Sn alloy.

6.5 Concluding Remarks

This thesis presents a comprehensive array of techniques for fabrication of nanoscale materials applicable to advanced solar cells, fuel cells, and self-cleaning surface. Some viable future directions forms the basis of this chapter, and hopefully will spur further research using these techniques to build devices with higher efficiency and increased functionality.

6.6 References

(1) Chu, S.-Z.; Wada, K.; Inoue, S.; Todoroki, S.-I. *Chem. Mater.* **2002**, *14*, 266-272.

(2) Chu, S.-Z.; Wada, K.; Inoue, S. *Adv. Mater.* **2002**, *14*, 1752-1756.

(3) Chu, S. Z.; Wada, K.; Inoue, S.; Todoroki, S. *Surface and Coatings Technology* **2003**, *169-170*, 190-194.

(4) Katoh, R.; Furube, A.; Yoshihara, T.; Hara, K.; Fujihashi, G.; Takano, S.; Murata, S.; Arakawa, H.; Tachiya, M. *J. Phys. Chem. B* **2004**, *108*, 4818-4822.

(5) Antolini, E. *J. Appl. Electrochem.* **2004**, *34*, 563-576.

(6) Chun, I.; Reneker, D.; Fong, H. *J. Adv. Mater.* **1999**, *31*, 36-41.

(7) McNicol, B. D.; Rand, D. A. J.; Williams, K. R. *J. Power Sources* **1999**, *83*, 15-31.

(8) Iwasita, T. *J. Braz. Chem. Soc.* **2002**, *13*, 401-409.

(9) Jung, I.; Kim, D.; Yun, Y.; Chung, S.; Lee, J.; Tak, Y. *Electrochimica Acta* **2004**, *50*, 607-610.

(10) Hoster, H.; Iwasita, T.; Baumgartner, H.; W. Vielstich. *J. Electrochem Soc.* **2001**, *148*, A496-A501.

(11) Spinace, E. V.; Neto, A. O.; Linardi, M. *J. Power Sources* **2004**, *129*, 121-126.

(12) He, Z.; Chen, J.; Liu, D.; Tang, H.; Deng, W.; Kuang, Y. *Mater. Chem. Phys.* **2004**, *85*, 396-401.

(13) Cheng, B.; Russell, J. M.; Shi, W.; Zhang, L.; Samulski, E. T. *J. Am. Chem. Soc.* **2004**, *126*, 5972-5973.